

SCUOLA DI SCIENZE

Dipartimento di Fisica e Astronomia

Corso di Laurea Magistrale in Astrofisica e Cosmologia

**A search for radio signatures of Dark Matter particles
in the Draco dwarf galaxy**

Tesi di Laurea Magistrale

Candidato:
Patrick Bigi

Relatore:
**Chiar.mo
Prof. Lauro Moscardini**

Correlatori:
**Dott. Gianni Bernardi
Prof. Marco Regis**

This Thesis work was done as part of the research activity of the
Istituto di Radioastronomia - Istituto Nazionale di Astrofisica
(Bologna)

Contents

Abstract	1
Sommario	3
Introduction	5
1 Dark Matter overview	7
1.1 First evidences	7
1.2 Cosmological framework	8
1.2.1 Thermal history of the Universe	10
1.2.2 Structure formation	14
1.3 DM in galaxies	22
1.3.1 Mass function	22
1.3.2 Density profiles	23
1.3.3 Dwarf Spheroidals	25
2 Particle DM detection	27
2.1 Indirect detection with high-energy photons	28
2.1.1 Local Group Dwarfs	30
2.2 Indirect detection with radio signatures	30
2.2.1 From annihilations to synchrotron radiation	30
2.2.2 DM radio searches in the Local Group	36
3 Data analysis and reduction	41
3.1 Interferometry overview	41
3.2 Giant Metrewave observations of the Draco dwarf galaxy	44
3.3 Calibrators	45
3.3.1 Primary calibrator	45
3.3.2 Secondary calibrator	47
3.4 Draco	48
4 Results	57
4.1 Model parameters	57
4.2 Analysis method	58
4.3 Results	59
4.3.1 Results from the Stokes I map	59
4.3.2 Results from the Stokes V map	62
4.4 Comparison with previous works	63
5 Conclusions	65
Bibliography	67

Abstract

Dark Matter is a fundamental component of the Universe both on Galactic and cosmological scales, albeit its intrinsic nature is still largely unknown. Weakly interactive massive particles (WIMPs) have been a long standing Dark Matter particle candidate from the theory stand point, although they have not received observational confirmation so far. Theoretical models suggest that WIMPs can annihilate/decay into electron/positron pairs and, in the presence of magnetic fields, such relativistic electrons would generate an observable synchrotron radio emission that would be the footprint of the WIMP particle and its cross section.

In this thesis we present a search for the radio signature of Dark Matter particles in the Draco dwarf spheroidal galaxy with Giant Metrewave Radio Telescope observations. We analyzed observations from the GMRT, taken with a large bandwidth around 650 MHz and with full array configuration in order to obtain the maximum sensitivity. We used long baselines to identify and remove compact sources, leading to a final image with $20.5''$ angular resolution and a $230 \mu\text{Jy beam}^{-1}$ rms noise. We modeled the DM-induced synchrotron emission in Draco in order to place constraints to the annihilation cross section from our observations.

We found marginal evidence ($\sigma = 1.97$) of a diffuse signal over the whole field of view that is unlikely due to DM but to residual artifacts left in the image after source subtraction. We still present best fits on the annihilation cross section of WIMPs assuming that the signal was due to DM. A best fit cross section of $\sim 10^{-23} \text{ cm}^3 \text{ s}^{-1}$ is obtained at 100 GeV for different annihilation channels. We estimate the best noise rms image that we could achieve with improved calibration/subtraction and we use it to place upper limits near $2 \cdot 10^{-24} \text{ cm}^3 \text{ s}^{-1}$ on the DM cross section for 100 GeV particle mass. We discuss our result in the light of the current literature constraints and explore alternative models for the theoretical emission.

Sommario

La Materia Oscura è una componente fondamentale dell'Universo sia su scala galattica che su quella cosmologica, eppure la sua natura intrinseca è ancora largamente sconosciuta. Dal punto di vista teorico, le *Weakly interactive massive particles* (WIMPs) sono da tempo candidate come particelle di Materia Oscura ma non hanno ancora ottenuto conferme osservative. I modelli teorici suggeriscono che le WIMPs possano annichilire/decadere in coppie elettrone/positrone e che, in presenza di un campo magnetico, questi elettroni relativistici possano generare emissione radio di sincrotrone osservabile, che sarebbe l'impronta delle WIMPs e della loro sezione d'urto.

In questo lavoro di tesi presentiamo una ricerca di segnale radio dovuto all'annichilazione di Materia Oscura nella galassia nana sferoidale Draco, tramite osservazioni effettuate con il Giant Metrewave Radio Telescope (GMRT). Abbiamo analizzato queste osservazioni, prese su una larga banda attorno a 650 MHz e usando l'intero array di antenne per massimizzare la sensibilità. Usando le baseline più lunghe per identificare e rimuovere le sorgenti compatte, abbiamo ottenuto un'immagine finale con risoluzione angolare di $20.5''$ ed un *rms noise* di $230 \mu\text{Jy beam}^{-1}$. Abbiamo modellato l'emissione teorica di sincrotrone dovuta alla Materia Oscura in Draco allo scopo di porre limiti alla sezione d'urto tramite un confronto con le nostre osservazioni.

Setacciando l'intero campo di vista, abbiamo trovato una debole traccia ($\sigma = 1.95$) del segnale diffuso, probabilmente non dovuto alla Materia Oscura ma a residui rimasti nell'immagine dopo la sottrazione delle sorgenti. Ciononostante, presentiamo i *best fit* della sezione d'urto delle WIMPs assumendo che questo segnale sia dovuto a Materia Oscura. Il valore di best fit ottenuto a per una massa di 100 GeV è di $\sim 10^{-23} \text{ cm}^3 \text{ s}^{-1}$ per tutti i canali d'annichilazione considerati. Abbiamo inoltre stimato il miglior rms noise che avremmo potuto ottenere migliorando la calibrazione e la sottrazione delle sorgenti, usandolo poi per porre un limite superiore di $2 \cdot 10^{-24} \text{ cm}^3 \text{ s}^{-1}$ sulla sezione d'urto a 100 GeV. Infine, discutiamo i nostri risultati alla luce dei limiti ottenuti nella letteratura corrente ed esploriamo modelli alternativi per l'emissione teorica.

Introduction

Dark Matter (DM) is one of the pillar of our knowledge of the Universe. For the Standard Cosmological Model, its role is fundamental in the formation and evolution of large scale structures, such that there are evidences that all massive systems, from clusters to dwarf galaxies, are dominated by DM halos. However, its intrinsic nature is still one of the main open issues in the modern physics. A largely supported idea is that DM is made of Weakly Interactive Massive Particles (WIMP), meaning that they have nonzero annihilation cross sections (or decay rates) through which they could generate Standard Model particles. Among the possible secondary products of these interactions are ultrarelativistic electrons and positrons, which are in turn able to emit synchrotron radiation in the presence of a magnetic field. We aimed to detect this radiation in one of the most DM dominated objects known, the Draco dwarf galaxy, with deep radio interferometric observations taken with the Giant Metrewave Radio Telescope (GMRT).

In this thesis work the whole Chapter 1 is dedicated to a DM state of art overview starting with its first historical evidences, then describing its fundamental role in the Standard Cosmological Model. The chapter ends with a description of DM distribution in galaxies with a particular attention on dwarf spheroidals (dSph). In Chapter 2 we describe the main approaches used to detect particle DM, from direct attempts to the γ -ray and radio searches. We summarize the main results in these fields and discuss the theoretical models we use to estimate the diffused synchrotron emission. Chapter 3 is dedicated to the calibration, reduction and analysis work on our observational data, with a brief summarize of the most relevant radio astronomy concepts in the first part. There we present the maps obtained. In Chapter 4, after the description of the maximum likelihood technique used to analyze maps and the benchmark model we assumed for the emission of Draco, we report the results for the comparison with observed maps. Lastly, we draw conclusions in Chapter 5.

Chapter 1

Dark Matter overview

1.1 First evidences

The term Dark Matter (DM) has been used with different meanings along the whole history of science. A recent, detailed review can be found in [Bertone and Hooper \(2018\)](#). For the purpose of this Thesis work, a brief description of the evolution of the modern concept follows.

A fundamental feature of the first evidences of DM is the relation with dynamical anomalies and, in this perspective, we may say that Lord Kelvin, in his Baltimore Lectures (1904¹), was the first to declare that *dark bodies* were needed in order to justify the velocity dispersion of stars in our Galaxy. With this term, he actually meant dark or faint stars, undetectable from the Earth. The French scientist Henri [Poincaré \(1906\)](#) referred to Kelvin's dark bodies as *matière obscure*, in order to manifest his skepticism about its existence.

In 1922, just before his death, the Dutch astronomer Jacobus [Kapteyn \(1922\)](#) made a giant step forward with a quantitative model of Milky Way (MW) dynamics, accurate enough to make the first estimation of local DM density. This approach was developed in later years by his successors and introduced a prolific way, still used nowadays, to inquire about dark matter.

An extragalactic proof was given by [Zwicky \(1933\)](#) in 1933, when he studied galaxies velocities in the Coma cluster as he expected to find a certain velocity dispersion through the relation

$$\sigma^2 \propto \frac{GM}{R}, \quad (1.1)$$

which holds for virialized systems like clusters. He showed that velocity dispersion was much higher than the one resulting from mass estimation, made summing all galaxies masses. He concluded that a *dunkle materie* mass at least ten times bigger than that of galaxies was needed to justify those velocities. This was game changing: from relatively small amounts, DM became the dominant part, in terms of mass, of a relaxed system like the Coma cluster and many consider Zwicky's discovery as the first evidence for the existence of Dark Matter in the way we intend it today. Indeed, astrophysical community was quite skeptical about this hypothesis and only in later years, when several missing mass problems emerged from studies on clusters, groups and single galaxies, scientists began to seriously consider it.

A crucial role in this direction is attributed to Rubin and her studies on rotation curves of spiral galaxies: these systems, such as MW and its neighbour M31, can be treated in first approximation as thin disks rotating around their centers with circular velocities $V_c(R)$. If dynamical equilibrium holds, one can compare gravitational and centrifugal forces to obtain a relation between $V_c(R)$ and radial mass distribution $M(R)$

$$V_c(R) = \sqrt{\frac{GM(R)}{R}} \quad (1.2)$$

¹The Baltimore Lectures on Molecular Dynamics and the Wave Theory of Light. A digital version can be found at <https://archive.org/details/baltimorelecture00kelviala/page/n6/mode/1up>

which, for example, gives a Keplerian fall ($V_c(R) \propto R^{-1/2}$) for a stellar system. With Eq. (1.2) one can build a rotation curve if an estimation of radial mass distribution is made with visible matter.

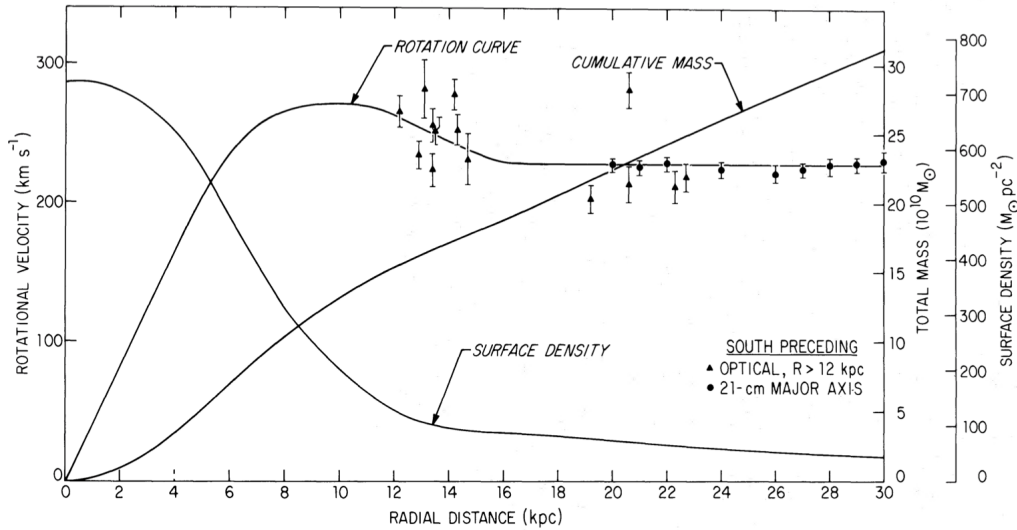


Figure 1.1 Rotation curve, stellar surface density and cumulative mass of M31 as functions of radial distance. Triangles are optical (Rubin and Ford, 1970) data, circles are 21-cm radio observations by Roberts and Whitehurst (1975), which is where the image was taken.

In the 1970s estimations made with stellar surface density distributions, like the one in Figure 1.1, offered radial distribution of circular velocity with Keplerian falls for distances over the visible edge of the disk. On the other hand, Eq. (1.2) can be used to determine $M(R)$ if a survey of circular velocities is made. This is what Rubin and Ford (1970) did observing HII emission regions in M31. Spectral analysis of emission/absorption lines allows to determine radial velocities with reference to the galaxy rest frame and thus reconstruct a $V_c(R)$ profile. What they found is similar to that shown in Figure 1.1, where the rotation curve remains approximately flat. Moreover, HI observations can extend the radial profile way further the optical edge: rotation curves maintain their flatness. This has to be explained with a DM halo whose density profile can be determined in different ways, as we will see in § 1.3.2. In later years Rubin, Ford and many others performed this kind of research on hundreds of galaxies, including the MW, demonstrating that a flat rotation curve is observable in all spirals. The astrophysical community were then convinced to accept the hypothesis of DM.

Since then, our knowledge about the universe can not do without DM. Evidences emerge from every galaxy and every cluster in the universe and, as described in next sections, it is a fundamental paradigm of most of trustworthy cosmological models. The concepts presented in the following overview on the cosmological framework are consolidated and can be found in any cosmology textbook. We are using Coles and Lucchin (1995) as the main reference.

1.2 Cosmological framework

The Standard Cosmological Model stands on two main principles:

- **Cosmological Principle:** the universe is *homogeneous* and *isotropic*, that means there are no privileged positions or directions.
- **General Relativity:** the geometry of the Universe is related to the energy-mass presence and distribution, as the Theory of General Relativity (GR) describes.

The Cosmological Principle, which is supported by different observational evidences like the Cosmic Microwave Background (CMB), is meant to apply on large scales, which means on the order of hundreds of Mpc in our epoch but needs to be scaled for the expansion of the Universe as we go back in time. The second principle may stand on its own feet as GR has been a long series of proofs and successes we do not need to summarize. GR allows to use Einstein's field equation

$$R_{\mu\nu} - \frac{1}{2}Rg_{\mu\nu} = \frac{8\pi G}{c^4}T_{\mu\nu}, \quad (1.3)$$

where $R_{\mu\nu}$ is Ricci curvature tensor, R is the scalar curvature and $g_{\mu\nu}$ is the metric tensor. This field equation, assuming a perfect fluid behavior for the energy-impulse tensor $T_{\mu\nu}$, leads us to the Friedmann equations

$$\dot{a}^2 + kc^2 = \frac{8\pi}{3}G\rho a^2, \quad (1.4)$$

$$\ddot{a} = -\frac{4\pi}{3}G\left(\rho + \frac{3p}{c^2}\right)a \quad (1.5)$$

which describe the dynamic evolution of the Universe through the scale factor $a(t)$ and its temporal derivatives. ρ and p are respectively the mass density and the pressure and k describes the geometry. Friedmann equations are always associated with an adiabatic equation, written as

$$d(\rho c^2 a^3) = -p da^3. \quad (1.6)$$

Manipulation of Eq. 1.4, 1.5 and 1.6 lets us introduce some useful parameters like Hubble parameter $H \equiv \dot{a}/a$, whose inverse, the Hubble time τ_H , sets a reference for every other timescale, as we will see later. We also define the critical density

$$\rho_{\text{cr}} \equiv \frac{3H^2}{8\pi G}, \quad (1.7)$$

so that, with some other manipulations, we can write the revealing (calculated at present time) equation

$$H_0^2 \left(1 - \frac{\rho_0}{\rho_{\text{cr},0}}\right) = -\frac{kc^2}{a_0^2}. \quad (1.8)$$

This shows how, in order to have a flat Universe, the curvature parameter k and so the quantity inside the brackets needs to be exactly zero. The density parameter is generally defined as

$$\Omega \equiv \frac{\rho}{\rho_{\text{cr}}}, \quad (1.9)$$

so that the flatness condition, calculated today, becomes $\Omega_0 = 1$. Every form of energy, including matter, has to be accounted for the density parameter (see [Aghanim et al., 2020](#) for precise, recently obtained values):

- **Radiation:** $\Omega_{0,\text{rad}} \simeq 8.24 \cdot 10^{-5}$ photons today represent an almost negligible fraction but they were dominating in the primordial Universe, in the so called *Radiation Era*.
- **Matter:** $\Omega_{0,\text{M}} \simeq 0.27$ this fraction includes both baryonic and Dark matter, with the last one dominating over the first with a contribution of $\Omega_{0,\text{DM}} \simeq 0.23$, meaning that baryons represent just 17% of the matter in the Universe. This constituent was dominating in the past during the *Matter Era* but now another component is in command.
- **Dark Energy:** $\Omega_{0,\Lambda} \simeq 0.73$ dominates the Universe today. This concept was firstly introduced by Einstein with his cosmological parameter Λ . It was included as $-\Lambda g_{\mu\nu}$ in the LHS of Eq. (1.3) in order to allow static Universe solutions for Eq. (1.4) and (1.5). Einstein believed that this term was to intend as a modified gravity effect while today it is attributed to the contribute of Dark Energy.

These three terms have dominated the universe successive eras we are describing in details later. First, we need to write the state equation

$$p = w\rho c^2, \quad (1.10)$$

where w is the state equation parameter that assumes a different value depending on which component we consider:

- $w=0$ for matter, as matter density results negligible.
- $w=1/3$ for radiation and relativistic matter.
- $w=-1$ for Λ , which behave as a negative pressure.

Now, if we apply Eq. (1.10) on Eq. (1.6) and integrate, we get trends for density as a function of the scale factor a , or redshift z , for three constituents

$$\rho \propto \begin{cases} a^{-3} \propto (1+z)^3 & \text{(matter)} \\ a^{-4} \propto (1+z)^4 & \text{(radiation)} \\ a^0 \propto (1+z)^0 & \text{(\Lambda)}. \end{cases} \quad (1.11)$$

From this, it is clear that radiation dominated the Universe in its early stages ($z \rightarrow +\infty$). With density parameters calculated today, we can infer two important redshifts:

$$z_{\text{eq,r-m}} = \frac{\Omega_{0,\text{m}}}{\Omega_{0,\text{r}}} \simeq 5000, \quad (1.12)$$

$$z_{\text{eq,m-}\Lambda} = \left(\frac{\Omega_{0,\Lambda}}{\Omega_{0,\text{m}}} \right)^{1/3} \simeq 0.3. \quad (1.13)$$

These equivalence redshifts define the limits of the three eras already mentioned. Their importance will be manifest in the next section, where we describe most important steps in the thermal evolution of the Universe.

1.2.1 Thermal history of the Universe

In this section we are going to describe the most relevant steps in the thermal evolution of the Universe with a focus on the DM role and implications. The journey starts, according to the Standard Model, at $t_{\text{P}} \sim 10^{-47}$ s, the so called Planck time. We do not have a physical model that can explain what happened before but we do not need to know for the purposes of this Thesis.

For similar reasons, we are not interested in describing in details motivations and modalities of *Phase transitions* and *Inflation*. The first is a complete matter of particle physics as in the primordial overcrowded plasma, phase transitions naturally develop, breaking symmetries and leading to a more ordered system. Inflation is generically intended as an accelerated expansion phase of the Universe. There are numerous different models but a shared idea is the presence of an energetic scalar field, which vacuum energy density dominating among Ω contributors. The field underwent a phase transition which boosted expansion into an exponential phase. This summarily describes the concept of inflation, whose best quality is that of solving some of the Standard Model problems like the flatness and the horizon ones. However, a detailed quantitative model is hard to set since no observations of that era are available.

Early hot Universe In these early stages, the Universe is hot and dense, such that matter and radiation are indistinguishable and they share the same temperature, which can be used as a effective clock to refer to events and eras. More precisely, a trend of the temperature can be found including energy densities and pressures of both matter and radiation into the adiabatic Eq. (1.6), obtaining

$$\frac{dT}{T} = -\frac{da}{a} \frac{1 + \sigma_r}{\frac{1}{2} + \sigma_r}, \quad (1.14)$$

where σ_r is the radiation entropy per baryon. This adimensional quantity, defined as

$$\sigma_r \equiv \frac{4m_p \sigma T^3}{3k_B \rho_m},$$

becomes constant after decoupling and has a value of $\sigma_{r,0} = 1.35 \cdot 10^8 (\sigma_{b,0} h^2)^{-1}$, large enough to simplify Eq. (1.14) getting

$$T \propto a^{-1} \propto (1+z). \quad (1.15)$$

Radiation and matter share this temperature until particle-photon collisional timescale $\tau_{\text{coll}} = (nc\sigma)^{-1}$ is smaller than expansion timescale $\tau_{\text{exp}} \sim 1/H_0$. When $\tau_{\text{coll}} \gg \tau_{\text{exp}}$, we have two different behaviors

$$T \propto \begin{cases} a^{-1} \propto (1+z) & \text{(radiation)} \\ a^{-2} \propto (1+z)^2 & \text{(matter)} \end{cases} \quad (1.16)$$

and these two components evolve independently. The moment $\tau_{\text{coll}} = \tau_{\text{exp}}$ is called t_{dec} . While the expansion timescale only depends on the cosmology assumed, the collisional timescale varies from particle to particle and anyway, t_{dec} (or z_{dec}) is to be intended as a time interval in which matter gradually decouples from radiation.

Now we can summarize the most relevant events in the thermal evolution of the Universe referring to temperatures instead of, or together with, redshifts. This tool becomes even more efficient since we need to account annihilations: a particle of mass m_p in equilibrium with radiation can survive if the thermal energy $k_B T$ is larger than $2m_p c^2$, otherwise annihilations would dominate. This means that, in an expanding Universe where T decreases monotonically, every particle species has its own T_{ann} below which it generates two photons.

Hadronic and Leptonic eras When the last phase transition, namely the quark-hadron one, ends at $T_{\text{QA}} \simeq 200 \text{ MeV } k_B^{-1}$, quarks are confined in hadrons, generating for the first time protons, neutrons, pions etc. This Hadronic Era lasts a very few since the lightest of the family, the pion, annihilates at $T_{\text{ann},\pi} = 130 \text{ MeV } k_B^{-1}$. Then the Leptonic Era begins, where electrons, positrons, muons, tauons, neutrinos and photons dominate. As temperature slowly decreases, even these light particles reach their T_{eq} and annihilate. This is a reversible process that conserves entropy, which is mostly from radiation

$$S = \frac{P + \rho c^2}{T} V = \frac{2}{3} g^* \sigma T^3 V, \quad (1.17)$$

where

$$g^* = \sum_i g_{i,B} + \frac{7}{8} \sum_i g_{i,F} \quad (1.18)$$

is the effective statistical weight, whose value depends on which particle species are coupled to radiation, so that when a species decouples, or annihilates, g^* drops. On the other hand, if $S_{(-)}$ is the entropy before an annihilation, the entropy after $S_{(+)}$ has to be the same such that, from Eq. (1.17),

$$g_{(-)}^* T_{(-)}^3 = g_{(+)}^* T_{(+)}^3. \quad (1.19)$$

Whenever an annihilation occurs, the plasma temperature has a small jump to reflect the effective statistical weight drop. Even though this does not affect the global temperature trend, it produces an important feature regarding neutrinos: their decoupling occurs at $T_{\text{dec},\nu} = 3 \cdot 10^{10}$ K, just before the electron-positron annihilation, the last of Leptonic Era. Even though decoupled neutrinos remain relativistic until very recent times, therefore having the same adiabatic trend, they do not follow the temperature jump of radiation. Since $g_{(-)}^* = 11/2$ (photons and e^\pm) and $g_{(+)}^* = 2$ (photons only), the neutrino temperature will be, from Eq. (1.19),

$$T_\nu = \left(\frac{11}{4}\right)^{1/3} T_r. \quad (1.20)$$

We know from CMB that radiation temperature is today $T_{0,r} \simeq 2.7$ K, that makes $T_{0,\nu} \simeq 1.9$ K. This value allows to make some considerations on neutrinos: if they are massless, the relation $\rho_\nu c^2 = \sigma T^4$ is valid and the contribution of $\Omega_{0,\nu} \simeq 0.7\Omega_{0,r}$ would be added to the radiative component, which would not change that much. On the other hand, if they have a mass, their density would be $\propto T_{0,\nu}^3$, which gives, assuming 3 neutrino flavors,

$$\Omega_{0,\nu} = 0.3 \frac{\langle m_\nu \rangle}{10\text{eV}} h^{-2}. \quad (1.21)$$

This puts a sort of limit of $\sim 10\text{eV}$ on the neutrino mass, otherwise they would overcome the total matter density. With a smaller mass, neutrino would instead be a candidate DM particle, also due to its low interactions rate. However it would be a Hot Dark Matter candidate, which, as we will see in section 1.2.2, disagrees with the Standard Cosmological Model.

Primordial Nucleosynthesis We have to make a step back at the end of Hadronic Era in order to talk about the fundamental Primordial Nucleosynthesis. This process is one of the greatest success of the Standard Model because it fully fits the primordial abundance of elements like Deuterium and Helium, unexplained by the only stellar evolution. Deuterium is the first to form and the more difficult one since in the reaction $n + p \rightleftharpoons D + \gamma$, photodissociations dominate at high temperatures. Quantitatively, we can use the Boltzmann equation to derive the operative equation

$$X_D = X_n X_p \exp\left(-29.33 + \frac{25.82}{T_9} - \frac{3}{2} \ln T_9 - \ln(\Omega_b h^2)\right), \quad (1.22)$$

where $X_i \equiv n_i/n_{\text{tot}}$ and $T_9 \equiv T/10^9$ K. It is clear that X_D is negligible until the temperature gets below $T_9 \simeq 1$. At $T^* \simeq 0.9 \cdot 10^9$ ($t^* \sim 200$ s), the Deuterium abundance becomes significant and then drops again when the Helium production starts through



The relative abundance of Helium produced can be found as

$$Y_{\text{He}} \simeq Y_{\text{He}}(t^*) \simeq 2X_n(t^n) \exp\left(-\frac{t^* - t_n}{\tau_n}\right), \quad (1.23)$$

where $t_n \sim 20$ s is the time neutrons and protons are no more in equilibrium, but the long mean lifetime of neutrons ($\tau_n \sim 900$ s) allows nucleosynthesis to produce $Y_{\text{He}} \simeq 0.25$. These predicted abundances, relative to Hydrogen, are plotted in Figure 1.2 as a function of baryon density (ρ_b). It is evident that ${}^4\text{He}$ abundance is almost independent of ρ_b , while Deuterium is highly sensible to baryon's density parameter variations. From the observational point of view, Helium primordial abundance is far more easy to estimate than Deuterium's. The consistency interval in Figure 1.2 was obtained by Schramm and Turner (1996) using a combination of ${}^4\text{He}$, D, ${}^3\text{He}$ and ${}^7\text{Li}$ observations. The Deuterium abundance strong dependence on ρ_b permitted

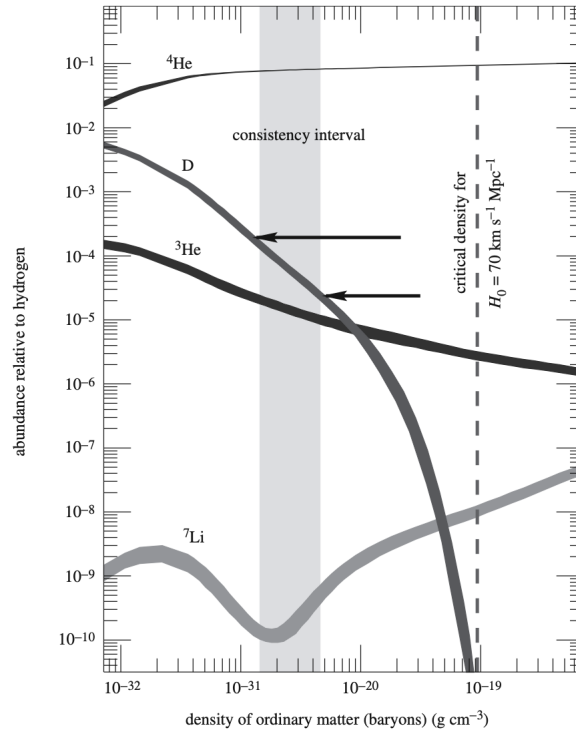


Figure 1.2 Relative abundances of ${}^4\text{He}$, ${}^3\text{He}$, D and ${}^7\text{Li}$ as function of baryon density. The image is taken from [Coles and Lucchin, 1995](#).

to put boundaries on the Ω_b parameter already in the 70s, establishing another proof of the existence of DM, necessary in order to reach $\Omega_m \sim 0.3$.

At the end of the Leptonic Era, we have a Universe made mostly of photons and free electrons and protons, with some negligible, in terms of number density, light nuclei like Helium. This is the so-called **Plasma Era**, where e^- and p^+ are coupled and have the same temperature, Compton scattering guarantees equilibrium with photons so that radiation is distributed as a black body. As the temperature keeps decreasing, electrons start to bound with nuclei for the very first time. We usually set the time of (re)combination at the moment when the ionization fraction $x \equiv n_e/n_{\text{tot}} = 0.5$. This time (or temperature) naturally depends on the considered species and its ionization level. The estimation of this temperature can be made with Saha's equation, for example for neutral hydrogen:

$$\frac{x^2}{1-x^2} = \frac{1}{n_{\text{tot}}} \left(\frac{m_e k_B T}{2\pi\hbar} \right)^{3/2} e^{-\frac{B_H}{k_B T}}, \quad (1.24)$$

where $B_H = 13.6$ eV is neutral hydrogen binding energy and it gives $T_{\text{rec,H}} \simeq 4000$ K corresponding to $z_{\text{rec,H}} \simeq 1500$. This can be compared with decoupling time t_{dec} which, we previously said, occurs when $\tau_{\text{coll}} = \tau_{\text{exp}}$. Even if this happens before t_{rec} , residual interactions between protons and photons via Compton scattering guarantee the same temperature for matter and radiation up to $z_{\text{dec}} \sim 300$, in non thermal equilibrium conditions. As the Universe becomes more and more neutral, radiation is free to propagate for the first time generating what we call Cosmic Microwave Background (CMB). Once again, the emission of this radiation did not happen altogether: a Gaussian distribution describes the probability of a photon to be scattered for the last time at a certain t (or z). This distribution's mean value is called redshift of the last scattering and its value $z_s \simeq 1100$, which we assume as the redshift from which CMB comes from, sets the most remote time we can observe in the Universe. CMB data allowed to put many boundaries on the Standard Cosmological Model parameters and, as we will see later, seem to agree with the Cold Dark Matter scenario we are going to describe soon.

1.2.2 Structure formation

In this section we are going to describe how structures of the Universe have formed from the primordial perturbations. The dissertation moves from the perturbation theory applied on the universe at the end of inflation, which may be the cause of primordial fluctuations from the homogeneous mean.

The theory is known as gravitational Jeans instability and was originally applied on a generic homogeneous mean which has some density ($\delta\rho$) or velocity (δv) fluctuations. Under certain conditions these fluctuations can grow and start a gravitational collapse. In order to give a physical significance, let start with a order-of-magnitude example: we have a spherical region of size λ with an overdensity $\delta\rho > 0$ with respect to the homogeneous mean density ρ . This overdensity will grow if the gravitational force per unit mass

$$F_G \simeq \frac{GM}{\lambda^2} \simeq G\rho\lambda,$$

is bigger than the pressure force per unit mass F_p

$$F_p \simeq \frac{p\lambda^2}{M} \simeq \frac{v_s^2}{\lambda}, \quad (1.25)$$

where $v_s \simeq \sqrt{p/\rho}$ is the sound velocity. The condition is therefore

$$\lambda > \lambda_J \sim \frac{1}{\sqrt{G\rho}} \quad (1.26)$$

and λ_J is called the Jeans length. Almost the same result can be obtained by comparing potential and kinetic energy of the region as well as free-fall and sound-crossing times. In any case, if the scale of the overdensity is bigger than its Jeans scale, $\delta\rho$ will grow, otherwise the perturbation cannot grow.

We now describe how to get analytical solutions for the evolution of perturbations in a linear regime ($\delta\rho/\rho < 1$). We start in the simple case of a collisional fluid, then we will describe analogue results for different cosmological cases and components. Conservation of mass, momentum and the Poisson equation, together with an equation of state are the four equations of the system we need to solve. Let assume that background values ρ_0 , p_0 , ϕ_0 and $v_0(=0)$ are a solution for the system and an adiabatic state equation ($p(\rho, S) = p(\rho)$). Once we introduce perturbations $\delta\rho$, δp , $\delta\phi$, δv and linearize equations, we get

$$\begin{cases} \delta\rho_t + \rho_0 \nabla \cdot \delta\vec{v} = 0 \\ \rho_0 (\delta\vec{v}_t + c_s^2 \nabla \delta - \nabla \delta\phi) = 0 \\ \nabla^2 \delta\phi = -4\pi G \delta\rho, \end{cases} \quad (1.27)$$

where t pedices indicate temporal derivatives and $\delta \equiv \delta\rho/\rho_0$. Assuming solutions in the form of plane waves $S(\vec{r}, t) = S_{\mathbf{k}} e^{i(\vec{k}\cdot\vec{r} - \omega t)}$, so that time and position dependencies are separated, we obtain the dispersion system

$$\begin{cases} -\omega \delta_{\mathbf{k}} + k \delta\vec{v}_{\mathbf{k}} = 0 \\ -\omega \delta\vec{v}_{\mathbf{k}} + k(c_s^2 \delta_{\mathbf{k}} - \delta\phi_{\mathbf{k}}) = 0 \\ -k^2 \delta\phi_{\mathbf{k}} = -4\pi G \delta\rho_{\mathbf{k}}. \end{cases} \quad (1.28)$$

By setting its determinant to zero, we have the dispersion relation

$$\omega^2 = c_s^2 k^2 - 4\pi G \rho_0. \quad (1.29)$$

From this, we can derive three cases:

- $\omega^2 = 0$ leads to the definition of Jeans wave number and, thus, Jeans length as

$$k_J = \frac{\sqrt{4\pi G\rho_0}}{c_s} \leftrightarrow \lambda_J = \frac{2\pi}{k_J} = \frac{c_s}{\sqrt{2G\rho_0}}. \quad (1.30)$$

In this ideal case, the perturbation is freezed and does not evolve.

- $\omega^2 > 0$, which means $k < k_J$, produces two waves moving with opposite directions but constant amplitudes, thus perturbations do not grow.
- $\omega^2 < 0$, which means $k > k_J$, produces two stationary wave solutions of either increasing or decreasing (exponentially) amplitude. The increasing solution is what we are interested in as it leads to gravitational collapse.

An equivalent parameter used to deal with gravitational instability is the Jeans mass, which is the mass of a sphere with radius $\lambda_J/2$:

$$M_J \equiv \frac{\pi}{6} \rho \lambda_J^3. \quad (1.31)$$

This proceeding is similar for more complicated cases we are going to describe later thus, for the sake of brevity, we will just report the dispersion relations next times.

The application of this theory in a cosmological context asks to define an important quantity, the cosmological horizon radius

$$R_H(t) = a(t) \int_0^t \frac{cdt'}{a(t')}. \quad (1.32)$$

It represents the largest distance from which a signal could have reached an observer at time t , establishing a causal connection between them. Outside this radius, only gravity is relevant so that one has to distinguish between fluctuations larger or smaller than $R_H(t)$. Perturbations in the cosmological context are treated as closed Universes (whose Hubble parameter is indicated with H_p) inside a flat Universe which has the role of background solution (with its H_b); if one imposes $H_p = H_b$, the behavior outside $R_H(t)$ results as

$$\delta \propto (\rho_b a^2)^{-1} \propto a^{1+3w} \propto \begin{cases} a^2 & t < t_{eq} \\ a & t > t_{eq}. \end{cases} \quad (1.33)$$

This means that perturbations outside the horizon always grow following the trend of the dominant component, which obviously changes at t_{eq} . As the horizon grows in time, more and more perturbations enter its radius and begin to act differently. Again, we need to distinguish between before and after the equivalence. Before it, in a radiation dominated Universe, the radiation pressure has to be accounted and the same process used to find Eq.(1.29) leads to

$$\ddot{\delta}_k + 2\frac{\dot{a}}{a}\dot{\delta}_k + \delta_k \left(k^2 c_s^2 - \frac{32}{3}\pi G\rho_0 \right) = 0, \quad (1.34)$$

which is the solution for the relativistic component. In this case the Jeans wave number is $k_J = \sqrt{32\pi G\rho_0/3c_s^2}$ and, because $c_s = c/\sqrt{3}$, the Jeans scale can be compared with the horizon radius:

$$\lambda_J = \frac{2\pi ct}{\sqrt{3}} > R_H = 2ct,$$

meaning that the Jeans scale loses its significance since it is a non causally connected scale. Perturbations then cannot grow in the radiation era.

After the equivalence, the dispersion relation becomes

$$\ddot{\delta}_k + 2\frac{\dot{a}}{a}\dot{\delta}_k + \delta_k (k^2 c_s^2 - 4\pi G\rho_0) = 0, \quad (1.35)$$

valid for the matter component. In this case, the Jeans wave number is $k_J = \sqrt{25\pi G\rho_0/6c_s^2}$. Solutions may be found in the form $\delta_k \propto t^\alpha$, where

$$\alpha_{1,2} = -\frac{1 \pm 5\sqrt{1 - (\lambda_J/\lambda)^2}}{6}. \quad (1.36)$$

For scales much greater than Jeans scale, the only one positive solution gives $\delta_k \propto t^{2/3} \propto a$ in an EdS, matter dominated universe.

The procedure for DM is quite different. Indeed, we know that baryons decouple after equivalence ($t_{\text{eq}} < t_{\text{dec}}$), but we cannot say the same thing for DM since we do not know what it is made of. Thus we need to consider a dispersion relation for DM before equivalence: we shall include every component in the gravitational term but we already saw that radiation and baryons do not develop fluctuations so we can ignore them and, assuming that c_s is velocity dispersion for DM, obtain

$$\ddot{\delta}_{k,\text{DM}} + 2\frac{\dot{a}}{a}\dot{\delta}_{k,\text{DM}} + \delta_{k,\text{DM}}(k^2c_s^2 - 4\pi G\rho_{0,\text{DM}}) = 0. \quad (1.37)$$

Is useful to make variable change with $x \equiv a/a_{\text{eq}}$. This introduces dependencies on \dot{a} and \ddot{a} which are removed using Friedmann's equations (1.4) and (1.5). Some further algebra leads to the hypergeometric equation

$$\delta_{k,\text{DM}}'' + \frac{3x+2}{2x(1+x)}\delta_{k,\text{DM}}' - \frac{3}{2x(1+x)}\delta_{k,\text{DM}} = 0, \quad (1.38)$$

where apices indicate a derivative with respect to x . The only growing solution is $\delta_{k,\text{DM}}^+ = 1 + 3x/2$, valid before equivalence. An important feature arises as a DM perturbation which enters the horizon at $\sim t_H$ grows by a factor

$$\frac{\delta(t_{\text{eq}})^+}{\delta(t_H)^+} = \frac{1 + 3/2}{1 + 3a_H/2a_{\text{eq}}} < 5/2, \quad (1.39)$$

thus every perturbation that enters the horizon before t_{eq} grows by a factor less than 5/2, while they grow as a^2 outside the horizon. This is called Meszaros effect or stagnation effect and it introduces a scale dependence on the growth of DM halos because smaller scales stagnate more than bigger ones.

An additional feature arises at the moment of decoupling of baryons. In fact, ordinary matter were not able to grow overdensities since its perturbations were dissolved by radiation pressure, but after t_{dec} baryons are subject to collapse. In the meanwhile, DM grew its perturbations as we just saw so that baryons find themselves in a perturbed gravitational field. The dispersion relation can now be written as

$$\ddot{\delta}_{k,b} + 2\frac{\dot{a}}{a}\dot{\delta}_{k,b} + \delta_{k,b}(k^2c_s^2 - 4\pi G\rho_{0,\text{DM}}) = 0 \quad (1.40)$$

and we can use Friedmann's equations as done previously to get

$$\frac{2}{3}a\delta_{k,b}'' + \delta_{k,b} - A = 0. \quad (1.41)$$

This has a growing solution which, assuming $\delta_{k,b}(t_{\text{dec}}) = 0$, results as

$$\delta_{k,b} = \delta_{k,\text{DM}}\left(1 - \frac{a_{\text{dec}}}{a}\right). \quad (1.42)$$

Its trend is shown in Figure 1.3 where baryonic perturbations grow asymptotically following DM ones. This is called *baryon catch-up*. If there was no DM in the universe, baryonic perturbations would be much lower than we observe them. In fact, the solution found in Eq. (1.33) can reproduce current overdensities if $\delta_b(t_{\text{dec}}) \sim 10^{-3}$ but CMB observations tell us that perturbations were much lower at decoupling. If DM is included, δ_b can easily reach current values thanks to baryon catch-up, starting from the $\delta_b(t_{\text{dec}}) \sim 10^{-5}$ given by CMB.

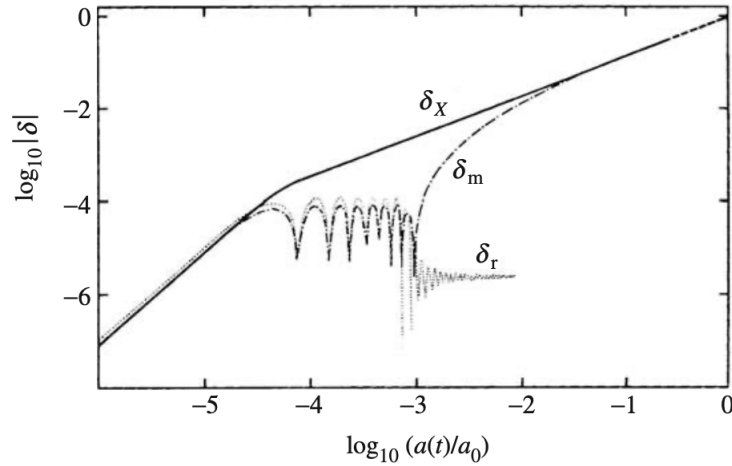


Figure 1.3 Evolution of a perturbation that enters the horizon at a_{eq} , so that no stagnation effects are accounted. δ_X is the relic perturbation which grows as $\propto a$ after equivalence. δ_m and δ_r oscillate until decoupling, then baryons reach δ_X asymptotically and radiation keeps oscillating on its own. Taken from [Coles and Lucchin, 1995](#).

Thermal relics We use to refer to unspecified particles generated in the hot early Universe as *cosmic relics* and in particular on *thermal* ones, meaning that they are in thermal equilibrium with other components until they decouple. We will refer to these particles with a suffix X , for example with their mass m_X or the time when they decouple, $t_{d,X}$. A further distinction is between *hot* and *cold* thermal relics with the first still being relativistic at $t_{d,X}$ and the second which became non relativistic at $t_{n,X} < t_{d,X}$. This distinction reflects on the two main types of DM cosmologists are used to consider: *Hot* (HDM) and *Cold Dark Matter* (CDM). Because the term relic has a much broader significance, we will use it for the following dissertation. We can use Boltzmann equation

$$\frac{dn_X}{dt} + 3\frac{\dot{a}}{a}n_X + \langle\sigma_A v\rangle n_X^2 - \Psi = 0, \quad (1.43)$$

to describe the density time evolution, where σ_A is the annihilation cross-section and Ψ is the particle pairs creation rate, which can be written as $\Psi = \langle\sigma_A v\rangle n_{\text{eq},X}^2$ if creations and annihilations are in equilibrium. Using a comoving density n_c and using a instead of time, Eq. (1.43) can be written as

$$\frac{a}{n_{c,\text{eq}}} \frac{dn_c}{da} = -\frac{\tau_H}{\tau_{\text{coll}}} \left[\left(\frac{n_c}{n_{c,\text{eq}}} \right)^2 - 1 \right]. \quad (1.44)$$

This suggests two approximate solutions: until $\tau_{\text{coll}} \ll \tau_H$, e.g. way before $t_{d,X}$, density is the equilibrium one $n_{c,\text{eq}}$; the moment of decoupling sets the so-called *freeze out*, and the comoving density does not change since then. This feature can be used, in the hot relics scenario, to put an upper bound on neutrinos mass or, assuming the mass, to have an estimation for the time neutrinos became non relativistic. Anyway, as will be clear soon, we have more interest in the cold relics scenario: at the moment of their decoupling, X particles have a number density ruled by the Boltzmann distribution

$$n(t_{d,X}) = \frac{g_X}{h^3} \left(\frac{m_X k_B T_{d,X}}{2\pi} \right)^{3/2} \exp\left(-\frac{m_X c^2}{k_B T_{d,X}}\right), \quad (1.45)$$

such that we can get their present number density as

$$n_{0,X} = n_{d,X} \left(\frac{a(t_{d,X})}{a_0} \right)^3 = n_{d,X} \frac{g_0^*}{g_X^*} \left(\frac{T_{0,r}}{T_{d,X}} \right)^3, \quad (1.46)$$

where $T_{d,X}$ is the real question mark. To determine it, one can use the condition

$$\tau_H(t_{d,X}) = \tau_{\text{coll}}(t_{d,X}) \quad (1.47)$$

and make some assumptions. An old but still valid result was found by [Lee and Weinberg \(1977\)](#), when they assumed a Dirac particle as DM candidate and an electroweak annihilation cross-section of $\langle \sigma_a v \rangle \sim 3 \cdot 10^{-26} \text{ cm}^3 \text{ s}^{-1}$. This puts the DM candidate in the so-called *Weakly Interactive Massive Particles* or *WIMPs* category, which is the preferred for Standard Cosmological Model and will be ours too. This value is known as the "thermal" cross-section. Combining relations Eq. (1.47) and (1.46) they were able to put a lower limit of 2 GeV on m_X .

Scale masses As seen previously, the Jeans mass defined in Eq. (1.31) is useful to determine if a perturbation is going to collapse or not. A version for collisionless component can be written as

$$M_{J,X} = \frac{\pi}{6} m_X n_X \lambda_{J,X}^3, \quad (1.48)$$

where $\lambda_{J,X}$ is the Jeans scale with mean particle velocity v_X instead of sound velocity. We need to distinguish four time intervals where v_X changes its trend and so does $M_{J,X}$. One can easily find

$$M_{J,X} \propto \begin{cases} a^3 & \text{for } z_{n,X} < z \\ a^{3/2} & \text{for } z_{d,X} < z < z_{n,X} \\ a^0 \simeq \text{const.} & \text{for } z_{\text{eq}} < z < z_{d,X} \\ a^{-3/2} & \text{for } z < z_{\text{eq}} \end{cases} \quad (1.49)$$

and see how Jeans mass is constantly at its maximum value during the interval between decoupling and equivalence. This is valid for both hot and cold relics except for the interval between $z_{n,X}$ and $z_{d,X}$ because hot relics become non relativistic later and they keep growing as a^3 until decoupling. The maximum value depends on m_X and for a typical cold relic candidate mass, is in the order of $\sim 10^6 M_\odot$. Such a small mass can be easily overtaken by perturbations and so they can grow while, in the hot relics scenario, $M_{J,X} \simeq 10^{15} M_\odot$ is nearly the size of a big galaxy cluster. Another important parameter is the *free-streaming scale*

$$\lambda_{\text{fs},X} = a(t) \int_0^t \frac{v_X}{a(t')} dt'. \quad (1.50)$$

We talk in terms of free-streaming when collisionless particles are involved. They do not have a sound speed, but move at a certain mean square velocity v_X and, if it is large enough, they can escape their self-gravity. In other terms, perturbations in collisionless fluids under the Jeans scale not only do not grow, but can be cancelled if they are under free-streaming scale too. As for Jeans mass, we can use free-streaming mass

$$M_{\text{fs},X} = \frac{\pi}{6} m_X n_X \lambda_{\text{fs},X}^3 \quad (1.51)$$

and look for its trends, which result

$$M_{\text{fs},X} \propto \begin{cases} a^3 & \text{for } z_{n,X} < z \\ a^{3/2} & \text{for } z_{d,X} < z < z_{n,X} \\ \ln^3 a & \text{for } z_{\text{eq}} < z < z_{d,X} \\ a^0 \simeq \text{const.} & \text{for } z < z_{\text{eq}}. \end{cases} \quad (1.52)$$

This time, the free-streaming mass slowly increases until equivalence and then becomes constant at its maximum value, in fact free-streaming mass cannot decrease by definition. Soon after equivalence, we have that $M_{J,X} \simeq M_{\text{fs},X}$ in both cold and hot relics cases. In the

hot scenario, this means that after equivalence every perturbation below $10^{15}M_{\odot}$ is cancelled by free-streaming and thus smaller structures like galaxies and groups have formed by later fragmentation of big halos. It is called *top-down* or *antihierarchical scenario* and naturally it assumes HDM. The cold relic hypothesis, that is assuming CDM, leads in the opposite direction, the so-called *bottom-up* or *hierarchical scenario*, where small halos merge to form bigger structures.

Power spectrum In order to describe the matter distribution in the universe and its evolution, cosmologists prefer to use the Fourier transform space and wavenumber \mathbf{k} , which we introduced in § 1.2.2. The perturbation field we indicated with $\delta(\mathbf{x})$ can be seen as Fourier transform

$$\delta(\mathbf{x}) = \frac{1}{(2\pi)^3} \int \delta(\mathbf{k}) e^{i\mathbf{k}\cdot\mathbf{x}} d^3\mathbf{k} \quad \Leftrightarrow \quad \delta(\mathbf{k}) = \int_V \delta(\mathbf{x}) e^{-i\mathbf{k}\cdot\mathbf{x}} d\mathbf{x}. \quad (1.53)$$

This allows to write the two-point correlation function, defined as

$$\xi(r) \equiv \langle \delta(\mathbf{x}) \delta(\mathbf{x} + \mathbf{r}) \rangle, \quad (1.54)$$

in the form

$$\xi(r) = \frac{1}{(2\pi)^6} \int d^3\vec{k} \int d^3\mathbf{k}' \langle \sigma(\mathbf{k}) \sigma(\mathbf{k}') \rangle e^{i\mathbf{k}\cdot(\mathbf{x}+\mathbf{r})} e^{i\mathbf{k}'\cdot\mathbf{x}}. \quad (1.55)$$

This function correlates the perturbation field with itself, giving the probability of two objects of being at distance r . The corresponding function in the Fourier space is defined by the relation

$$\langle \sigma(\mathbf{k}) \sigma(\mathbf{k}') \rangle = (2\pi)^3 \mathcal{P}(k) \delta_{\text{D}}(\mathbf{k} + \mathbf{k}'), \quad (1.56)$$

where δ_{D} is the three-dimensional Dirac delta distribution. $\mathcal{P}(k)$ is called the *power spectrum*. If $\delta(\mathbf{x})$ is Gaussian, its variance $\sigma^2 = \langle \delta^2(\mathbf{x}) \rangle$ can be written, thanks to the Parseval Theorem, as

$$\sigma^2 = \frac{1}{(2\pi)^3} \int P(\mathbf{k}) d^3\mathbf{k}. \quad (1.57)$$

In practice the quantity used is the *mass contrast*, defined as $\delta_M(\mathbf{x}) = \delta M / \bar{M}$, which leads to the *mass variance*

$$\sigma_M^2 = \frac{1}{(2\pi)^3} \int P(\mathbf{k}) W^2(\mathbf{k}, R) d^3\mathbf{k}, \quad (1.58)$$

where $W(\mathbf{k}, R)$ is a filter function needed to the comparison with observations. The power spectrum physically represents the importance of a given scale k in the global distribution of perturbations. For example, assuming a power law $P(k) = Ak^n$, bigger scales will have more power, that is the perturbations on large scales will have larger amplitude, if $n < 0$. Applying the linear theory, one can get scale relations for the mass variance, which evolve with the square of growing solutions δ_+ :

$$\sigma_M^2 \propto \delta_+^2 k^{n+3} \propto \delta_+^2 R^{-(n+3)} \propto \delta_+^2 M^{-(n+3)/3}. \quad (1.59)$$

Moreover, from a statistical point of view, the density contrast introduced above allows to develop a proper formalism in which δ has to be invariant for translations and rotations, according to the cosmological principles of homogeneity and isotropy. Perturbations of the primordial universe are just induced at the end of inflation as random fluctuations, such that we can assume a nearly Gaussian distribution

$$\mathcal{P}(\delta) d\delta = \frac{1}{(2\pi\sigma^2)^{1/2}} \exp\left(-\frac{\delta^2}{2\sigma^2}\right) d\delta, \quad (1.60)$$

which has to be accompanied by a warning: for how it is defined, the density contrast has to be > -1 , otherwise it would indicate a negative density. As we have seen, contrasts grow and

so does the variance σ^2 , making the Gaussian distribution of Eq. (1.60) to broaden. Since σ cannot get under -1 , the distribution $\mathcal{P}(\delta)$ will be deformed asymmetrically, accumulating the probability near -1 without ever passing it. This agrees with simulations, where voids dominate volumes and overdense regions are limited to cosmic filaments and nodes. A different kind of function is therefore needed and may be found in the *log-normal distribution* (Coles and Jones, 1991), but we do not need to go further in this direction.

Again, considerations on primordial, inflation-induced fluctuations lead to assume $n = 1$ for the power spectrum, the so-called Zeldovich spectrum, meaning that small scale perturbations have more power, at least in the primordial situation. This primordial spectrum indeed is modified by physical features we have previously mentioned: smaller scales, which means higher k , enter the horizon sooner and, if before z_{eq} , are subject to stagnation. This makes the power spectrum to have a break at $k = k_{\text{eq}}$, that is the wavenumber of a perturbation that enters the horizon at the equivalence. The position of this break is sensible to Ω_m as more matter would shift the equivalence back in time and vice versa. So, whatever is n , one can demonstrate that the power spectrum, in CDM scenario, has the shape

$$P(k) \propto \begin{cases} Ak^n & k < k_{\text{eq}} \\ Ak^{n-4} & k > k_{\text{eq}}. \end{cases} \quad (1.61)$$

Observations tell us that $k_{\text{eq}} \simeq 2 \cdot 10^{-2} \text{ h Mpc}^{-1}$, which means that on scales smaller than $\sim 100 \text{ Mpc}$ the spectrum decreases with a trend that depends on whether the DM component is hot or cold. In fact, free-streaming dissipates scales under their M_{fs} . For HDM, which has free-streaming mass of $\sim 10^{15} M_{\odot}$, the effect is huge and the power law results steeper. The same effect on CDM is negligible as only scales under $\sim 10^6 M_{\odot}$ are cancelled and those are cosmologically irrelevant. The point is that observations on clusters and galaxies distributions are incompatible with HDM, while are in good agreement with the CDM case.

Non-linear evolution Current density contrasts in clusters are far over the fundamental condition of the linear theory, that is $\delta \leq 1$. Thus a nonlinear theory is necessary to describe the last phases of structure formation. The problem is that analytical models cannot admit exact solutions except for some ideal or non physical cases and need to be compared with numerical simulations. But these approaches are useful to highlight some properties and give a clue of how nonlinear overdensities evolve, thus we are qualitatively presenting some in this paragraph.

The first one considers a spherical perturbation which is in a linear regime at $t_i = t_{\text{rec}}$, with a constant initial contrast δ_i and an Einstein-de Sitter modelled background universe. The linear perturbation theory can give the evolution of such a perturbation as

$$\delta = \delta_+(t_i) \left(\frac{t}{t_i}\right)^{2/3} + \delta_-(t_i) \left(\frac{t}{t_i}\right)^{-1}, \quad (1.62)$$

where δ_+ and δ_- represent growing and decaying solutions respectively. It is clear that the decaying solution is going to be negligible as time passes. Another assumption is that the spherical overdensity is at rest with respect to the background expanding Universe. In the linear regime the velocity can be written as $v = ia\dot{\delta}/k_x$, where k_x is the wave number for a DM particle X . So the condition just mentioned translates in

$$v_{\text{pec}} = 0 = \frac{i}{k_x t_i} \left(\frac{t}{t_i}\right)^{-2/3} \left[\frac{2}{3} \delta_+ \left(\frac{t}{t_i}\right)^{-1/3} - \delta_- \left(\frac{t}{t_i}\right)^{-4/3} \right] \quad (1.63)$$

and thus, combining Eq. (1.62) and Eq. (1.63), we get

$$\delta(t_i) = \frac{5}{3} \delta_+(t_i). \quad (1.64)$$

A sufficient condition for the perturbation to collapse is that its initial density parameter Ω_p is bigger than 1 so that it can be treated as a closed universe. Because $\Omega_p(t_i)$ can be written as

$$\Omega_p(t_i) = \Omega(t_i)(1 + \delta(t_i)), \quad (1.65)$$

if the background universe is closed too, then every perturbation is going to collapse, otherwise a condition on δ_+ emerges:

$$\delta_+(t_i) > \frac{3}{5} \frac{1 - \Omega(t_i)}{\Omega(t_i)}. \quad (1.66)$$

If this condition is achieved, we expect that the spherical perturbation is expanding with the background universe until a time t_{\max} , called *turnaround*, when the expansion stops and the collapse starts. At this moment, the perturbation density $\rho_p(t_{\max}) = 3\pi/32Gt_{\max}^2$ can be compared with the background one to get a contrast

$$\delta_c^{nlin}(t_{\max}) \simeq 4.6 > \delta_c^{lin}(t_{\max}) \simeq 1.07, \quad (1.67)$$

that shows how the regime is already nonlinear at t_{\max} . The perturbation then would collapse into a singularity in $t_{\text{coll}} = 2t_{\max}$ as closed universes do, but pressure and shocks heat matter during the infall until the system reaches equilibrium at a certain t_{vir} . Applying the virial theorem, internal energy can be found as

$$E(t_{\text{vir}}) = -\frac{1}{2} \frac{3GM^2}{5R_{\text{vir}}}. \quad (1.68)$$

Assuming that neither energy or mass have been lost since t_{\max} , E_{vir} should be equal to

$$E(t_{\max}) = -\frac{3GM^2}{5R_{\max}} \quad (1.69)$$

and so we find that $R_{\text{vir}} = R_{\max}/2$, thus when $\rho_p(t_{\text{vir}}) = 8\rho_p(t_{\max})$. Moreover, numerical simulations show that $t_{\text{vir}} \simeq 3t_{\max}$. All these relations allow to estimate density contrasts at t_{coll} and t_{vir}

$$\delta_c^{nlin}(t_{\text{coll}}) \simeq 8 \left(\frac{\rho_p(t_{\text{to}})}{\rho(t_{\text{to}})} \right) \left(\frac{t_{\text{coll}}}{t_{\max}} \right)^2 \simeq 180, \quad (1.70a)$$

$$\delta_c^{nlin}(t_{\text{vir}}) \simeq 8 \left(\frac{\rho_p(t_{\text{to}})}{\rho(t_{\text{to}})} \right) \left(\frac{t_{\text{vir}}}{t_{\max}} \right)^2 \simeq 400. \quad (1.70b)$$

These values are much more realistic and near to observed density contrasts than those extrapolated from linear approximation

$$\delta_c^{lin}(t_{\text{coll}}) \simeq 1.68, \quad (1.71a)$$

$$\delta_c^{lin}(t_{\text{vir}}) \simeq 2.20 \quad (1.71b)$$

but the assumptions are strong: some nearly spherical perturbations may exist, as much as null peculiar velocities, but are limited for low mass instabilities and cannot be assumed for every perturbation present at t_{dec} , especially for those with big sizes. Moreover, it has been demonstrated that collapse is more likely to develop in a triaxial configuration, as the *Zel'dovich approximation* shows. In brief, it consists in a first-order Lagrangian perturbation theory, where the approximation is made on particle displacements instead of density. Without going into details, this approximation shows that collapse can happen at different velocities along three axis and that exists a moment called *shell-crossing*, when collapse has reached the singularity along one of the axis. This leads to almost two-dimensional configurations for

collapsed structure which are called *pancakes* and if shell-crossing happens for another axis, matter will be distributed in a filament. This result agrees with numerical simulations, where the matter slowly settles in cosmic filaments and nodes that form the so-called cosmic web. Although very instructive, even Zel'dovich approximation is limited to its assumptions and to big scales structures. These analytical approaches cannot compete with modern N-body simulations of structure formation, but are useful to understand the physics behind collapse.

1.3 DM in galaxies

In §1.1 we mentioned how [Rubin and Ford, 1970](#) provided an important evidence for the existence of DM from galaxies observations and showed that the dark component is dominant in terms of mass. In §1.2.2, we described how DM perturbations were born and grew before baryonic ones and allowed a faster evolution for these last. Thus exists a strong relation between a galaxy and its DM halo and, for the purposes of this thesis, it will be necessary to consciously assume a DM halo density profile for the dwarf spheroidal in exam. In order to do so, some related concepts are discussed in this section.

1.3.1 Mass function

Let us start with the basic concept of *luminosity function* $\Phi(L)dL$: it is defined as the number of galaxies per unit volume with luminosity in the interval from L to $L + dL$ so that, ideally, an integration on the whole luminosity range would give the number density of galaxies and the total luminosity of a sample may be found as

$$\mathcal{L}_g = \int_0^{\infty} \Phi(L)LdL. \quad (1.72)$$

The best fit analytical expression that better reproduces observations was already found by [Schechter, 1976](#) as

$$\Phi(L)dL = \Phi^*(L/L^*)^{-\beta} \exp(-L/L^*)d(L/L^*), \quad (1.73)$$

where Φ^* and L^* represent number density and luminosity at the break of the function, respectively. Qualitatively, the so-called *Schechter function* tells us that faint galaxies are dominant in number with respect to brighter ones. It is worth mentioning that many different kinds of luminosity function can be used, depending on the spectral band used or the sample choice made. Moreover, the function evolves with redshift because both mean density and mean luminosity were higher in the past. Anyway, since luminosity is a directly observable quantity, once we assume a redshift range, we are able to constraint parameters of the Schechter function.

We may be more interested in an analogous function, the *mass function* $n(M)dM$, that is the number of galaxies per unit volume with mass in the interval between M and $M + dM$. Its relation with the luminosity function is described by the fundamental *mass to light ratio* M/L . Indeed, for a given M/L , mass and luminosity functions provide the same information as

$$\Phi(L) = n(M) \frac{dM}{dL} \simeq n(M) \left\langle \frac{M}{L} \right\rangle. \quad (1.74)$$

Because mass is far more difficult and laborious to be determined observatively, one could try to get $n(M)$ out of $\Phi(L)$ by assuming M/L . The problem is that the mass to light ratio is hard to predict and has a wide range of values, depending on the galaxy type, its evolutionary history and the redshift. Recovering a mass function from the luminosity one is therefore unfeasible. It becomes useful to have a theoretical analytical model such as the one developed by [Press and Schechter \(1974\)](#). In order to discuss it, we need to recall Eq. (1.60) and the

fact that the distribution $\mathcal{P}(\delta)$ becomes non Gaussian as perturbations grow. Indeed, the probability of a perturbation δ leading to a collapsed structure is given by

$$P_{>\delta_c}(M) = \int_{\delta_c}^{\infty} \mathcal{P}(\delta) d\delta \quad (1.75)$$

and this can be connected to the mass function through the relation

$$n(M)dM = 2\frac{\bar{\rho}_m}{M}[P_{\delta_c}(M) - P_{\delta_c}(M + dM)] = 2\bar{\rho}_m \left| \frac{dP_{>\delta_c}}{d\sigma_M} \right| \left| \frac{d\sigma_M}{dM} \right|. \quad (1.76)$$

The problem is that one should assume a distribution for the non-linear regime and integrate starting from the critical value obtained in Eq. (1.70) in order to get $P_{>\delta_c}$, but such calculations are difficult to perform. Press and Schechter adopted an original approach by using a Gaussian distribution instead and integrating from the linear regime value of Eq. (1.71). In fact, in a linear regime, a Gaussian distribution remains Gaussian when perturbations grow and it only changes its width. These two improprieties seem to balance one another and lead to results in agreement with numerical simulations. An additional but more logic assumption is that the variance is a power law $\sigma_M = (M/M_0)^{-\alpha}$ where $\alpha = (n + 3)/6$ from Eq. (1.59), which makes Eq. (1.76) simpler:

$$n(M)dM = \frac{2}{\sqrt{\pi}} \frac{\rho_m \alpha}{M_*^2} \left(\frac{M}{M_*} \right)^{\alpha-2} \exp \left[- \left(\frac{M}{M_*} \right)^{2\alpha} \right] dM \quad (1.77)$$

where $M_* \equiv (2/\delta_c^2)^{1/2\alpha}$ sets the exponential break. It is evident that, if one assumes a constant M/L for mass variations, equation Eq. (1.77) reproduces the Schechter function Eq. (1.73). If the β parameter of the luminosity function is ~ 1 , the Schechter function is said to be flat and in this case we need $\alpha - 2 = -1$, thus $\alpha = 1$ in order to overlay mass and luminosity functions. This would mean that $n = 3$, but the predicted value for the power spectrum of CDM halos at the galaxy scale is $n \sim -2$. This incompatibility is to be addressed to the fact that not every DM halos contain a galaxy. Moreover, numerical simulations shows that the Press and Schechter approach overestimates the number of small halos and this may be due to the spherical collapse assumption. In fact, introducing ellipsoidal collapse in simulations adds free parameters and allows to get a better fit (e.g. [Sheth and Tormen, 2002](#)).

It is already clear that many of the properties of DM halos emerge from those simulations that, given a set of cosmological parameters, better reproduce observational data and the hierarchical scenario we expect. Without going into the huge variety of technical approaches, we are just taking the results we need to describe the state-of-art properties of DM halos. To do so, we first define properly the mass and radius of a halo. Some definitions are still based on the spherical collapse model as we assume that, once an overdensity reaches its turnaround point, it collapses until virialization. At this time, $R_{\text{vir}} = R_{\text{max}}/2$ and the density is expected to be close to $200\rho_{\text{crit}}$, but it has been shown ([Diemand and Kuhlen, 2008](#)) that matter orbits extend far beyond R_{vir} and several other problems may be summoned to stand that a common definition is unlikely to be found.

1.3.2 Density profiles

In order to refer to different definitions of radius and mass, it is customary to use, for example, R_{200} to indicate the radius of a sphere with an average density $\bar{\rho} = 200\rho_{\text{cr}}$. With this convention, we get smaller and smaller radius by using greater and grater pedices, such that an R_{2500} refers to a small sphere containing a very overdense region. The definition of a halo mass is therefore simple as we can use M_{200} to indicate the mass within a radius R_{200} . With these conventions, we now need consciously assume a theoretical density profile for DM halos

which will be fundamental for the purpose of this thesis. We remember that a density profile can be associated to a velocity dispersion profile or to the circular velocity one through the relation $V_c^2 = GM(r)/r$, from which estimated profiles can be obtained for example for spiral galaxies. The peak value of circular velocities V_{max} defines a radius R_{vmax} over which velocities fall and sets a characterizing scale for each halo. Another important quantity, which describes the concentration of a halo, can be defined as

$$c_V \equiv \frac{\rho(< \bar{R}_{\text{vmax}})}{\rho_{\text{cr},0}} = \frac{3V_{\text{max}}^2}{4\pi G\rho_{\text{cr},0}R_{\text{vmax}}^2}. \quad (1.78)$$

The importance of this concentration parameter is due to the fact that DM halos, which form through fluctuations growth as described in § 1.2.2, are not affected by microphysics effects such as the baryonic component of galaxies and hence are likely to share same density profiles at any scale, from the biggest of cluster one to that of micro-halos. Concentrations instead are sensible to the formation history of the structure. In fact, the mass variance σ_M depends on the original mass (see Eq. (1.59)) such as small structures, on average, have formed earlier and thus they were born in a denser universe. This causes smaller halos to have greater median c_V at $z = 0$. But which density profile better reproduces simulated or observed distributions?

Considering perfectly spherical halos, a classical profile may be found in that of the Singular Isothermal Sphere model (SIS) which, by assuming equilibrium between gravitational and kinetic pressures, simply gives

$$\rho(r) = \frac{\sigma_V^2}{2\pi Gr^2}. \quad (1.79)$$

This basic model is unphysical because of the singularity at zero radius and the divergence of mass for $r \rightarrow \infty$. Anyway, it does not fall far from the simulated ones and it resembles observed profiles properly. N-body simulations over a large scale range of halos led [Navarro et al. \(1996\)](#) to propose the so-called Navarro-Frenk-White (NFW) profile:

$$\rho_{\text{NFW}}(r) = \frac{\rho_s}{(r/R_s)^\gamma(1+r/R_s)^{3-\gamma}}, \quad (1.80)$$

where $\gamma = 1$ in the original version. This expression is characterized by a scale radius which is related to the circular velocity one as $R_{\text{vmax}} = 2.163R_s$ and ρ_s is the density at this radius. A relative concentration parameter can be defined as $c_{\text{vir}} \equiv r_{\text{vir}}/r_s$ and can be compared with c_V : this last is surely more general and reliable since c_{vir} is subject to a fitting procedure in simulations ([Bullock et al., 2001](#)). The NFW profile seemed to be the best-fit function for most of the simulated halos but a controversy arose between simulators and observers. The former, whose simulations were getting better and better, started to obtain steeper profiles than that of NFW for central regions, for example with the [Moore et al. \(1998\)](#) value of $\gamma = 1.5$. In the meanwhile, observers reconstructed several rotation curves of dwarfs and low brightness spirals, finding that they indicated flat core profile, e.g. with $\gamma = 0$ ([McGaugh and de Blok, 1998](#)). In another work [Moore \(1994\)](#) underlined how these observational results could put some doubts on the CDM paradigm as simulations were obtaining opposite results. In the successive years, enhancing rotational curve precision, it became evident that Moore's and, in many cases, the NFW profiles were inadequate to reproduce the observed cores. Then simulators showed that the alternative [Einasto \(1968\)](#) profile

$$\rho_E(r) = \rho_s e^{-\frac{2}{\alpha}[(r/R_s)^\alpha - 1]} \quad (1.81)$$

with $\alpha \simeq 0.17$ could better reproduced the observed slopes and the reason because CDM simulated halos failed central regions resemblances was attributed to the dominant presence of baryons at these radius. Different phenomena like Supernova and AGN feedback ([Pontzen and Governato, 2012](#)) could justify flat cores but our knowledge of the interactions between DM

halos and baryons is still not complete. With smaller halos like those of dwarf galaxies, the main problem keeps consisting in the incapacity of current simulations to resolve such small scales. [Burkert \(1995\)](#) conducted a study on dwarf halos and presented another profile, with a shallow central region

$$\rho_B(r) = \frac{\rho_s}{(1 + r/R_s)[1 + (r/R_s)^2]}, \quad (1.82)$$

which can properly fit observational data.

1.3.3 Dwarf Spheroidals

As Eq. (1.73) and Eq. (1.77) clearly show, faint ($\mathcal{M} \geq -18$), small-size galaxies dominates the number density of galaxies in the universe. Of course, their low luminosity makes them hard to be detected and studied, such that most of the known dwarf galaxies are satellites of the Milky Way or Andromeda, enclosed into the Local Group. Except for the Large and Small Magellanic Clouds, which fall under the Hubble class of Dwarf Irregulars (dIrr), all other satellites are classified as Dwarf Spheroidals (dSph). These faint systems have metal poor stellar populations, in fact it is customary to consider that, among small size DM halos, only the eldest ones could attract enough baryons to trigger star formation. Thus, the stellar populations of these objects are old and all the gas which fell into the potential well has been processed long time ago. In fact, stars represent the only emission and the presence of interstellar medium seems negligible, if there is any. This made dwarfs difficult to be found, such that the first one discovered, the Sculptor, was found by [Shapley \(1938\)](#). Since then, tens more dSph has been unveiled, many of them thanks to the SDSS² survey at the beginning of this century and several more have been found later. In the first data release of SDSS, an even fainter class ($L < 10^5 L_\odot$) of dwarfs has been discovered and they are now classified as Ultra-Faint Dwarfs (UFD). A dedicated review has been published by [Simon \(2019\)](#), while an extended, recent census of Local Group satellites can be found in [Drlica-Wagner et al. \(2020\)](#).

These objects (both 'classical' and ultra-faint dwarfs) can be identified in surveys as old, concentrated stellar populations and they appear not very different from globular clusters (GC). Both GCs and dSphs are gas poor and do not present evidences of current star formation. To distinguish between these two categories, an effective method is to compare the half-light radius r_h for systems at the same luminosity: GC characteristic half-light radius is about 10 pc while dSph one spans from 20 to 500 pc. In fact, the intrinsic difference between these two classes of systems is the presence of a mass dominating DM halo. From spectroscopic studies, the velocity dispersion is similar for both (5–15 km s⁻¹) but the difference between half-light radius, thus the difference of sizes, proves that GC are dominated by the stellar mass while dSph are dominated by their DM halos, for a characteristic mass of $10^7 M_\odot$. Equivalently, dSphs present mass-to-light ratios an order of magnitude greater than those of GCs. Anyway, spectroscopic studies usually do not reach great statistics, so that precise radial distribution profiles are hard to be reconstructed without some model dependencies. As we will better explain in § 2.1, the characteristic features of dSphs now exposed make these systems the best candidate targets for many DM detection attempts, including the one discussed in this Thesis.

²SDSS website: <https://www.sdss.org>

Chapter 2

Particle DM detection

In the context of the Standard Cosmological Model Λ CDM, a consistent fraction of the Universe is made of a DM component ($\Omega_{\text{DM}}h^2 = 0.120$, for [Aghanim et al. \(2020\)](#)). This is considered to be a cold component, meaning that DM particles are already non relativistic at the moment of their decoupling from radiation. As explained in § 1.2.2, assuming the typical annihilation cross section for the electroweak scale ($\langle\sigma_{\text{a}}v\rangle \sim 3 \cdot 10^{-26} \text{ cm}^3 \text{ s}^{-1}$), we get to resemble the current relic abundances. In this context, a lower limit for the mass of CDM particles can be established at the GeV scale. From a cosmological point of view, the most relevant DM properties are its mass particle and cross section, and most astrophysical searches, including this Thesis work, aim to constrain these parameters.

From the perspective of particle physics, any new particle should respond to the theoretical framework of the Standard Model, or an extension of it. Just to mention an example, in the Supersymmetry (SUSY) context there are some theoretical particles, such as the *supersymmetric neutralino*, which are considered as possible DM candidates ([Masiero et al., 2005](#)). The SUSY theoretical scenario is investigated with some of the most ambitious experiments of this era, such as the Large Hadron Collider at CERN, which aims to discover new particles. However, the discovery of any new particle, even if a DM candidate, would not mean that the Dark Matter which populate the Universe is made of those particle; a direct or indirect detection of astrophysical DM would still be needed in order to obtain complementary information and determine if produced and detected particles are the same species.

Since the purpose of this Thesis is to observe radiation due to secondary products of DM eventual annihilations (or decays), it is to be considered as an indirect detection technique. In the following we describe methods of direct and indirect detection of DM particles, with particular attention to radio astronomical probes. From now on, we are only considering the WIMP hypothesis for DM candidates.

Direct detection Any direct approach aims to detect WIMPs that flow through the Earth with underground particle detectors, in particular via elastic scattering with nuclei and the resulting nuclear recoils (e.g., [Widrow et al., 2008](#); [Read, 2014](#)). Given the MW DM halo, a flux of $10^5 \text{ cm}^{-2} \text{ s}^{-1}$ particles of typical mass of a WIMP candidate ($\sim 100 \text{ GeV}$) is estimated ([Goodman and Witten, 1985](#)). Most of the following discussion follows [Bertone and Hooper \(2018\)](#), in particular their Chapter 17. The theoretical event rate can be computed by integrating the differential event rate over all the recoil energies, where the lower limit is given by the smallest recoil energy detectable E_{T} . The differential event rate dR/dE_{R} can be written as

$$\frac{dR}{dE_{\text{R}}} = \frac{\rho_0}{m_N m_{\chi}} \int_{v_{\text{min}}}^{v_{\text{esc}}} v f(v) \frac{d\sigma_{\text{WN}}}{dE_{\text{R}}} dv, \quad (2.1)$$

where $d\sigma_{\text{WN}}/dE_{\text{R}}$ is the differential cross-section for a WIMP-nucleus encounter and represents the quantity to be constrained. M_N , M_{χ} and ρ_0 are respectively the neutron mass, the WIMP

mass and the local WIMP density. The differential cross section is weighted by the WIMPs velocity distribution $f(v)$ relative to the laboratory frame and integrated over the velocity range v_{\min} , the minimum speed that causes a recoil, and v_{esc} , the MW escape velocity. The velocity distribution and ρ_0 are significantly affected by uncertainties in the DM halo model (Petač et al., 2018).

From an observational point of view, DM-induced nuclear recoils can be detected with underground scintillators. Among these instruments, the DAMA/LIBRA experiment (Drukier et al., 1986) is the only one that have claimed a detection of a DM signature so far. The experiment is located at the Gran Sasso National Laboratory of the INFN and consists of a heavy scintillator made of sodium iodide (NaI), doped with thallium (Tl) and placed deep underground. The claimed detection is based on the annual modulation of the event rate: since the Earth revolves around the Sun, its velocity with reference to the galactic centre changes throughout the year, by a factor of $\pm 30 \text{ km s}^{-1}$, leading to a modulation of the velocity distribution $f(v)$, and, eventually, the differential event rate.

While direct detection techniques belong to the realm of particle physics, astrophysical observations allow the detection of secondary products of DM annihilations/decays coming from celestial sources (Gunn et al., 1978). Target of astrophysical observations would then be sources with a large DM component from which γ , X-rays and relativistic electron-positron pairs can be produced. In § 2.1 we will describe DM searches using high energy photons, and using radio observations in § 2.2.

2.1 Indirect detection with high-energy photons

WIMPs can annihilate (or decay) into Standard Model particles directly or indirectly (Pospelov et al., 2008). Given that WIMPs are hypothetical particles, there is not, in principle, a favourite channel for their annihilation. Thus we can expect them to produce whichever of the known particles of the Standard Model as primary products; some of the mainly considered particles are quarks ($b\bar{b}$), leptons (τ^\pm , μ^\pm) or bosons (W^\pm). In any case, in terms of energy, nearly 100% of the final products of an annihilation are e^+/e^- and γ -ray photons (Leane et al., 2018). By assuming the primary product and the WIMP mass (M_χ), we are able to obtain photon spectra by means of Monte Carlo event generators and dedicated software (Bringmann et al., 2018, e.g. DarkSUSY) as final products (Cembranos et al., 2011). Potential detection of a signal from DM annihilation would instead be able to determine which channel better fits that signal.

These photon spectra often present a relevant component of γ rays. The flux of high-energy photons Φ_γ , expressed in $\text{cm}^{-2} \text{ s}^{-1} \text{ sr}^{-1}$, can be written as (Bergström et al., 1998):

$$\Phi_\gamma = \frac{N_\gamma \sigma v}{4\pi M_\chi^2} \mathcal{J}, \quad (2.2)$$

where N_γ is the number of γ ray photons produced per annihilation, σv is the product of the cross-section and particle velocity, and M_χ the WIMP mass, which comes in squared because the process involve two χ particles. These three terms characterize the DM particle and are the quantities we would like to constrain. The last term in equation 2.2 is the so-called \mathcal{J} -factor (Evans et al., 2016):

$$\mathcal{J} = \iint_{\text{los}} \rho_\chi^2(l) dl d\Omega, \quad (2.3)$$

namely the integral of the squared DM density ρ_χ over the line of sight dl and the instrument resolution $d\Omega$.

Estimates of \mathcal{J} -factors (and the following \mathcal{D} -factors) are often uncertain, due to the fact that DM density profiles have large parameters space and uncertainties. Often, such as with dwarf spheroidal galaxies, the task is even more complicated because of poor spectroscopic

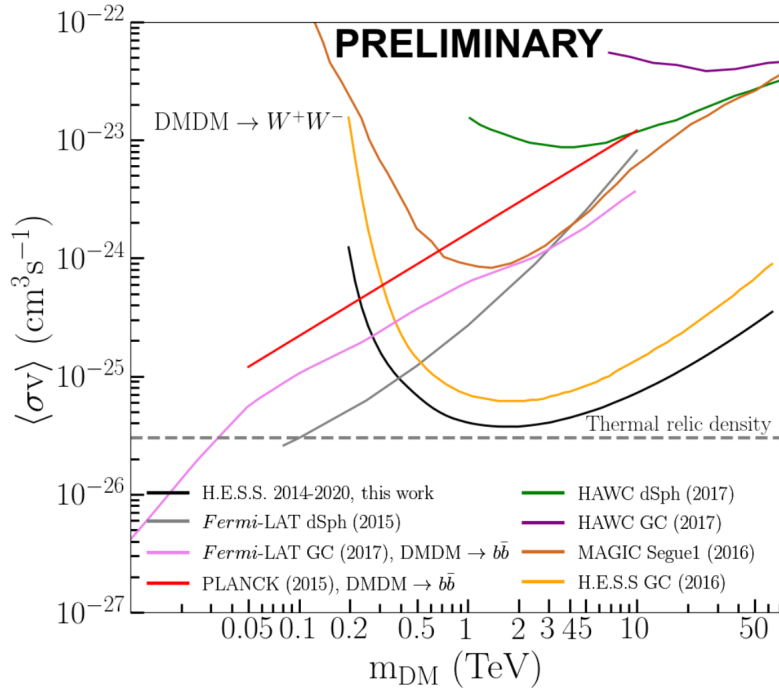


Figure 2.1 Upper limits (95% C.L.) on DM annihilations (W^\pm channel; Montanari et al., 2021).

data of the stellar population, but with simplified formulas (see Evans et al., 2016) one can still obtain reliable values.

In case of DM decay, equation 2.2 becomes (Bergström et al., 1998):

$$\frac{d\Phi_\gamma}{dE} = \frac{1}{4\pi M_\chi \tau_\chi} \frac{dN_\gamma}{dE} \mathcal{D}, \quad (2.4)$$

where the decay time τ_χ replaces the cross-section and the flux just depends on m_χ^{-1} as the process involves only one particle. In this case the \mathcal{D} -factor is (Evans et al., 2016):

$$\mathcal{D} = \iint_{\text{los}} \rho_\chi(l) dl d\Omega, \quad (2.5)$$

and is proportional to the density.

The two channels through which high energy photons can be produced - either annihilation or decay - lead to different searches in terms of astrophysical targets: high density environments are optimal targets to look for DM annihilation, in particular the Galactic centre (GC), which has the highest J-factor due to the large solid angle and may host a cusp-core halo profile which would enhance the signal (e.g., Bertone et al., 2002). Even though any current attempt to interpret high energy signals from this region as due to DM has failed (e.g., Profumo, 2005), bounds on WIMPs parameter space have been obtained with different instruments. Among several attempts, best results has been obtained with HAWC (Abeysekara et al., 2018), Fermi-LAT (Ackermann et al., 2017) - which also excluded WIMP masses below 30 GeV for the $b\bar{b}$ channel - and HESS (Abdallah et al., 2016). Another recent work (Montanari et al., 2021) has been made with HESS, lowering bounds on the same mass range (these are claimed to be preliminary results). Figure 2.1 shows bounds of these researches.

Conversely best targets to measure DM decay signals are regions with lower densities, like dwarf galaxies (Ruchayskiy et al., 2016) or the diffuse galactic halo (Borriello et al., 2009). In the next section we will describe past searches carried in dwarf galaxies, which are the targets of the present work too. Some of the papers cited in Figure 2.1 will be presented there.

2.1.1 Local Group Dwarfs

Dwarf spheroidal (dSph, DSph) galaxies in our Local Group have been recognized early as some of the most promising objects to constrain the nature of DM particles (Lake, 1990). DSph galaxies have old, metal-poor stellar populations with dynamical properties governed by the DM halo. They show no sign of star formation and negligible amount of interstellar gas in any phase. These characteristics suggest that negligible radio emission is expected from dSph galaxies. At the same time, negligible γ ray emission is also expected due to the lack of star-formation induced supernova remnants and the absence of a central supermassive black hole.

In order to predict the emission due to either DM annihilation or decay, \mathcal{J} and \mathcal{D} factors need to be estimated. This is often done by means of spectroscopic stellar observations, which are particularly difficult to perform on dSphs due to their faintness and the small number of stars in these objects (e.g., Strigari, 2018). The stellar kinematics allows to reconstruct DM density profiles, thus to constraint \mathcal{J} and \mathcal{D} .

The search for high-energy signals from dSphs is usually performed on most promising targets, with both ground-based Cherenkov telescopes and space telescopes. Up to date, Geringer-Sameth et al. (2015b) claimed a detection in the MW satellite Reticulum II using Fermi-LAT observations. The reported signal is ($>3.7\sigma$) with DM annihilation for particle masses below few 100 GeV. While the result has been confirmed by Hooper and Linden (2015), other Fermi-LAT collaboration papers do not consider it statistically significant (Drlica-Wagner et al., 2015).

Paper	Instrument	Channel	$\langle\sigma v\rangle$ [$\text{cm}^3 \text{s}^{-1}$]	M_χ [TeV]
Abramowski et al. (2014)	HESS	$\tau^+\tau^-$	$3 \cdot 10^{-24}$	1
Acciari et al. (2010)	VERITAS	$\tau^+\tau^-$	$3 \cdot 10^{-24}$	0.3
Albert et al. (2018)	HAWC	$\tau^+\tau^-$	$3 \cdot 10^{-24}$	0.3
Aleksić et al. (2011)	MAGIC, Fermi-LAT	$b\bar{b}$	$3 \cdot 10^{-25}$	1
Geringer-Sameth et al. (2015a)	Fermi-LAT	$b\bar{b}$	$3 \cdot 10^{-26}$	< 0.1

Table 2.1 Best upper bounds from high energy observations. All the limits mentioned above are at 95% C.L.

In any other case, no detection are reported, placing upper limits in the cross section-mass diagram. Table 2.1 list the best results to date, with the most stringent limit being $\langle\sigma v\rangle \sim 3 \cdot 10^{-26} \text{ cm}^3 \text{ s}^{-1}$ for particles below 100 GeV for the $b\bar{b}$ annihilation channel (Geringer-Sameth et al., 2015a).

2.2 Indirect detection with radio signatures

Electrons and positrons are among the most common secondary products of DM annihilations and decays (e.g. Regis and Ullio (2008); Fig. 4). Of course, given the mass range for the most reliable DM candidate particles (GeV-TeV scale), light particles like electrons are expected to be produced at relativistic energies. In turn, such a population would be able to generate synchrotron emission in the presence of a magnetic field and this is the signal that radio observations aim to detect.

2.2.1 From annihilations to synchrotron radiation

In this section we are characterizing the most important quantities which allow to relate the synchrotron emission with the annihilation/decay and the consequent diffusion of an

ultrarelativistic electron population. These theoretical models represent the framework at the foundation of almost every research work presented in the following section, but we already highlight the aspects related to observations on dSphs. Specifically, the following discussion follows [Regis et al. \(2015b\)](#), the second paper of a series discussed in § 2.2.2, when not indicated otherwise. A summarizing scheme can be found in Figure 2.2 and can be used to better understand the modeling process.

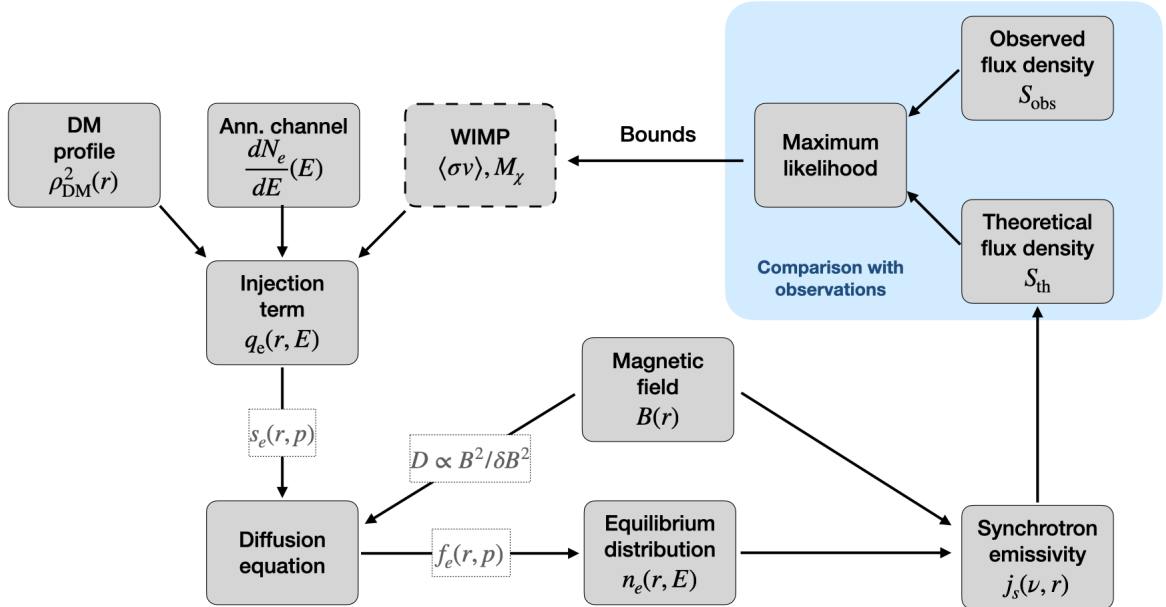


Figure 2.2 A summarizing scheme for the modeling process. It has to be read starting from the top left corner, where the DM profile, the annihilation channel and WIMP parameters are used to calculate the injection term. The light blue box includes the statistical analysis that leads to obtain bounds for WIMP parameters. It will be described in § 4.2.

Electron injection. The injection of ultrarelativistic electrons (and positrons) in the interstellar medium depends on the DM number density, which can be expressed as the ratio between the actual density ρ and the particle mass M_χ , and the number of electron-positron pairs e^+/e^- produced. In the case of annihilation, the injection term q_e^a as a function of radial coordinate r and energy E can thus be written as:

$$q_e^a(r, E) = \langle\sigma_a v\rangle \frac{\rho^2(r)}{2M_\chi^2} \cdot \frac{dN_e^a}{dE}(E), \quad (2.6)$$

where the differential term dN_e^a/dE is the number of e^+/e^- produced per annihilation and per energy interval $(E, E + dE)$. It is calculated with spectra for every possible annihilation channel, weighted for the corresponding branching ratio. For the decay hypothesis, which involve just one particle, the injection term q_e^d becomes:

$$q_e^d(r, E) = \Gamma_d \frac{\rho(r)}{M_\chi} \cdot \frac{dN_e^d}{dE}(E), \quad (2.7)$$

where Γ_d is the decay rate.

Among the quantities included in the above equations, the number of electrons/positrons produced per annihilation (decay) characterizes the DM candidate properties. For example,

an annihilation (decay) into leptons (τ^\pm or μ^\pm) leads to e^\pm production through direct decays, resulting in steep energy spectra; otherwise, if the preferred channels are quarks ($b\bar{b}$) or weak gauge bosons (W^\pm), energy spectra are flatter and the production of e^\pm is reached through chains of hadronizations and decays.

The astrophysical input is the density profile of the DM halo. In the case of dSphs, density profiles are obtained with a two-component (stars and DM) model whose parameters are constrained by spectroscopic observations (e.g., [Chang and Necib, 2021](#)).

Diffusion equation. After electron-positron pairs are injected due to annihilation/decay, they can spatially diffuse in the gravitational potential of the galaxy. Under the assumption of spherical symmetry and stationary state, the equilibrium density n_e of the electron/positron population is described by the transport equation:

$$-\frac{1}{r^2} \frac{\partial}{\partial r} \left[r^2 D \frac{\partial f_e}{\partial r} \right] + \frac{1}{p^2} \frac{\partial}{\partial p} (\dot{p} p^2 f_e) = s_e(r, p) \quad (2.8)$$

where $f_e(r, p)$ is the electron-positron distribution function at the equilibrium at a given radius r and momentum p , and s_e is the source function of electron-positron. The electron density is related to the momentum as:

$$n_e(r, E) dE = 4\pi p^2 f_e(r, p) dp, \quad (2.9)$$

and the source function to the injection term as:

$$q_e(r, E) dE = 4\pi p^2 s_e(r, p) dp. \quad (2.10)$$

The first term on the left hand side of equation 2.8 characterizes the diffusion of the e^-/e^+ population through the diffusion coefficient D .

The main process to account for is due to hydromagnetic waves propagating in the interstellar medium. These are able to scatter charged particles, reducing their capacity of escaping the galaxy and their efficiency in confining cosmic rays is related to the turbulence properties of the magnetic field. In this context, three distinctive scenarios can be considered:

- **Standard diffusion:** the standard scenario, which applies for example to the MW, is that of a moderate turbulence which allows CRs to diffuse on a scale similar to the host galaxy. The diffusion coefficient can be written, in the quasi linear approximation, as:

$$D = \frac{v r_g^\alpha}{3(1-\alpha)} \frac{B^2}{k_L^{1-\alpha} \delta B_L^2} \quad (2.11)$$

where r_g is the gyroradius, while k_L and B_L are, respectively, the wavenumber and the random magnetic field for a certain normalization choice. The diffusion coefficient can then be computed with the ratio between the coherent and the turbulent components of the magnetic field $B/\delta B$. This quantity, estimated for the Local Group galaxies, gives a typical value of $D_0 = 3 \cdot 10^{28} \text{ cm}^2 \text{ s}^{-1}$.

- **Free-escape:** if turbulence is absent or, more likely, very weak, CRs are free to move into almost straight lines at ultrarelativistic velocities and escape the system in relatively short times. In this case, the second term of Eq. (2.8), which accounts for energy losses of electrons, can be neglected. In fact, the main process through which electrons lose their energy is the synchrotron emission we aim to detect. With free-escaping, charged particles are barely decelerated moving along the object and most of their energy is

carried out. One can get an upper limit of $10^{32} \text{ cm}^2 \text{ s}^{-1}$ (at 1 GeV) for the diffusion coefficient by imposing the diffusion velocity to be smaller than the speed of light:

$$v_d = \frac{L}{\tau_d} \sim 10^{-4} c \left(\frac{D}{10^{28} \text{ cm}^2 \text{ s}^{-1}} \right) \left(\frac{\text{kpc}}{L} \right). \quad (2.12)$$

This scenario is actually unlikely, due to the self-induced scatter that CRs would produce when moving faster than the Alfvén speed (Cesarsky, 1980) and it can, therefore, be considered as the most pessimistic case.

- **Loss-at-injection:** the opposite scenario is the case of an intense, turbulent magnetic field which causes electrons to be confined near where they were injected. In this case, they radiate synchrotron emission losing most of their energy without actually diffusing, such that the first term of Eq. (2.8) can be neglected. A lower limit on the diffusion coefficient of $10^{26} \text{ cm}^2 \text{ s}^{-1}$ (at 1 GeV) can be obtained by imposing that the diffusion time is shorter than the age of the universe:

$$\tau_d \sim \frac{L^2}{D} \sim 10^{15} \text{ s} \left(\frac{L}{\text{kpc}} \right)^2 \left(\frac{10^{28} \text{ cm}^2 \text{ s}^{-1}}{D} \right). \quad (2.13)$$

In this scenario, the presence of a cusp in the DM radial distribution would lead to a cusp in the flux density profile.

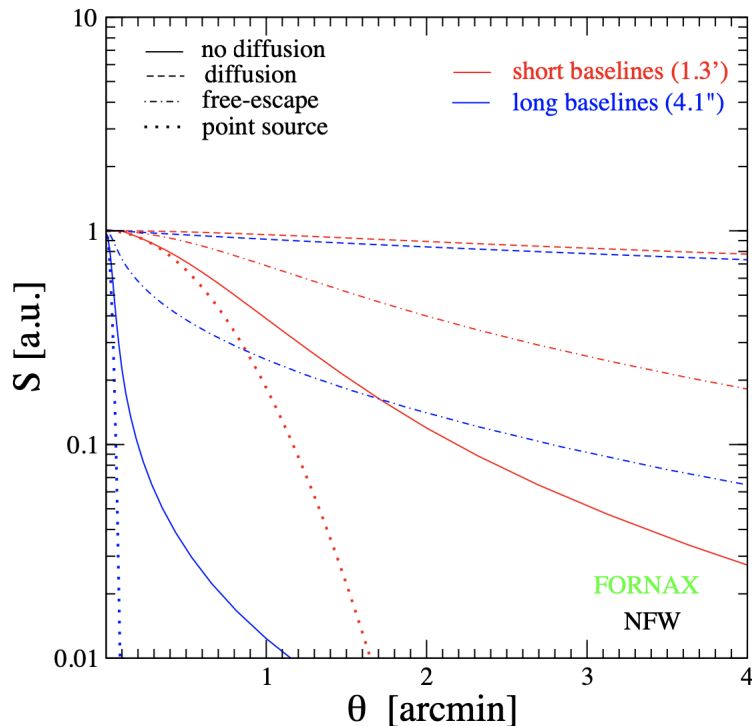


Figure 2.3 Expected flux density as a function of radial distance from the centre for the Fornax dwarf galaxy, assuming a NFW profile (arbitrary units). Profiles are shown for different resolutions (colors) and diffusion scenarios (line style; Regis et al., 2014).

Figure 2.3 shows how the emission remains fairly constant up to a few arcmin distance from the centre in case of standard diffusion (dashed line). Conversely, the emission drops by an order of magnitude already a couple of arcminutes away from the centre in the case of loss-at-injection (solid line). In the case of free-escape (dashed-dotted), the emission is

fainter than the standard case because particles are weakly decelerated. The effects of different scenarios are amplified by the fact that a cuspy DM profile (NFW) is used. It is evident how different diffusion scenarios can influence the theoretical flux density. We will see how this is reflected in terms of bounds in § 4.3.1.

Synchrotron emission. Synchrotron emission is generated when ultrarelativistic electrons are accelerated in a magnetic field. The emissivity $j_s(\nu, r)$ for a given electron population $n_e(r, E)$ is (Rybicki and Lightman, 1986):

$$j_s(\nu, r) = \int dE P_s(\nu, r, E) n_e(r, E), \quad (2.14)$$

namely the integral over energy range of the electrons distribution times the emission power P_s , which can be written as:

$$P_s(\nu, r, E) = \frac{\sqrt{3}e^3}{m_e c^2} B(r) F(\nu/\nu_c). \quad (2.15)$$

Here, $F(\nu/\nu_c)$ represents the spectral behaviour of the synchrotron radiation with ν_c being the critical frequency:

$$\nu_c \equiv \frac{3ce}{4\pi(m_e c^2)^3} B(r) E^2. \quad (2.16)$$

The radial profile of the magnetic field intensity $B(r)$ is one of the most uncertain parameters to be determined. For the case of dSph galaxies, complex mechanisms such as the thermal or synchrotron self-absorption can be neglected due to the lack of interstellar gas and the sparseness of the emitting region, respectively. The proximity of dSphs also allows to exclude intergalactic absorption. The theoretical flux density is obtained by integrating the emissivity over the interested volume, and can be measured by a radiotelescope as:

$$S_{\text{th}}(\nu, \theta_0) = \iint d\phi d\theta \sin \theta G(\theta, \phi, \theta_0) \int ds \frac{1}{4\pi} j_s(\nu, r(s, \theta, \phi)), \quad (2.17)$$

where angular coordinates (θ, ϕ) and the line-of-sight coordinate s are introduced, with θ_0 being the direction of the center of the source and $G(\theta, \phi)$ as the instrument response, typically an elliptical Gaussian centered in θ_0 .

The theoretical flux density is the final product of the modeling process. In Figure 2.4 we show an example of how the theoretical signal would appear in an actual observation (Regis et al., 2014).

In the statistical analysis that we describe in § 4.2, the expected signal is compared with observational data in terms of flux density distribution. This is the crucial part of the work as it allows to set bounds on WIMP parameters, as outlined in the scheme of Figure 2.2.

Now, we complete the description of the modeling process with the role of the magnetic field.

Magnetic field. As suggested in the previous paragraphs, the determination of magnetic field properties is fundamental to characterize both the diffusion mechanisms (Eq. (2.8)) and the theoretical synchrotron emission (Eq. (2.15),(2.16)). It is hard to characterize the magnetic field in dSphs: these are gas poor objects that do not present magnetic driven emission mechanisms (except, perhaps, the one we look for) and thus the most common ways to determine the local field are unfeasible. Another possibility could be to observe the rotation measure RM from background sources (Rybicki and Lightman, 1986):

$$\text{RM} = \frac{2\pi e^3}{m^2 c^2 \omega^2} \int_0^D n_e B_{\parallel} dl, \quad (2.18)$$

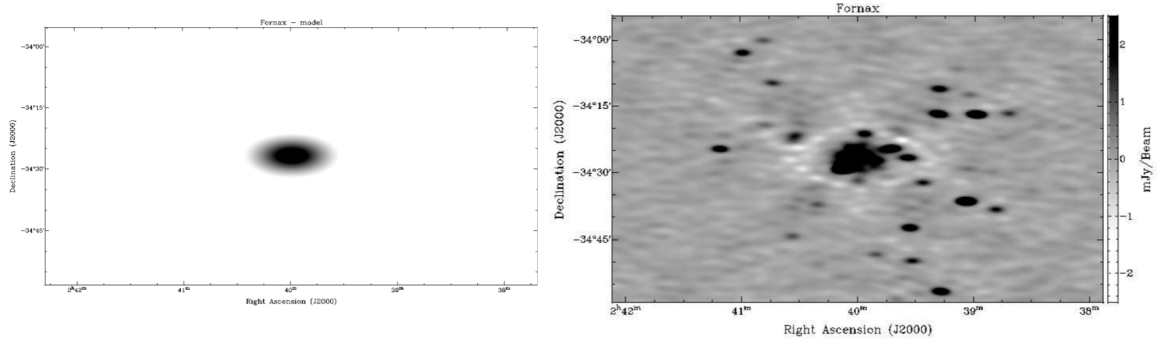


Figure 2.4 Left panel: expected signal for the Fornax dwarf, modelled with $M_\chi = 100$ GeV, $\langle\sigma v\rangle = 10^{-25}$ cm³ s⁻¹, $B_0 = 1$ μ G and a Burkert profile. Diffusion is neglected. Right panel: the same signal is injected in an actual image and it can be seen its detectability (Regis et al., 2014).

which depends on the electron density n_e . This is in turn a difficult quantity to constraint for dSphs: an estimate can be made through X-ray observations of thermal bremsstrahlung, whose non-detection places a 10^{-6} cm⁻³ limit on the electron density (e.g., Zang and Meurs, 2001). This value is just a factor of three higher than the cosmological density ($3 \cdot 10^{-7}$ cm⁻³) leading to a rotation measure values too small to be detected in current observations (Stasyszyn et al., 2010).

In absence of direct measurements, there are a few indirect ways to estimate the magnetic field. A scaling relation has been found by Chyży et al. (2011) between the star formation rate (SFR) density (Σ_{SFR}) and the magnetic field intensity in dwarf irregular galaxies in the Local Group, $B \propto \Sigma_{\text{SFR}}^{0.3}$. The turbulence introduced by supernova explosions is usually considered as the main source of the magnetization of a galaxy, together with dynamo processes, therefore, a strong relation between SFR and the magnetic field is expected, although it cannot be firmly established for dSphs. On the other hand, dSphs hosted star formation episodes in the past and a magnetic field could have formed, like the case of dwarf irregular galaxies (Calura et al., 2008). Moreover, it is customary to consider dwarf irregular galaxies and dSphs to have a common progenitor (Dolphin et al., 2005) and that the latter have been subject to tidal stripping of gas (Mayer et al., 2001). An early magnetic field can therefore still be present in dSphs and can have an intensity of ≈ 1 μ G if estimated through the star formation rate density relation (Chyży et al., 2011). In this case, the radial profile of the magnetic field can be assumed to follow the stellar profile.

In the case of ultra-faint dwarf galaxies (UFDs), another approach can be used: outflows from the Milky Way are proved to bring magnetization outside the galaxy disc up to 7 kpc above the plane (e.g. Carretti et al., 2013), where the magnetic field is ≈ 10 μ G. UFDs, which are within 40 kpc from the center of the Milky Way, can be permeated by this magnetized environment. The intensity of the field B at a distance d from the Galactic center can be estimated as:

$$B = 50 \frac{\text{kpc}}{d} \mu\text{G} \quad (2.19)$$

and, since UFDs have typical sizes of 100 pc, the field can be considered constant over the whole object. This cannot be applied on dSphs because they lie further from the MW than UFDs, such that the intensity from Eq. (2.19) would be negligible.

Another alternative way to estimate the magnetic field is the assumption of equipartition in the synchrotron radiating source. The condition is that the source is at minimum energy which is split between magnetic U_B and cosmic ray energy density U_{CR} as:

$$U_B = \int \frac{B^2}{8\pi} dV = \frac{3}{4} U_{\text{CR}} = \frac{3}{4} (1 + k) U_e. \quad (2.20)$$

The magnetic field intensity B is thus related to the energy density of the emitting relativistic electrons U_e . Assuming a value for the ratio k between protons and electrons, one can derive the local field intensity as

$$B_{\text{eq}} = \left[\frac{3}{4}(1+k) \frac{C_e}{C_B} \right]^{2/7} \left(\frac{L}{V} \right)^{2/7}, \quad (2.21)$$

where L and V are the luminosity and the volume of the source, respectively. C_e and C_B are tabulated coefficients. However, the assumption of equipartition should hold locally in every part of the source and we know, observationally, that this condition of minimum energy does not always hold, in particular in dSphs.

2.2.2 DM radio searches in the Local Group

As for γ -ray observations, satellites in the Milky Way and in M31 are considered optimal targets for the detection of DM annihilation radio signals. The absence of stellar formation and supernovae, and the lack of emitting interstellar medium make dSphs and UDS the objects with the lowest contamination for radio frequencies. When observing targets like the galactic center or galaxy clusters one needs to model the standard radio emission and separate it from a possible radio DM signal. In the case of dSphs, the only contamination is expected from background compact sources, whose subtraction is easier. Moreover, despite their spatial extensions span up to ~ 500 pc, their proximity induces them to subtend a relatively large solid angle, from few to few tens of arcminutes. Thus, the radio profile of the diffuse DM annihilation signal can be properly sampled (see, e.g., [Beck, 2020](#), for a recent review).

The idea of detecting DM annihilation signals in the radio domain was recognized in the early 2000s in the context of multiwavelength campaigns ([Colafrancesco et al., 2006](#)), even for dSphs targets ([Colafrancesco et al., 2007](#)). In the last decade, several observations with different instruments were carried out and we summarize them briefly here,

Single dish observations One of the main distinctions above the observational approaches can be found in the radio telescope nature: the theoretical signal appears on angular scales corresponding to the host galaxy, from few to few tens of arcminutes. A single dish observation is sensitive to emission up to scales θ :

$$\theta \sim \frac{\lambda}{D}, \quad (2.22)$$

where D is the diameter of the antenna. Therefore, with a sufficient sensitivity, a single dish telescope should be able to detect the extended emission. The coarse angular resolution limits, however, the identification and subtraction of background sources which needs to rely on catalogue information.

[Spekkens et al. \(2013\)](#) observed a sample of four dSphs (Draco, Ursa Major II, Coma Berenices, Willman I) with the 100 m diameter Green Bank single dish Telescope¹ (GBT). They achieved a sensitivity of 7 mJy beam^{-1} after subtracting source identified in the NVSS² catalog. Draco and Ursa Major II were dominated by foreground emission, whereas no significant emission was found in Coma and Willman I, yielding a $10^{-25} \text{ cm}^3 \text{ s}^{-1}$ limit for the annihilation cross section at $M_\chi = 100 \text{ GeV}$ ([Natarajan et al., 2013](#)). [Natarajan et al. \(2015\)](#) observed the UDS Segue I with the GBT, with similar results.

¹GBT website: <https://greenbankobservatory.org/science/telescopes/gbt/>

²NRAO VLA Sky Survey: <https://www.cv.nrao.edu/nvss/>

Interferometric observations The properties of interferometric observations, which are discussed in § 3.1, allow to reach higher angular resolutions than single dishes while retaining sensitivity on the angular scales where the DM is expected. In the last decade, even though no detection has been achieved, more and more sensitive observations were performed allowing to place increasingly stringent constraints on the WIMP parameter space. Meanwhile, the exploitation of long baselines in order to resolve discrete sources has been refined and employed to perform precise source subtraction, thus lowering the confusion level and further improving sensitivities.

Early interferometric DM searches were carried out with the Australian Compact Telescope Array³ (ATCA) and were presented in three different papers: Regis et al. (2015a), where they characterize the source subtraction, Regis et al. (2015b), dedicated to maps production and modeling of the theoretical signal, and Regis et al. (2014), where bounds on the WIMP parameters space were presented.

Note that one way to interpret this kind of plot is to assume the “thermal” cross section as the real one for WIMPs: if the obtained upper limit at a given mass is below the “thermal” value, one can rule out the considered mass.

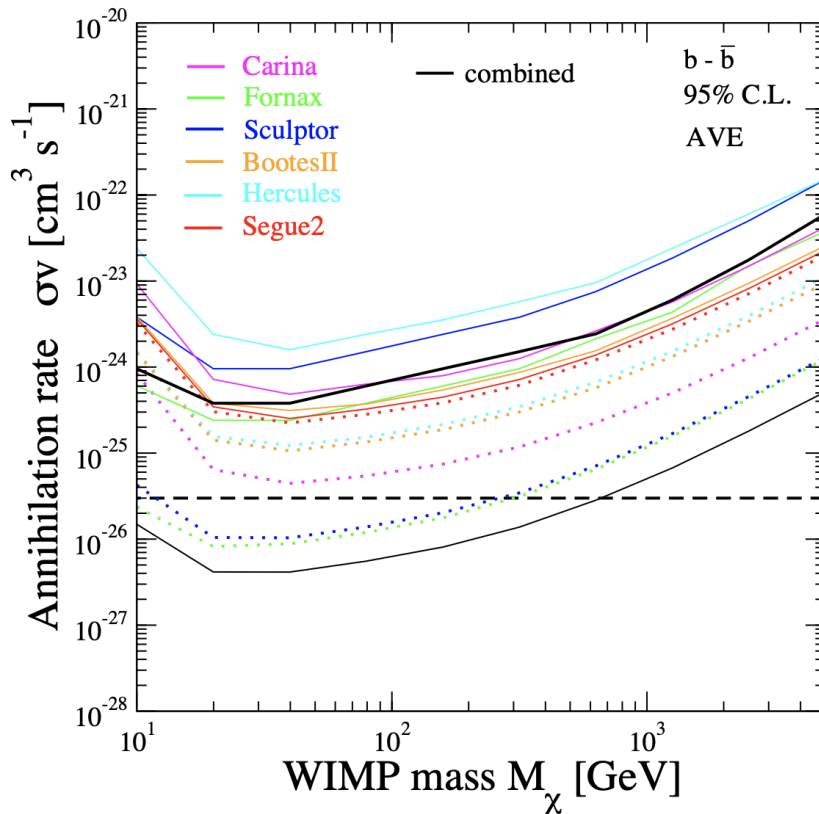


Figure 2.5 Bounds at 95% C.L. on the WIMP parameters space in the AVG (see text for details) scenario for the $b\bar{b}$ annihilation channel. Solid lines are bounds obtained from maps with source subtraction performed in the visibility plane. For dotted lines, the subtraction has been further applied on images. Black lines are obtained through the combination of bounds from single galaxies (Regis et al., 2014, Fig. 4).

Observations targeted three classical dSphs (Carina, Fornax, Sculptor) and three UDS (BootesII, Segue2, Hercules), respectively with 1° and 0.5° mosaics around every dwarf. As the name suggests, the instrument consists in a compact array of 5 ($D = 22$ m) antennas but a sixth one is placed 4.5 km from the core, allowing to obtain high angular resolution. The

³ATCA website: <https://www.narrabri.atnf.csiro.au/observing/>

large bandwidth (2 GHz around $\nu = 2.1$ GHz) and long integration times (up to 17 hours per target) allowed to reach sensitivities of $\sim 30 \mu\text{Jy beam}^{-1}$. For the interpretation of maps, three model scenarios have been considered:

- **OPT:** the optimistic scenario considers the loss-at-injection case for diffusion. This leads to a prominent cusp in the theoretical emission profile and thus to very stringent constraints in the case on non detection. For the magnetic field, equipartition is assumed;
- **PES:** the pessimistic scenario takes the magnetic field strength as inferred from the late SF history of targets and uses a diffusion coefficient $D = 10^{30} (E/\text{GeV})^{0.3} e^{(r/r_*)}$ $\text{cm}^2 \text{s}^{-1}$, where r_* is the stellar half-light radius. This coefficient is really high and brings this scenario near to the “free escape” one, making it an extreme reference case, as the authors claim.
- **AVG:** here, the magnetic field is inferred from the whole SF history. The diffusion coefficient has the same profile as in the PES case, but with a lower normalization ($D_0 = 10^{28} \text{cm}^2 \text{s}^{-1}$). This was taken as the standard, fiducial scenario. Results from this model are shown in Figure 2.5, where upper limits were compared with those from [Spekkens et al. \(2013\)](#). The analysis that combined all the targets yielded to the most stringent constraints on the cross section.

[Regis et al. \(2017\)](#) search for radio signatures from DM in UDS RetII. Observations were taken again with the ATCA telescope in the 1.1 – 3.1 GHz band for a total integration time of 30 h, with the hybrid configuration H75 and using the sixth antenna for high resolution maps. They reached a sensitivity of $10 \mu\text{Jy beam}^{-1}$.

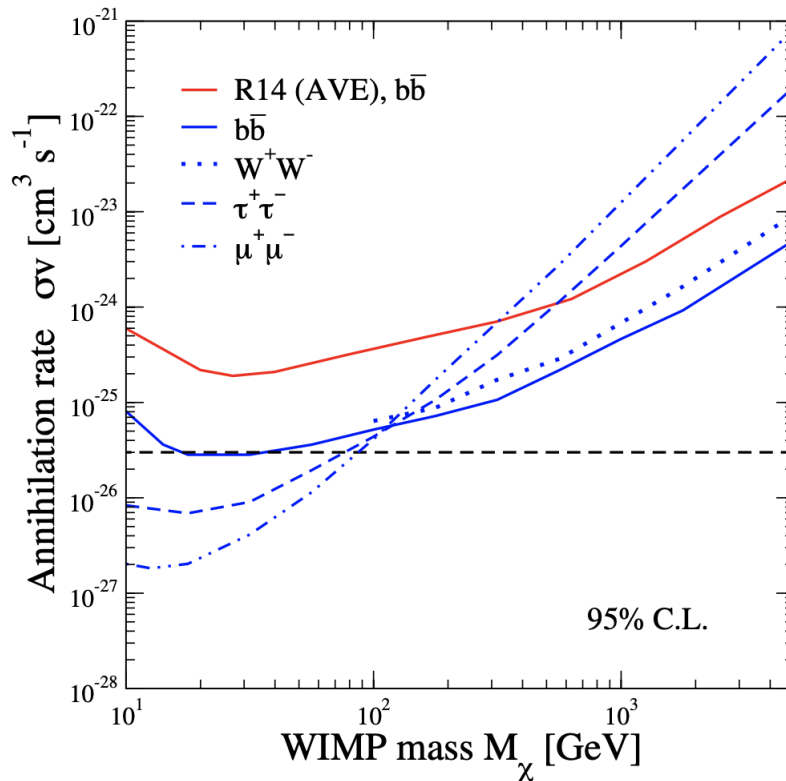


Figure 2.6 Bounds at 95% C.L. on the WIMPs parameters space for different annihilation channels (blue lines). For comparison, the red line is the $b\bar{b}$ bound in the AVG scenario from [Regis et al. \(2014\)](#) (black solid line of Figure 2.5). The plot is taken from [Regis et al. \(2017\)](#), Fig. 13.

They adopted the AVG model and obtained tighter constraints than Regis et al. (2014) and even better than high energy observations (Figure 2.6). Moreover, they found radio counterparts for two BL-Lac which were considered as possible DM annihilation signal in Fermi-LAT data (Geringer-Sameth et al., 2015c), demonstrating they actually are background sources.

DM searches below ~ 1 GHz were missing in the literature until 2019, when Kar et al. (2019) presented a study on 14 dSphs (Table 1 of the Paper) in the frequency range 170 – 231 MHz. Data were taken from the Murchinson Widefield Array⁴ (MWA) GLEAM survey (Hurley-Walker et al., 2016), thus were not dedicated observations. The MWA very different from ATCA: it consists in 8128 dipole antennas organized in 128 "tiles" with maximum baselines of 3 km. This configuration yields a high surface brightness sensitivity and the possibility of observing very large fields, albeit with a coarse $\sim 8'$ angular resolution. In order to perform a proper source subtraction, the authors took high resolution images from the TGSS ADR1 survey (Intema et al., 2017). This survey, taken at 150 MHz, has a resolution of ~ 6 arcseconds, allowing to subtract discrete sources. The subtracted maps from all 14 dSphs were stacked in order to reduce the noise, reaching a sensitivity of 9 mJy beam^{-1} . This result did not yield a detection or an improvement over existing upper limits, but was a first pilot study at low radio frequencies.

A similar study was published by Cook et al. (2020), where they used GLEAM data for 33 dSphs again yielding no detection. Other two recent studies at low frequencies can be found in Vollmann et al. (2020) and Basu et al. (2021). The latter uses the stacking technique with images of 23 dSphs from the TGSS survey (~ 150 MHz). The first is instead a dedicated observation of Canes Venatici I with the Low-Frequency ARray⁵ (LOFAR), again at ~ 150 MHz. In both cases, the non-detection led to put constraints on the parameters space comparable with Fermi-LAT data, but the authors stress how these bounds are very sensible to the model's parameters.

The state of the art in the field has recently been published in Regis et al. (2021). Unlike previous studies, this was conducted on the Large Magellanic Cloud (LMC), which are considered as an intermediate class between dwarf spirals and irregulars. The LMC has the largest \mathcal{J} -factor, after the Galactic center, of the Local Group and the second closest object of the Milky Way and was already the target of early searches (Tasitsiomi et al., 2004; Siffert et al., 2010). Regis et al. (2021) took observations from the Evolutionary Map of the Universe, or EMU (Norris et al., 2011), a wide field, low frequency band survey performed with the Australian Square Kilometer Array Pathfinder⁶ (ASKAP). With a largest detectable scale of $\sim 2^\circ$ at 888 MHz and a $13''$ angular resolution, they reached a sensitivity of $\sim 58 \mu\text{Jy beam}^{-1}$. The data analysis is somehow more elaborated with respect to dSphs, due to the presence of non negligible radio emission; on the other hand, the presence of ionized gas allows a fairly precise estimate of the magnetic field ($4.3 \mu\text{G}$) and the diffusion coefficient ($D = 2 \cdot 10^{28} \text{ cm}^2/\text{s}$). This significantly reduces the modeling uncertainties, allowing to set the most stringent upper limits on the DM particle Figure 2.7.

Canonical WIMP masses up to 480 GeV are ruled out for a $b\bar{b}$ annihilation channel.

⁴MWA website: <https://www.mwatelescope.org>

⁵LOFAR website: <https://www.astron.nl/telescopes/lofar/>

⁶ASKAP website: <https://www.atnf.csiro.au/projects/askap/index.html>

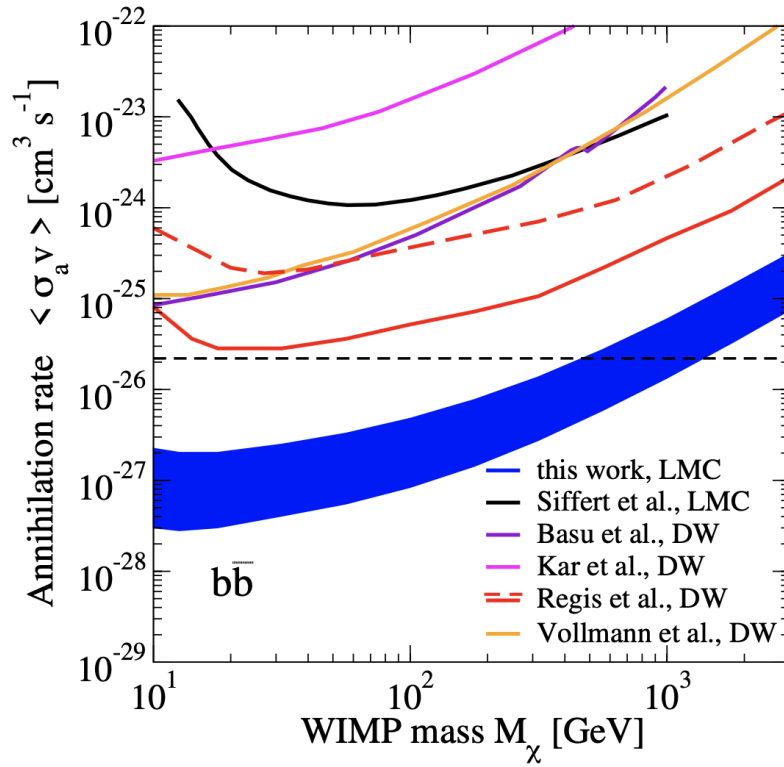


Figure 2.7 Bounds at 95% C.L. on the WIMPs parameters space for annihilation into $b\bar{b}$ (Regis et al., 2021). The uncertainty band is determined by the weakest/strongest bound among those obtained with four different DM profiles.

Chapter 3

Data analysis and reduction

In this chapter we describe methods and procedures we used in the data analysis and reduction. This part represents by far, in terms of time and efforts, the majority of the practical thesis work. The large amount of data available has been processed with CASA¹ (Common Astronomy Software Application). The chapter is organised as follows: in § 3.1 we present basics concepts of interferometry used in the data analysis, which is described in § 3.3, dedicated to the calibration process, and § 3.4, where the reduction of Draco observations is described. § 3.2 introduces details of the target and the instrument used, together with the observational overview.

3.1 Interferometry overview

The use of interferometry in radio astronomy has allowed to largely extend the potentiality of radio observations, not only for the great enhancement in angular resolution but for the growth in collecting area, thus in sensitivity too. This section is necessary to introduce some basic concepts we will use in the data analysis and reduction. For the following paragraphs, a reference can be found in classical textbooks as [Condon and Ransom \(2016\)](#) or [Thompson et al., 1991](#).

Effective area and Antenna temperature. The total spectral power P_ν received by an ideal antenna is given by the geometric area of the antenna A and the receiving flux density S_ν :

$$P_\nu = \frac{1}{2}AS_\nu. \quad (3.1)$$

The $1/2$ factor is due to the fact that antenna receivers are sensitive to a single polarization and thus the power of an unpolarized incoming signal is always split in two. However, real antennas do not convert all the flux density received into output power thus is convenient to define an effective area as:

$$A_e \equiv \frac{2P_\nu}{S_\nu}. \quad (3.2)$$

The most relevant concept here is that the output power can be expressed in terms of an effective temperature by dividing for the Boltzmann constant:

$$T_A \equiv \frac{P_\nu}{k_b}, \quad (3.3)$$

where T_A is the antenna temperature. The advantage of using this quantity is that it can be easily compared with receiver noise, which is naturally measured in Kelvin units.

¹The software is free and available at <https://casa.nrao.edu>

Noise and sensitivity. Radiotelescope receivers are affected by several noise contributions. Noise can be measured by a radiometer, a radio receiver which translates all the power within a certain frequency interval $\Delta\nu$ into an output voltage, or a total noise equivalent temperature T_N . If a radiometer is attached to the output of a radio telescope, it measures every contribute of the antenna noise plus its own. Any source of noise gives a contribute almost indistinguishable from that of another source and they generally form altogether a Gaussian like distribution with zero mean. The relevant noise property is therefore its variance σ_s which, in case of interferometric observations, can be expressed as:

$$\sigma_s = \frac{2k_b T_s}{A\sqrt{N(N-1)/2}\sqrt{\Delta\nu\tau}}, \quad (3.4)$$

where A is the collecting area of a single antenna, $N(N-1)/2$ are the number of visibilities measured by an array with N antennas and τ is the observing time.

Complex visibilities. The interferometric response to a source of brightness distribution $I_{\hat{s}}(l, m)$, where (l, m) represents the sky plane coordinates and \hat{s} is the pointing direction, is a complex visibility \mathcal{V} :

$$\mathcal{V} \equiv R_c - iR_s = A e^{-i\phi}, \quad (3.5)$$

where R_c and R_s are, respectively, the even cosine component and the odd sine component of the visibility. The complex visibility \mathcal{V} can be related to the sky brightness distribution I by the Van Citter-Zernike theorem:

$$\mathcal{V}(u, v) = \iint I(l, m) e^{-2\pi i(ul+vm)} dl dm, \quad (3.6)$$

where (u, v) are the coordinates corresponding to the array layout and (l, m) the sky plane coordinates (see Figure 3.2 for a representation of the coordinates for imaging). We note that equation 3.6 is a two dimensional Fourier transform relationship. Every baseline of an interferometer measures a point in the uv -plane for each exposure time and multiple points across the uv -plane are measured when the Earth rotates during an observation and the projected baseline changes with time. Additionally, an interferometer with N antennas, instantaneously measures $N(N-1)/2$ baselines.

Angular scales. There are few scales which characterize an observations and are determined by the instrument. The field of view (FoV) Θ_{FoV} is the sky area that the primary beam is sensitive to and is defined as the corresponding angle size:

$$\Theta_{\text{FoV}} \sim \frac{\lambda_c}{D}, \quad (3.7)$$

where λ_c is the central wavelength of the observation and D is the antenna diameter, given that every antenna has the same size. A second, important quantity is the angular resolution θ_{min} , which corresponds to the minimum detectable separation between two sources and is set by the longest baseline b_{max} :

$$\theta_{\text{min}} \sim \frac{\lambda_c}{b_{\text{max}}}. \quad (3.8)$$

Conversely, the maximum angular size θ_{max} of a detectable signal is:

$$\theta_{\text{max}} \sim \frac{\lambda_c}{b_{\text{min}}}, \quad (3.9)$$

which means that an interferometer will not be sensitive to structures more extended than θ_{max} .

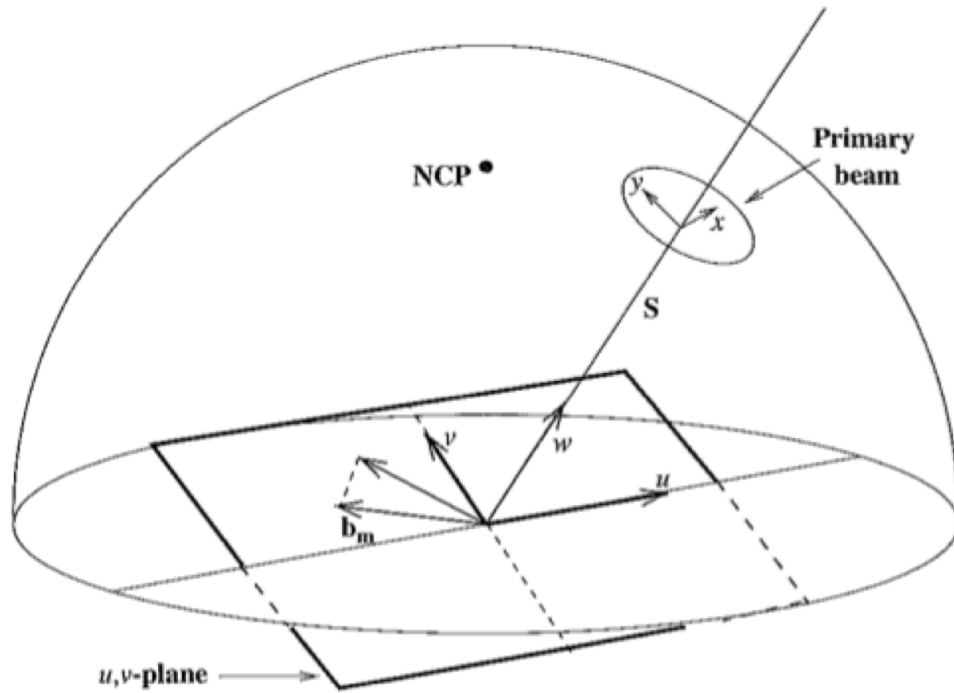


Figure 3.1 Representation of the coordinate systems used in interferometric observations: the sky plane (here shown as (x, y)) and the visibility plane (u, v) . “NCP” stands for North Celestial Pole. The w axes is in the same direction as the pointing direction S .

Flagging and calibration. Radio observations are always subject to errors, interferences and corruptions of various type that need to be corrected for. Such correction process is called calibration and assumes that corruptions can be described by 2×2 antenna-based, complex gain matrices G that are the solution of the following equation:

$$\mathcal{V}_{\text{obs}}^{ij}(\nu, t) = G^i(\nu, t) G^{*j}(\nu, t) \mathcal{V}_{\text{true}}^{ij}(\nu, t), \quad (3.10)$$

where (i, j) are antenna indexes and $\mathcal{V}_{\text{true}}$ are the visibilities that best describe the intrinsic sky brightness (“sky model”). The matrix G^{ij} is to be solved in the calibration process. The gain matrix is often factorized as:

$$G^i(\nu, t) = B^i(\nu) J^i(t), \quad (3.11)$$

where B is the frequency dependent factor, also called bandpass, and J incorporates the time variability of the gains. Gains can be determined through the observation of a calibrator source for which we already have an accurate model. These sources are generally bright, unresolved, unpolarized and not variable. The bandpass is generally considered stable through an observations, therefore a bandpass (or “primary”) calibrator is normally observed only once at the beginning of the observation. The observation of a bandpass calibrator often also sets the flux density scale.

Time variability in the gains J is often due to atmospheric variations that corrupt visibility phases. A “secondary” calibrator not far from the observed target is normally observed, interspersed throughout the duration of the observation, in order to calibrate out phase corruptions. A reference antenna, i.e. a well behaved antenna in the array for which the phase is set to zero, is often used in calibration.

Visibilities are often corrupted by interfering signals that cannot be calibrated out, i.e. are not antenna-based variations of the receiving system. These corruptions are, most of the times,

man-made (e.g., cell phones, satellites) and the corrupted visibilities need to be discarded or, in the radio interferometry language, flagged. Flagging methods are described further in the data reduction section.

Imaging After visibilities are calibrated, an image can be formed by inverting the Fourier relationship in (3.6). As mentioned earlier, visibilities are only measured at a certain number of uv points and this can be expressed as:

$$\mathcal{V}_{cal}(u, v) = S(u, v) \mathcal{V}_{true}(u, v), \quad (3.12)$$

where $S(u, v)$ is the sampling function, which, in its simplest form, is one for each point measured and zero elsewhere. The Fourier transform of the sampling function is called dirty beam $B_D(l, m)$ and represents the angular resolution of the observation, namely the point spread function (PSF). If we now use the convolution theorem we find the dirty image $I_D(l, m)$ to be:

$$I_D(l, m) = \iint \mathcal{V}_{cal}(u, v) e^{2\pi i(ul+vm)} du dv = B_D(l, m) \otimes I(l, m), \quad (3.13)$$

which indicates that the reconstructed (dirty) image is the convolution (\otimes) between the intrinsic sky distribution and the dirty beam. In this sense it is called “dirty image”: as the uv plane is never fully sampled, the Fourier transform of an incomplete sampling turns into a dirty beam with significant sidelobes and the corresponding dirty image requires deconvolution techniques in order to achieve a better reconstruction of the sky brightness distribution.

Deconvolution or CLEAN is implemented in different algorithms (e.g., Högbom, 1974; Clark, 1980), which follow a similar procedure: they are iterative methods and, at each iteration, the flux density peak of the dirty image is found and its position is reported in a model map, together with the peak value. Simultaneously, a fraction of the dirty beam is removed from the dirty image, which now becomes a residual image, in correspondence of the peak position. The process is repeated until a stopping criterium is reached. The model map so formed is then convolved with a two dimensional Gaussian function that is the best fit to the main lobe of the dirty beam. The residual map is added to obtain a restored (or final) image.

3.2 Giant Metrewave observations of the Draco dwarf galaxy

The Draco Dwarf Spheroidal galaxy (RA = 17^h20^m12.40^s, DEC = +57°54^m55.00^s) is located 76 kpc away from the Solar system and has a $M_V = -8.6$ absolute magnitude (McConnachie, 2012). It was discovered by Wilson (1955) during the Palomar Observatory Sky Survey (POSS), together with the LeoI, LeoII and Ursa Minor galaxies. Similar to other dwarf spheroidal galaxies, Draco has low metallicity, with a $[Fe/H] = -1.74$ mean value (Faria et al., 2006), indicative of no active star formation. In fact, the reconstructed star formation history shows that most stars are older than 10 Gyr and the last formation phase ended ~ 2 Gyr ago (Aparicio et al., 2001). Moreover, no evidence of either cold or hot interstellar medium has been detected, such that the only two relevant components of the galaxy are stars and its DM halo (Putman et al., 2021).

Mashchenko et al. (2006) used these two components to model global properties of Draco: studying the velocity dispersion of stars through their radial motion and simulating the halo evolution, they ruled out the hypothesis of Draco being tidally disrupted by the MW. They showed that both a NFW profile and a Burkert one could, with different constraints, fit the observed data. Estimates of \mathcal{J} (and \mathcal{D}) factors for dSphs are not straightforward due small amount of stellar kinematic data. Moreover, results can be slightly different for various models and parameters choices (see, e.g., Chiappo et al., 2019). Draco has been, however, recognized as one of the dSphs with the highest \mathcal{J} factor (Bonnivard et al., 2015), with

$\log_{10}(\mathcal{J}/[\text{GeV}^2 \text{ cm}^{-5}]) = 18.9$ for most choices of solid angle values (see Horigome et al., 2020, for a recent analysis).

In this thesis we analyze Draco observations taken with the Giant Metrewave Radio Telescope (GMRT)². The GMRT is a versatile radio interferometer located about 80 km north of the Indian city of Pune, in a region of relative low contamination from radio frequency interference. It consists of 30 antennas of 45 m diameter each, equipped with feeds that cover six frequency bands centered at 50, 153, 233, 325, 610 and 1420 MHz respectively. The interferometer configuration consists of a central compact array of fourteen antennas, randomly distributed over an area of one square kilometer, allowing high brightness sensitivity. The other sixteen antennas form a roughly Y-shaped figure which extends up to the maximum baseline of 22.7 km to provide high angular resolution. The array has been recently subject to a technical upgrade (uGMRT) which increased the sensitivity of about three times (Gupta et al., 2017).

Our observations of the Draco dwarf galaxy were taken on September 22, 2019, for about 4 hours from 7:37:21 to 11:31:10 (UTC). The main observational parameters have been summarized in Table 3.1. The time requested was decided after consulting the exposure time calculator of the GMRT³, asking for an expected sensitivity of $10 \mu\text{Jy beam}^{-1}$ in Band 4. Observations are organized into 13 scans: the first and the last are dedicated to the bandpass calibrator 3C286 (§ 3.3.1), while the 5 on-source scans (§ 3.4) are located between 6 gain calibrator scans (§ 3.3.2).

Target	RA	DEC	Band	N° channels	$\Delta\nu_{\text{ch}}$	τ_{int}
Draco	17 ^h 20 ^m 12.4 ^s	+57°54′55.0″	550 – 750 MHz	2048	97 kHz	16 s

Table 3.1 Parameters for our observations: target name, coordinates, band and number of channels. The channel width $\Delta\nu_{\text{ch}}$, representing the spectral resolution, and τ_{int} is the integration time for each visibility.

At these frequencies the GMRT has a FoV of 0.60 square degrees and can detect signals on scales as large as 19′. Eight antennas were malfunctioning throughout the observation and were permanently flagged⁴, resulting in the uv -coverage shown in Figure 3.2. Four of these compose the northern arm of the Y-shaped array.

3.3 Calibrators

The detection of the DM-induced radio emission requires a meticulous calibration in order to obtain the best possible sensitivity and this attention needs to be applied to calibrator data too. Due to the particular importance for this experiment, in this section we are describing the flagging and calibration process of both calibrators in details.

3.3.1 Primary calibrator

The primary (or bandpass) calibrator in our observations is 3C286, a brilliant quasar at $z = 0.8493$ (Albareti et al., 2015) in the constellation of Canes Venatici. It is largely used as calibrator for radio interferometric observations (Perley and Butler, 2017) and is included in flux density models available in CASA. This has a flux density of 21.8 Jy at the central frequency 0.60 GHz, with a spectral index $\alpha = 0.42$. Observations were carried out in two different scans, at the beginning and at the end of observations for a total exposition time of 25 minutes.

²See <https://www.gmrt.ncra.tifr.res.in/index.html> for the GMRT website.

³GMRT Exposure Time Calculator: <http://www.ncra.tifr.res.in:8081/~seccr-ops/etc/etc.html>

⁴Those were antennas 1,7,13,23,27,28,29 and 30.

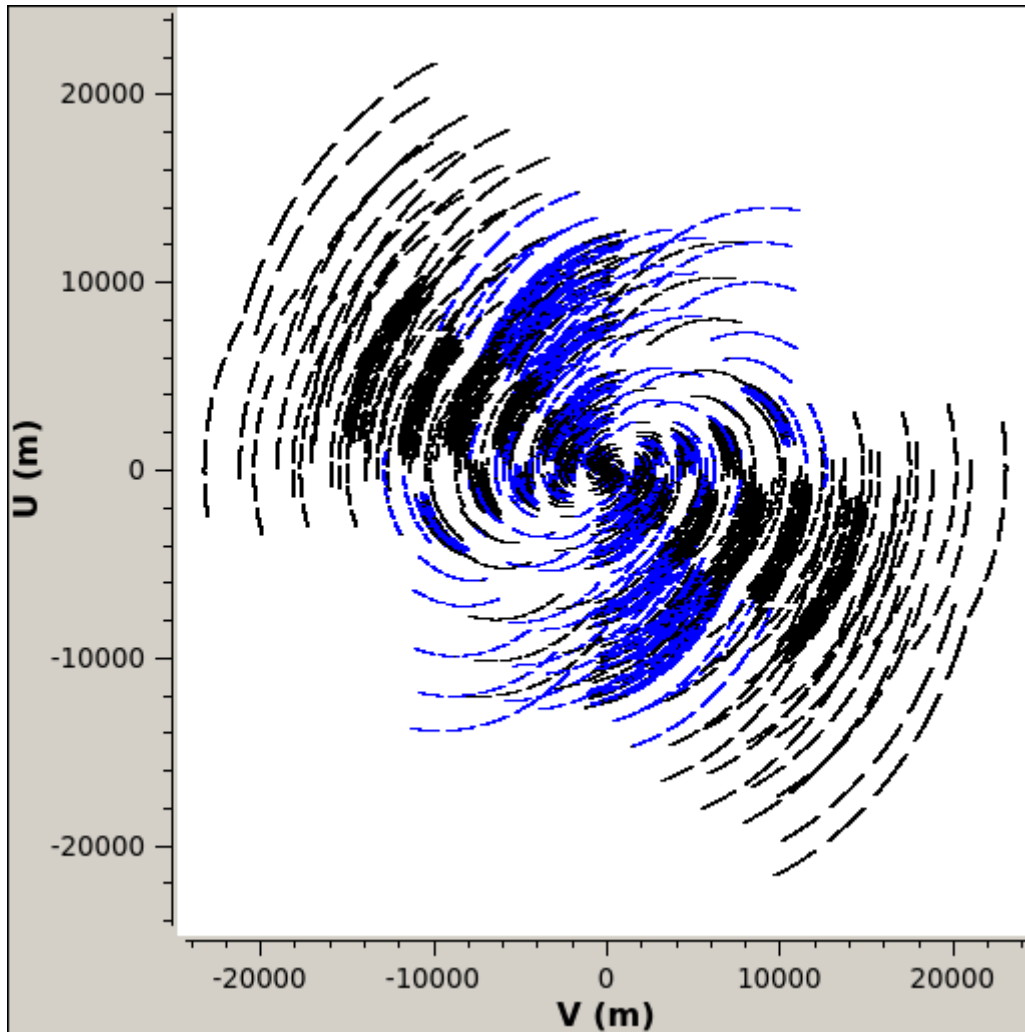


Figure 3.2 Coverage of the uv -plane from the Draco observation. Blue points are unflagged, black points are flagged.

The first step of the data reduction is a first manual flagging to remove most evident Radio Frequency Interferences (RFI) together with autocorrelations and time slots at low elevation when antennas may have shadowed each other. Then, the flux density model mentioned above has been assumed and a preliminary bandpass solution was computed. After the bandpass was applied, we manually flagged further RFI in the calibrated visibilities and performed an automatic flagging through the RFlag algorithm⁵. The algorithm removes outlier visibility points calculated on the statistics of sliding time and frequency windows. In this case it has been applied on residuals, that is on differences between bandpass corrected and model data. After each round of flagging a bandpass was recomputed and applied and, after four iterations, the process converged.

Figure 3.3 shows the residual visibility spectrum, i.e. the difference between the calibrated and model visibilities. In the case of perfect calibration, residuals will only contain noise, expected to be equally distributed around zero. We can see that the scatter is small, slightly worse for the imaginary part compared to the real one, with a larger scatter below 600 MHz.

⁵CASA documentation on the RFlag algorithm: <https://casa.nrao.edu/Release4.1.0/doc/UserMan/UserMansu164.html>

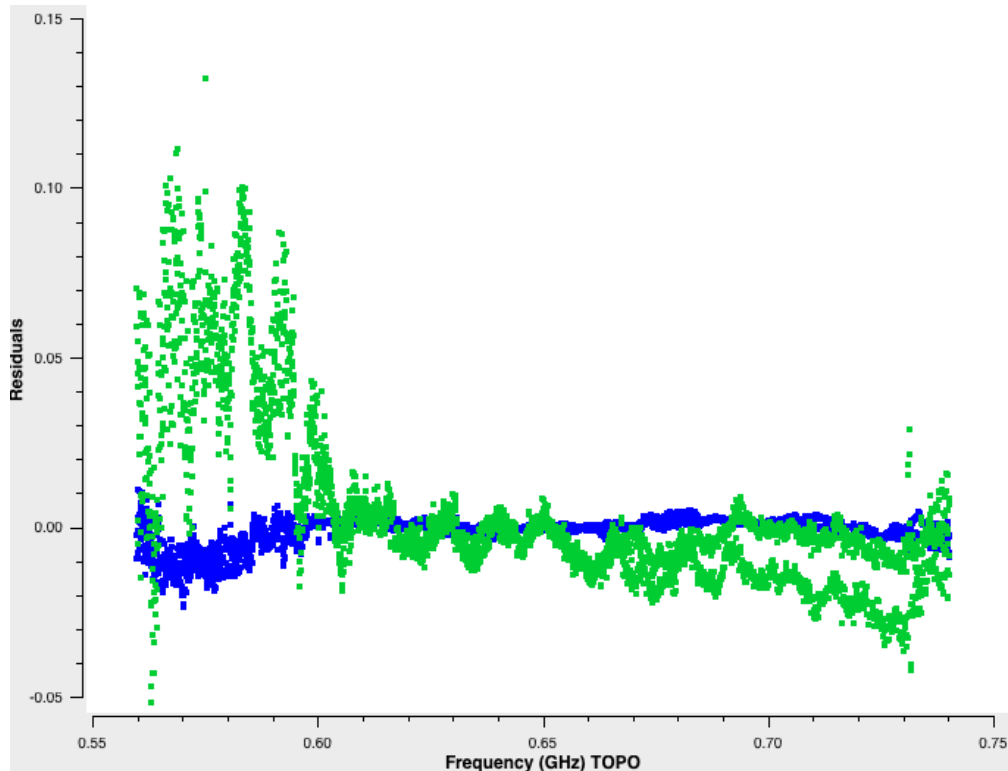


Figure 3.3 Residual (i.e. data minus model) visibility spectra for the primary calibrator 3C286. The real (imaginary) part of the visibility is plotted in blue (green). Data are averaged over time and baselines. Points for both correlations RR and LL are shown.

3.3.2 Secondary calibrator

The BL LAc 1738+476 (Véron-Cetty and Véron, 2006) was observed as a secondary (phase) calibrator. Since a phase calibrator has to produce gain solutions in function of time $J^i(t)$, it was observed for approximately 5 minutes every 40 minutes.

The flagging process for 1738+476 is similar to the one of the first calibrator: a preliminary manual flag is performed and bandpass solutions are applied before running the RFlag algorithm. CASA does not store any model for this source, therefore we derived a source model from the observations themselves. We first used a flat spectrum source with 1 Jy flux density as a source model in order to solve for phase variation with time, with solution intervals of 2 minutes. Then we made a dirty image where we synthesized the whole band using the multi-frequency algorithm and measured the flux density of the calibrator to be $S = 0.63$ Jy at the central frequency of $\nu_c = 650$ MHz. As the source spectral index α is not reported in the literature, we derived it by combining this measurement and its flux density $S = 1.62$ Jy at 365 MHz (Douglas et al., 1996):

$$\alpha = -\frac{\log S_{\nu_1} - \log S_{\nu_2}}{\log \nu_1 - \log \nu_2} \sim 0.6. \quad (3.14)$$

We used this spectral value to set a model of the secondary calibrator as a function of frequency through the CASA task *componentlist*. We used this model to solve for gain amplitude variation as a function of time - after applying the phase solutions - with solution intervals of 2 minutes. As the source is not bright enough to warrant sufficient signal to noise ratio per individual frequency channel, we averaged 100 channels (i.e., 10 MHz) together in order to solve for gain amplitudes.

For each iteration of phase and amplitude solutions we performed a round of flagging to excise outlier data points, similarly to what was done for the primary calibrator. The process converged after a few iterations. Figure 3.4 shows that both the real and imaginary part of

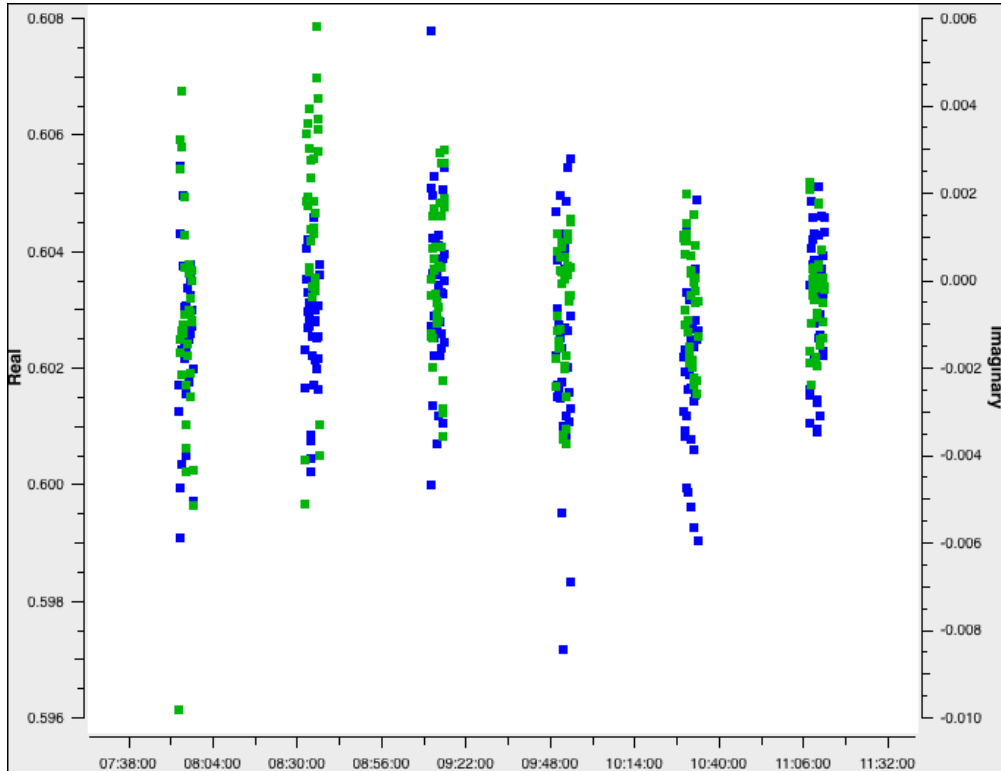


Figure 3.4 Residual (i.e. data minus model) visibilities as a function of time for the secondary calibrator 3C286. The real (imaginary) part of the visibility is plotted in blue (green). Data are averaged over the whole bandwidth and baselines.

the residual visibilities are distributed around zero with a small scatter - as expected. The rms scatter is 1.5%, indicating a fairly good calibration.

Figure 3.5 shows the accuracy of the spectral calibration after gain amplitude solutions. Also in this case the scatter is small around the model for all the frequencies. After this last step, calibration solutions are ready to be applied on the target. To summarize, we have three solutions: a bandpass solution from the primary calibrator 3C286, and gain phase and amplitude solution from the secondary as a function of time.

3.4 Draco

Observations of the spheroidal dwarf galaxy Draco were grouped into 5 different scans of 30 minutes, alternated with the secondary calibrator, for a total exposure time of 150 minutes.

Data were flagged following the same procedure used for calibrators and calibration solutions were applied to form calibrated visibilities. Visibilities were then Fourier transformed into a dirty image using the CASA *clean* task. We ran a preliminary deconvolution with 1000 major cycle of the clean algorithm, using a threshold of 1 mJy beam^{-1} as a stopping criteria. The map obtained has a FoV of 0.37 square degrees, large enough to enclose the eventual diffused emission as the virial radius of Draco is of $16'$ (Klop et al., 2017). The map is produced with a cell size of $1.2''$ and a synthesized beam size of $4.46''$, obtained with uniform weighting: visibilities are weighted with weights $W(u, v)$ when gridded in the uv -plane:

$$V(u, v) = W(u, v) V'(u, v) \quad (3.15)$$

where uniform weightings W_{uni} are:

$$W_{\text{uni}}(u, v) = \frac{1}{\delta_s(u, v)} \quad (3.16)$$

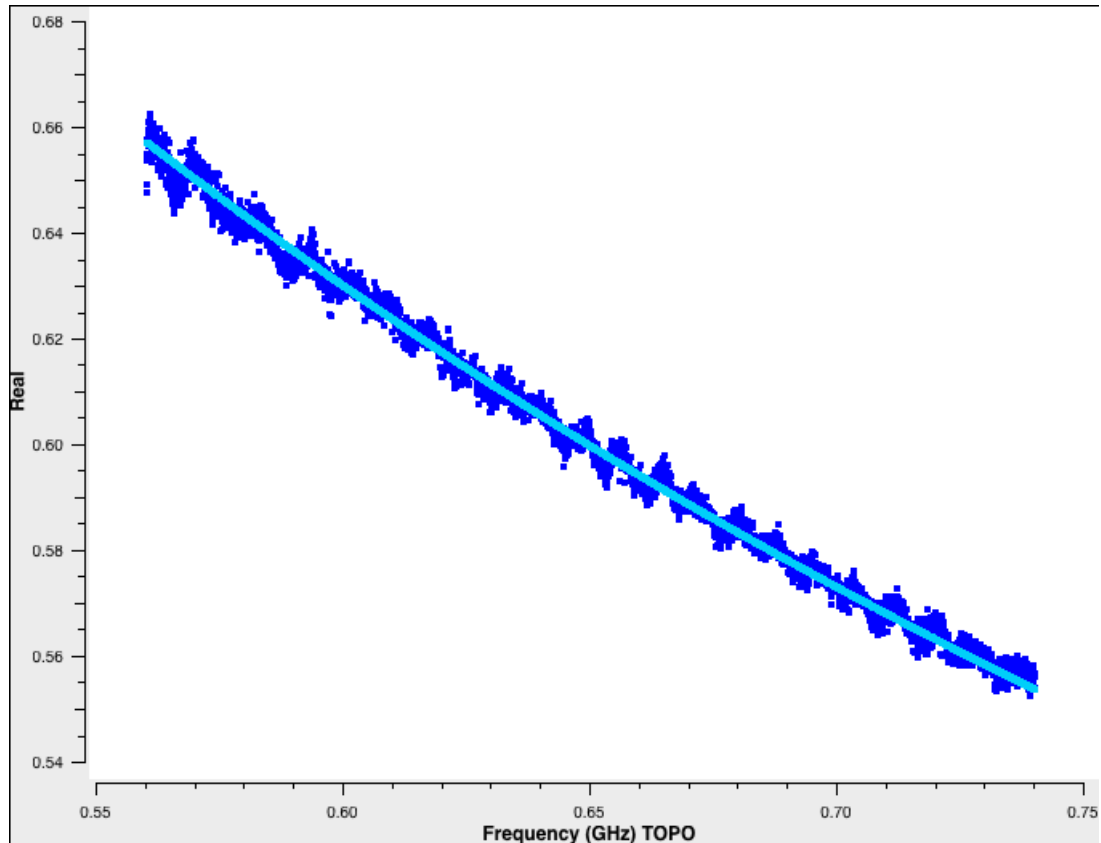


Figure 3.5 Real part of visibilities (dark) and model (light blue) as function of frequency. Spectral points are averaged over time and baselines.

are inversely proportional to the sampling density function δ_s , resulting in a higher resolution and sidelobes suppression, but increasing the noise level. The natural option is the opposite as it uses the number of baselines that N that fall within the specific uv pixel: the noise variance of a visibility

$$W_{\text{nat}}(u, v) = \frac{1}{N} \quad (3.17)$$

Natural weights lead to a larger synthesized beam and higher sidelobes. Another possibility is to use the Briggs et al. (1999) weighting, which varies between uniform and natural schemes relying on the local density of uv points and the *robustness* (r) parameter. This can continuously vary between -2 , which is close to a uniform scheme, and $+2$, which is close to the natural one.

For the successive deconvolutions, we tried with different schemes and then decided to use the Briggs scheme with $r = -1$. This setup was the better compromise between resolution and sensitivity, resulting in a synthesized beam of the image is $4.60''$ and the measured rms is $40 \mu\text{Jy beam}^{-1}$. The radio image is shown in Figure 3.6 overlaid on the optical map. In order to express the sensitivity in term of surface brightness, we calculate the synthesized beam solid angle Ω_b as:

$$\Omega_b = \frac{\pi\theta_b^2}{4 \ln 2}, \quad (3.18)$$

where θ_b is the synthesized beam size, leading to a $6 \mu\text{Jy arcmin}^{-2}$ surface brightness sensitivity. This quantity can be fairly compared among different images and beam sizes, as we do in the next paragraphs.

The sensitivity of our final images remains somewhat limited by calibration errors around bright sources. Figure 3.7 shows a zoom into the brightest source in the field, just north-west off Figure 3.6. The source has a peak flux density of $\sim 180 \text{ mJy beam}^{-1}$ and its residual

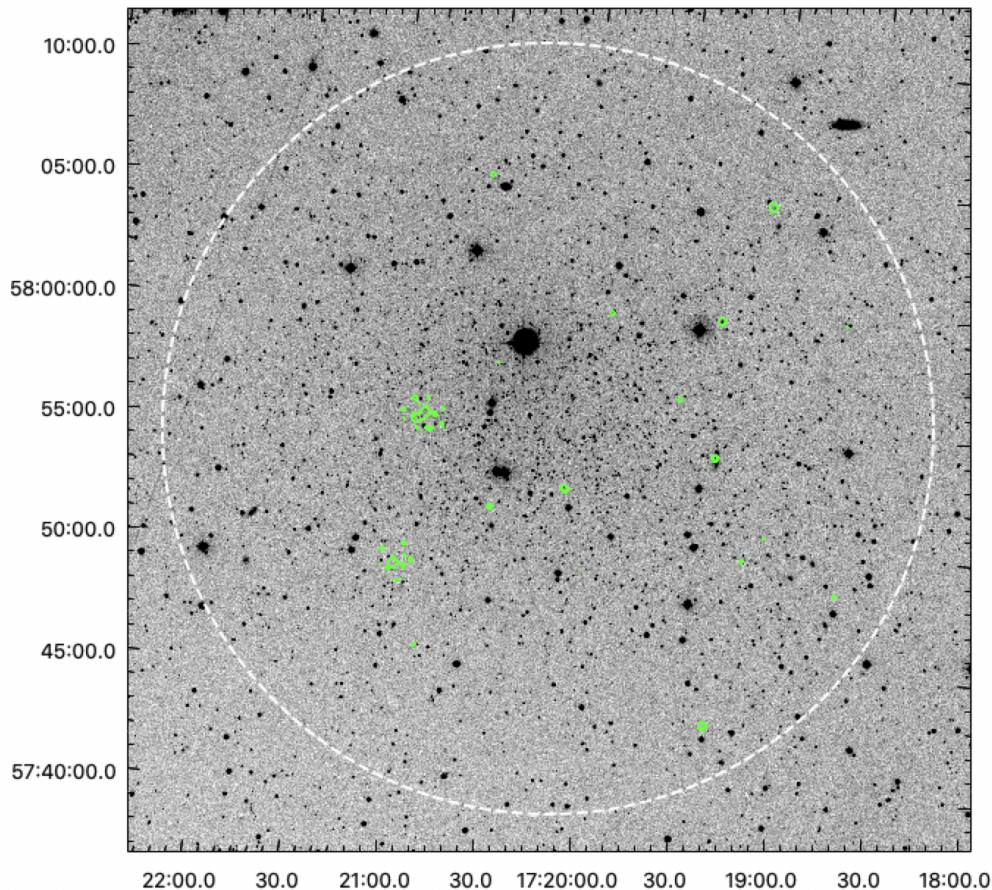


Figure 3.6 Draco optical image ($35' \times 35'$) from the DSS survey. White dashed circle: projected virial radius ($16'$) taken from Klop et al. (2017). Green: 3σ radio contours of the high resolution map. The synthesized beam is $4.60''$ and the rms noise is $40 \mu\text{Jy beam}^{-1}$.

sidelobes cannot be subtracted through deconvolution. In order to improve the noise, we attempted selfcalibration: we derived a sky model from the clean image and use it to calculate phase solutions with a 2 minute interval. After solutions were applied, the rms noise improved, reaching a $36 \mu\text{Jy beam}^{-1}$, although no further improvement was obtained through other selfcalibration rounds.

Sensitivity estimation. Since a perfect calibration is difficult to be obtained, we are interested in which would be the rms if no calibration errors were made. To do so, we used the Stokes V parameter: the GMRT data we used were taken with the two correlations RR and LL, which correspond to right and left circular polarizations so that the intensity Stokes parameter (I) is obtained as the quadratic sum of the two. The V parameter measures instead the circular polarisation with the semi-difference of RR and LL.

The reason we are interested in such quantity is that celestial sources are not circularly polarised and thus a Stokes V image should only contain noise. Thus, measuring the rms of the Stokes V image gives an estimate not contaminated by calibration errors. Moreover, even though we do not expect to be confusion limited (see § 3.4), the Stokes V rms is not affected by confusion since either. We generated a Stokes V dirty image, with the same weighting scheme of the previous images (Figure 3.8). The image is considerably more featureless compared to the Stokes I image, even if the bright source on the top right corner shows artefacts in Stokes V too, likely due to instrumental polarization. The measured rms of the image thus has been taken far from that source and resulted in a $20 \mu\text{Jy beam}^{-1}$ ($3 \mu\text{Jy arcmin}^{-2}$) rms noise.

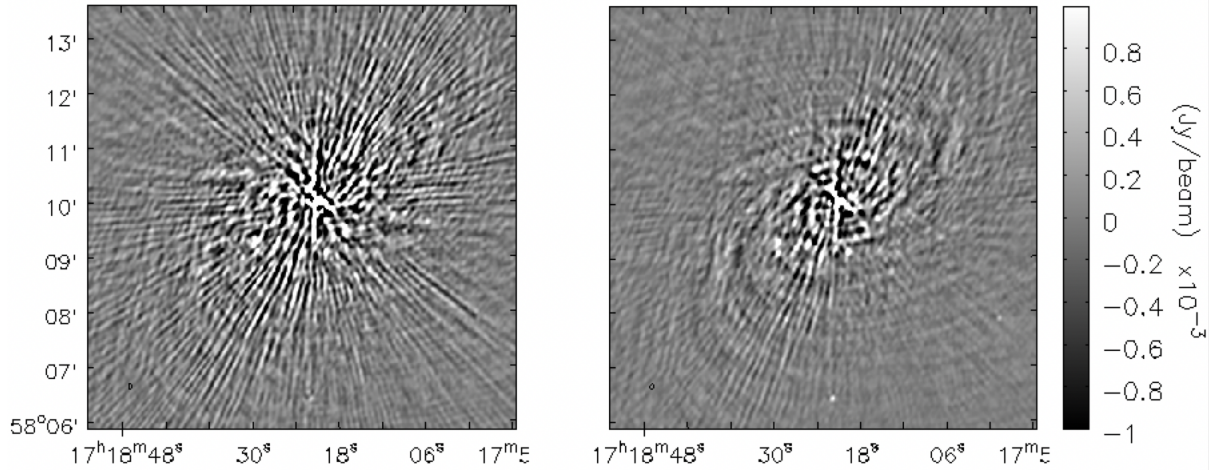


Figure 3.7 Zoomed images on the bright source located just outside the right-top corner of Figure 3.6. The comparison is made on images before (left panel) and after (right panel) self calibration application. It can be seen that the artifacts around the source were mitigated by selfcalibration.

Low resolution maps. We wanted to determine the best way to generate a low resolution, high sensitivity image for Draco, so that an eventual diffuse component due to DM would emerge above the noise. Imaging with natural weightings led to a $\sim 10''$ resolution while we wanted it to be larger than $20''$ in order to have a lower brightness sensitivity. The loss in terms of resolution is not worrying since the theoretical emission is expected on scales above $1'$.

Another way to achieve a coarser resolution is to make a selection on the data based on the baseline length. Longer baselines provide higher resolutions and vice versa, thus selecting baselines shorter a certain length leads to lower resolutions. Throwing away long baselines obviously damages the sensibility since we have fewer antennas involved, but since the rms is measured as a brightness a larger beam size may compensate for the sensitivity loss. To maintain an acceptable rms and get a restoring beam of $20'' - 25''$, we produced images with uniform weighting and excluded baselines longer than 3.0 km. The obtained low resolution intensity map is showed in Figure 3.9, with a noise rms of $205 \mu\text{Jy beam}^{-1}$, corresponding to $1.52 \mu\text{Jy arcmin}^{-2}$. As expected, the higher rms is compensated by the larger beam size and the brightness sensitivity is better than the one of Figure 3.6. This is the same for the Stokes V map (Figure 3.10), for which we achieved an rms noise of $0.38 \mu\text{Jy arcmin}^{-2}$.

We investigated the best trade off between sensitivity and angular resolution by combining different choices of baseline cuts and imaging weights. We generated 20 Stokes V maps, varying the robustness parameter between -1.0 and +2.0 with bins of 1.0 and made five different baseline cuts: at 3 km, 2 km, 1.5 km, 1 km and 0.5 km. The sensitivity as a function of synthesized beam size is plotted in Figure 3.11. We can see that the sensitivity rapidly decreases as a function of baseline cut until the synthesized beam size is $\sim 80''$, after which it does not change much. The behaviour is fairly similar among all the choices of weighting scheme, essentially validating our final decision of keeping the robustness to -1.0. We also kept the baseline cut at 3 km because the decrease in brightness sensitivity came at the cost of evident artifacts in correspondence of the sidelobes residuals of bright sources. If better a better deconvolution of bright sources was achieved, a cut at 1.5 km, thus obtaining a $\sim 1'$ beam size, would have been the best trade off.

Source subtraction. The subtraction of discrete sources is a crucial step in the analysis of these maps for at least two reasons. The first is that the more point-like sources we manage to

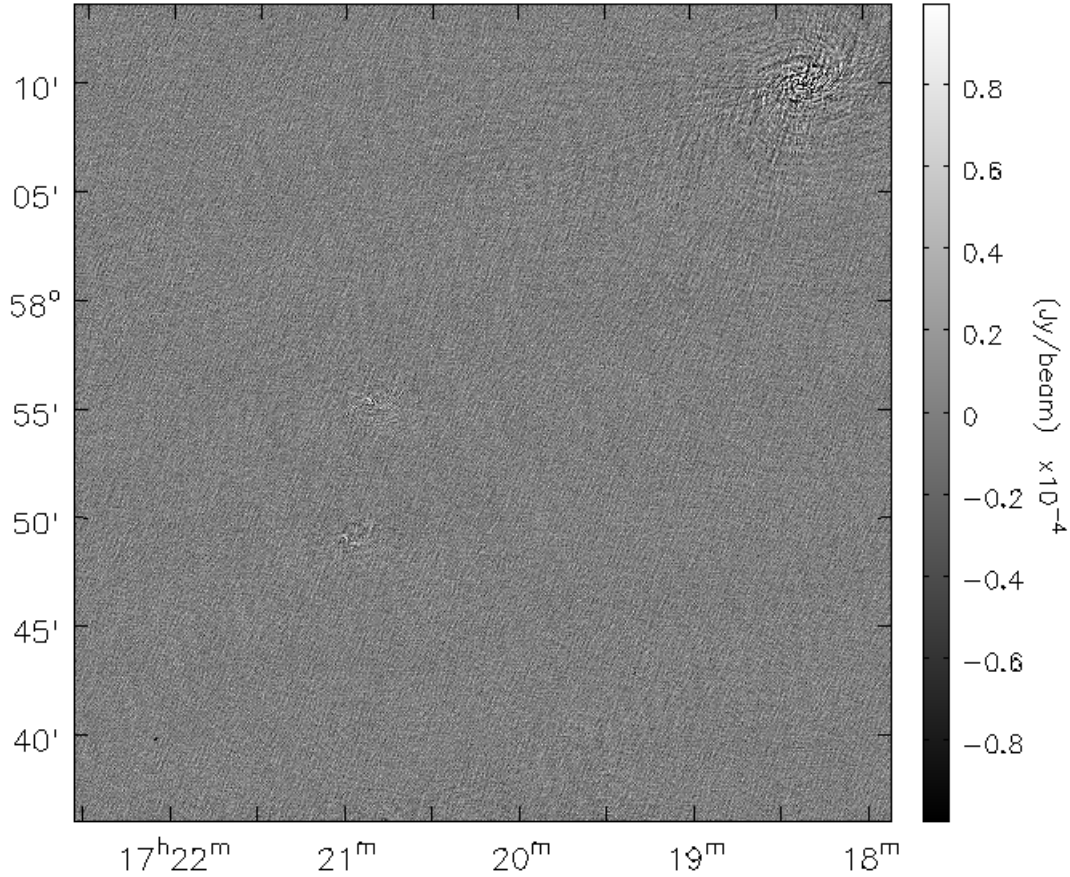


Figure 3.8 Stokes V map of the Draco field. The achieved sensitivity is $20 \mu\text{Jy beam}^{-1}$ for a $4.60''$ synthesized beam, a factor of two better than the Stokes I image.

subtract the less will be the confusion level of our maps, as discussed in the next paragraph. The second is that a discrete source can be interpreted as diffuse emission on a small scale when maps are subject to the statistical analysis described in § 4.2, thus resulting as a detection of potential DM annihilation signal.

In literature, slightly different methods are used. For single dishes or interferometers with large beams, it is necessary to use catalogs of discrete radio sources from surveys (e.g. in Kar et al., 2019). When instead, a set of long baselines are included in the observations, the subtraction is made either in the visibility plane, through uv models of high resolution maps, or directly on the image plane (Regis et al., 2015b). In our case, we disposed of several long baselines, reaching a resolution of $4.60''$. We decided to perform the source subtraction in the visibility plane by using the CASA task *uvsub*, that subtract the model column of a CASA measurement set from the data column. In order to produce a proper model, we performed a deep deconvolution down to a threshold of $110 \mu\text{Jy beam}^{-1}$, namely 3σ over the measured noise of the high resolution map. After the subtraction, we cleaned the resulting visibilities to the same threshold of the model with a cut on baselines longer than 3 km, obtaining the map in Figure 3.12. This is the final product of our data reduction and, as described in Chapter 5, is the subject of the statistical analysis that leads to put bounds on the WIMPs parameters space. The measured rms of this image is $230 \mu\text{Jy beam}^{-1}$ for a beam size of $20.5''$. This is almost five times the rms of the Stokes V map of Figure 3.10. This can be partially due to the contamination of two bright sources: the one on the top right corner we already pointed out and the one which lies just off the field, in the bottom central edge of the map. A confront with the NVSS catalog confirmed that these are the two brightest sources of the field. Moreover, as

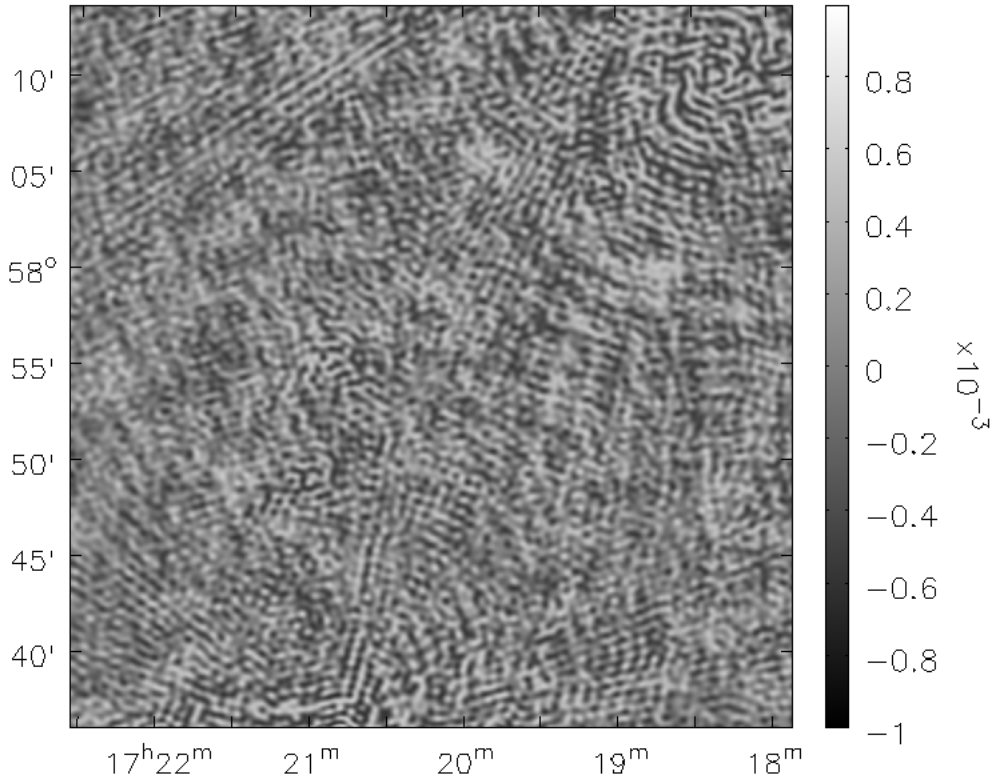


Figure 3.9 Residual image for low resolution map. The sensitivity is $205 \mu\text{Jy beam}^{-1}$ for an original beam size of $20.5''$.

visible in the map, a remnant of the source at the left of the center is still present even after the subtraction on the visibility plane. This can be addressed to the enlargement of the beam and the fact that residuals of the source have been recognized as emission in the deconvolution process. As described in § 4.3.1, this results in a preference for the presence of annihilation signal in the statistical analysis, which has to be considered artificial.

Confusion level. The confusion contribution to the rms of a radio observation is caused by faint, unresolved sources which isotropically populate the sky background. As they cannot be separated in individual sources, their effect is to add to the noise in each individual synthesized beam, therefore increasing the pixel-to-pixel variance. For a given radio telescope, the confusion rms σ_c is proportional to the beam size.

Since the confusion term is the integral contribution of a number of point-like source, by assuming a model for their distribution and their flux density, confusion can be estimated. If the confusion term is higher than the noise rms, the image is termed “confusion dominated”. Conversely, the image is termed “noise dominated”. We intend to determine which regime our observations belong to, as the noise can be reduced by a longer integration, whereas the confusion cannot.

An estimate of the confusion noise $\sigma_{c,\text{XTC}}$ can be obtained by the GMRT Exposure Time Calculator, which uses the empiric formula:

$$\sigma_{c,\text{XTC}} \simeq 1.2 \left(\frac{\nu}{3.02 \text{ GHz}} \right)^{-0.7} \left(\frac{\theta_b}{8''} \right)^{10/3} \mu\text{Jy beam}^{-1}. \quad (3.19)$$

In our observations, the confusion limit at 0.65 GHz for the resolution of $3.8''$ would be $0.3 \mu\text{Jy beam}^{-1}$, which is one third of the expected sensitivity ($10 \mu\text{Jy beam}^{-1}$). In the

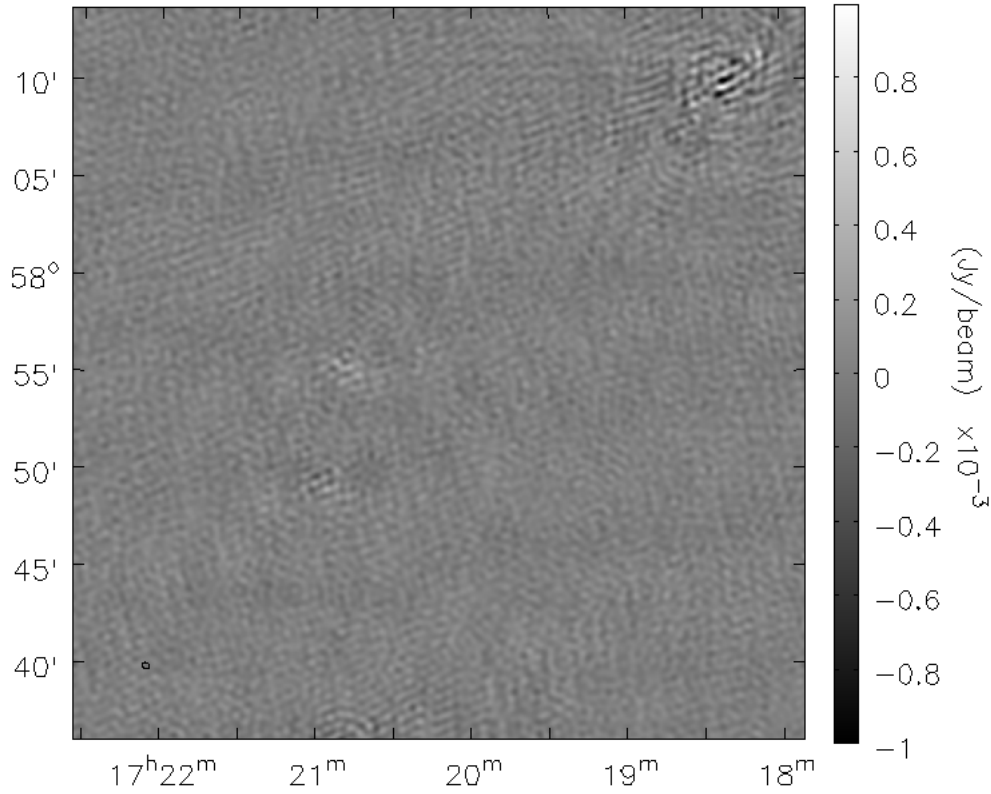


Figure 3.10 Stokes V image for low resolution map. The sensitivity is $50 \mu\text{Jy beam}^{-1}$ for a beam size of $20.5''$.

practice, the best resolution we obtained was $4.6''$ and, using equation (3.19), we estimated a confusion noise at the $0.6 \mu\text{Jy beam}^{-1}$ level. Another largely used expression is taken from Condon (1974):

$$\sigma_{c,C} \simeq 200 \left(\frac{\nu}{\text{GHz}} \right)^{-0.7} \left(\frac{\theta_b}{\text{arcmin}} \right)^2 \mu\text{Jy beam}^{-1}, \quad (3.20)$$

which uses a flatter power law for the beam size dependence and a different normalization. For what concerns our work, we used this empiric expression with $\nu = 0.60 \text{ GHz}$ to obtain different values of confusion estimation for different beams we got in the images presented above. Results are summarized in Table 3.2.

	High resolution image ($\theta_b = 4.6''$)		Low resolution image ($\theta_b = 20.5''$)	
$\sigma_{c,ETC}$	$0.6 \mu\text{Jy beam}^{-1}$		$88 \mu\text{Jy beam}^{-1}$	
$\sigma_{c,C}$	$1.6 \mu\text{Jy beam}^{-1}$		$33 \mu\text{Jy beam}^{-1}$	
	Stokes I	Stokes V	Stokes I	Stokes V
noise rms	$36 \mu\text{Jy beam}^{-1}$	$20 \mu\text{Jy beam}^{-1}$	$230 \mu\text{Jy beam}^{-1}$	$53 \mu\text{Jy beam}^{-1}$
$\sigma_{\text{max}}/\text{rms}$	0.04	0.08	0.38	1.6

Table 3.2 Summary of the confusion level estimates for different angular resolutions. The noise rms values are reported for the Stokes I and V images at different resolutions. The last row shows the ratio between the worst estimate of confusion noise and the noise rms.

For the high resolution image, the estimation with Eq. (3.20) is almost three times higher than with Eq. (3.19). Images at low resolution, which have a larger synthesized beam, show

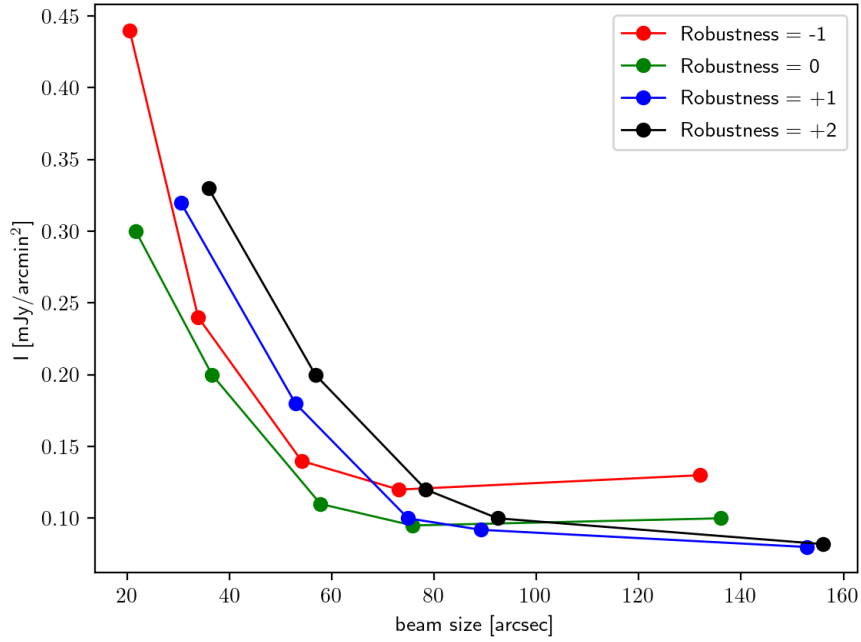


Figure 3.11 Measured brightness sensitivity as a function of the beam size. Colors are for different robustness (legend). For each robustness, five decreasing maximum baseline length are considered: 3 km, 2 km, 1.5 km, 1 km and 0.5 km.

the opposite relation. In the sixth row, the measured rms noise is reported for both Stokes I and Stokes V images of both image types. For the high resolution image, the confusion noise is a small fraction of the measured noise, regardless how it is estimated. Even in the low resolution image the confusion level only contributes to a small fraction of the measured rms noise, indicating that our Stokes I image are noise rather than confusion limited. The fact that the Stokes V noise rms is below the confusion level should not be worrying since the image is not affected by confusion but confirms that, at 20.5'' beam size, the confusion contribute to the rms is similar to the thermal noise's.

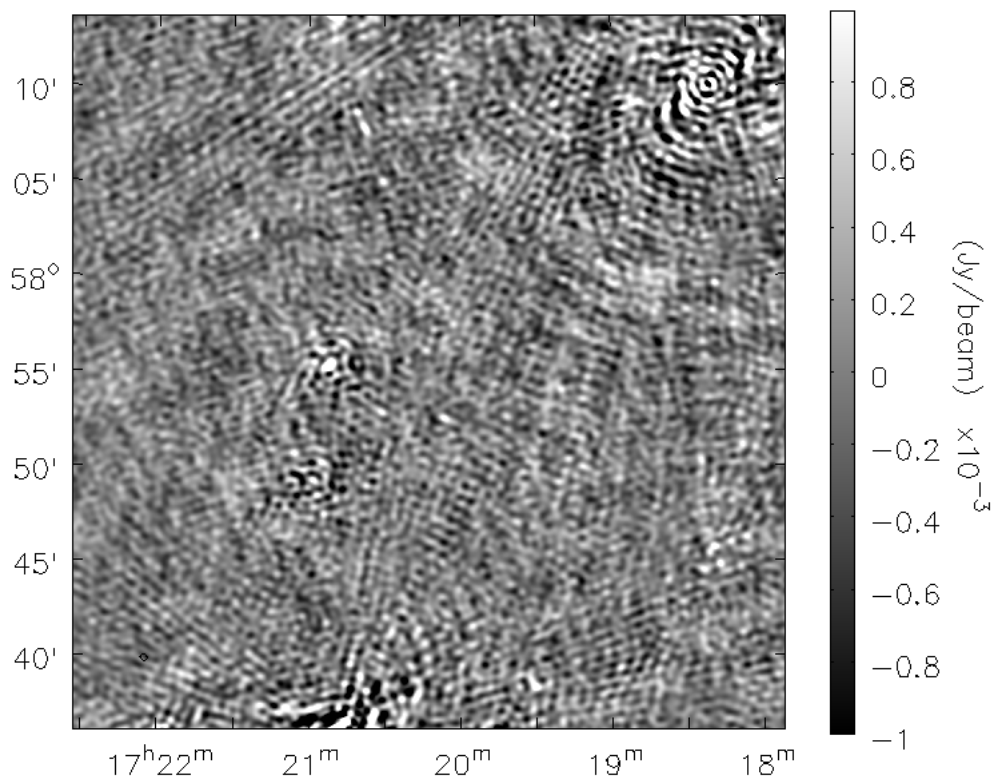


Figure 3.12 Low resolution map after source subtraction on the visibility plane. The measured rms is $230 \mu\text{Jy beam}^{-1}$ for a beam size of $20.5''$.

Chapter 4

Results

In chapter § 2, we explained how to obtain a theoretical estimation of the synchrotron emission S_{th} for a certain distribution of DM. These models are sensitive to the magnetic field, diffusion properties, the DM density profile, for which many assumptions can be made. In particular, they are also sensitive to DM particles parameters, such as the mass M_χ and the velocity-averaged, annihilation cross section $\langle\sigma v\rangle$, which this thesis work aims to constraint. In the previous chapter (§ 3), we described how we reduced data in order to obtain several images, characterized by different beam sizes and sensitivities. An hypothetical diffuse emission could be present in these images and be compared with the theoretical expectation. Alternatively, the lack of detection of diffuse signal still allows to constrain model parameters. In this section we describe the search for DM-induced diffuse emission in Draco and the subsequent upper limits on the DM particle model.

4.1 Model parameters

A set of parameters were assumed to model the expected signal. The modeling process has been described in § 2.2.1 and here we are following the same steps to describe the parameters we used for our benchmark model.

The electron injection term (Eq. (2.6)) requires the DM density profile $\rho(r)$, the number of e^+/e^- pairs per annihilation and per energy interval dN_e^a/dE , the particle cross section and mass. The latter are the parameters we want to constrain. We considered values between 10^{-26} and 10^{-21} $\text{cm}^3 \text{s}^{-1}$ for the cross section and masses between 10 GeV and 1 TeV. The dN_e^a/dE term only depends on the chosen annihilation channel and since there is not a preferable one (see § 2.1), we considered the four usually used in the literature (e.g. in Regis et al., 2014), namely $b\bar{b}$, $\tau^+\tau^-$, $\mu^+\mu^-$ and W^+W^- . Since the constraints are always more stringent considering annihilations, we ignored the case of WIMP decays. Any other parameter has been assumed as a fixed value to obtain a standard model for the expected signal. For the DM density distribution we assume an NFW profile (Eq. (1.80)) with a scale radius $r_0 = 0.35$ kpc and a halo normalization $\rho_0 = 2.3 \cdot 10^8 \text{ M}_\odot \text{ kpc}^{-3}$. These values are taken from Martinez (2015).

The injection term so obtained is entered in the diffusion equation (Eq. (2.8)) as the source of an ultrarelativistic electron/positron population. To characterize the diffusion, we considered the standard scenario where the diffusion coefficient D is obtained through estimates of the ratio between the coherent and the turbulent component of the magnetic field (Eq. (2.11)). We assumed the benchmark value for dwarf galaxies $D_0 = 3 \cdot 10^{28} \text{ cm}^2 \text{ s}^{-1}$ to be constant over the galaxy extension.

The magnetic field is a crucial parameter as it influences both the diffusion coefficient and the synchrotron emissivity but, as said, it is hard to determine in dwarf galaxies. In fact, as any other dSph, Draco does not show evidences of recent SF (Aparicio et al., 2001) but it should

have a relic magnetic field from the ancient starburst that built its stellar population. With the relation from [Chyży et al. \(2011\)](#), one can infer an intensity $B_0 = 1 \mu\text{G}$ as a benchmark value for any dSph (e.g., [Beck and Colafrancesco, 2016](#)), and assume the magnetic field distribution to follow an exponential decrease:

$$B(r) = B_0 e^{-r/r_h} \quad (4.1)$$

with r_h being the half-light radius. Assuming a gaussian stellar profile, we assumed a projected half-light radius of $10'$ ([Martinez, 2015](#)).

The magnetic field is used together with the equilibrium distribution $n_e(r, E)$ to compute the synchrotron emissivity (Eq. (2.14)). In turn, the emissivity is integrated as in Eq. (2.17) to determine the theoretical flux density S_{th} , for which the distance of the galaxy is required. The distance of Draco from the Sun is set to $d = 76 \text{ kpc}$ ([McConnachie, 2012](#)).

We also point out that we used a value of $2.2 \cdot 10^{-26} \text{ cm}^3 \text{ s}^{-1}$ for the thermal cross section ([Steigman et al., 2012](#)) as a more precise value for WIMP masses above 10 GeV than the canonical $3 \cdot 10^{-26} \text{ cm}^3 \text{ s}^{-1}$. This limit is shown with a black dashed line in all the following plots.

4.2 Analysis method

We have shown in § 2.2.1 that a theoretical synchrotron emission with flux density S_{th} due to DM annihilation/decay can be computed as a function of particle cross section $\langle\sigma v\rangle$ and mass M_χ . In order to compute the theoretical synchrotron emission one needs to compute the electron injection (equation 2.6) and then solve the diffusion equation (2.8) which, in turn, gives the spatial and energy distribution of relativistic electrons necessary to compute the synchrotron emissivity (equation 2.14). We used the code developed in [Regis et al. \(2014\)](#) to determine the synchrotron emissivity model as a function of particle mass and cross section.

A likelihood function \mathcal{L} is computed for each synchrotron model:

$$\mathcal{L}(\langle\sigma v\rangle, M_\chi) = e^{-\chi^2/2}, \quad (4.2)$$

with

$$\chi^2 = \frac{1}{N_{\text{pix}}^{\text{beam}}} \sum_{i=1}^{N_{\text{pix}}} \left(\frac{S_{\text{th}}^i(\langle\sigma v\rangle, M_\chi) - S_{\text{obs}}^i}{\sigma_{\text{rms}}^i} \right)^2, \quad (4.3)$$

where $N_{\text{pix}}^{\text{beam}}$ is the number of image pixels per beam area, S_{th}^i is the model output for each pixel i , S_{obs}^i is the observed flux density and σ_{rms}^i is the rms noise. We note that, in principle, the noise can be spatially dependent, i.e. its variance changes across the observed image. In practice we assumed the noise to be constant across the map, measured in an “empty” area where no sources are visible. To determine the statistical relevance of an eventual detection, we used the λ_d estimator ([Regis et al., 2015b](#)):

$$\lambda_d = -2 \ln \left(\frac{\mathcal{L}_{\text{null}}}{\mathcal{L}_{\text{bf}}} \right), \quad (4.4)$$

where $\mathcal{L}_{\text{null}}$ is the likelihood of no signal (i.e., $S_{\text{th}} = 0$) and \mathcal{L}_{bf} the likelihood of the best fit model. If \mathcal{L}_{bf} is higher than $\mathcal{L}_{\text{null}}$, the λ_d estimator becomes positive and we have a preference for the presence of the annihilation signal. The statistical significance of this preference is given by $\sqrt{\lambda_d} \sigma$ which is the confidence level at which the null hypothesis (no signal) can be rejected. If the preference is above 3σ , it is considered as a detection.

Whether the detection level is obtained or not, bounds at 95% C.L. from the best fit are determined as follow: for a given set of fixed parameters $\vec{\Pi}_0 = (B, D, r_b, d, \dots)$, namely those

listed in the previous section, the cross section remains the only free parameter. It is subject to another likelihood profiling with

$$\lambda_c(\langle\sigma v\rangle) = -2 \ln \left[\frac{\mathcal{L}(\vec{\Pi}_0, \langle\sigma v\rangle)}{\mathcal{L}(\vec{\Pi}_0, \langle\sigma v\rangle_{\text{b.f.}})} \right] \quad (4.5)$$

following a χ^2 -distribution and with $\langle\sigma v\rangle_{\text{b.f.}}$ being the best-fit value for the cross section. Varying the cross section from the best fit value, 95% C.L. are determined.

Going back to Eq. (4.4), if $\lambda_d < 0$ we have a preference for the null hypothesis (i.e. $S_{\text{th}} = 0$), we still use equation (4.5) but only the upper limit is calculated by increasing the cross section until the estimator reaches $\lambda_c = 2.71$, which corresponds to 2σ in case of one-sided probabilities. We compute the analysis for 12 masses, evenly spaced on a logarithmic scale, from 10 GeV to 1 TeV in order to obtain plots of § 4.3.

4.3 Results

We used the Stokes I map (Figure 3.12) and the relative Stokes V map (Figure 3.8) for the following analysis. From now on, we will simply refer to them as Stokes I and Stokes V, respectively. Both maps have the same resolution, 20.5'' due to the exclusion of baselines longer than 3 km. In the following sections, we describe results of the analysis on the two maps separately.

4.3.1 Results from the Stokes I map

The Stokes I map reaches a sensitivity of $230 \mu\text{Jy beam}^{-1}$ and is sensitive to emission on scales up to $\sim 19'$ at the central frequency (25.8' at the lowest frequency of 450 MHz). It shows no sign of extended emission and the only noticeable feature are artifacts around bright sources due to mis-subtraction/calibration errors. We used the central area of 15' radius in this map to compute the likelihood described in § 4.2, assuming the benchmark model of § 4.1.

The likelihood analysis led to a preference for the presence of annihilation signal with $\sigma = 1.97$ for $M_\chi = 1$ TeV, mildly decreasing for lower masses. As said, this cannot be considered as a detection since the significance is below 3σ . Moreover, the preference is likely due to residuals left after source subtraction - as already pointed out in § 3.4. The deconvolution process made to obtain the Stokes I map (Figure 3.12) may have overcleaned some of the residuals, artificially generating an excess in the map - although this is only a tentative explanation and a further investigation is needed. The pointing center, which corresponds to the center of the optical galaxy, is 5.3' away from the brightest radio source. The signal due to DM annihilation is expected to match the center of the galaxy but we did not constrain the search area when the code was run.

Even though this preference is likely to be artificial, we report the bounds obtained for the annihilation cross section as function of masses. In Figure 4.1 we show the best fit lines and relative 95% C.L. intervals with coloured bands for the four considered annihilation channels. We separated channels in two panels for clarity. In the top one, we have results for quarks and muons. The best fit line for the channel $b\bar{b}$ begins at 20 GeV because, below this mass value, the estimator λ_d drops at lower masses. For the bosonic channel, annihilation is only allowed above 100 GeV because of the large mass of W bosons.

We note that the cross section grows with the mass for every channel but with different slopes. By looking at the injection term expression (Eq. (2.6)), it is clear that for a fixed value of q_e^a , the cross section is proportional to the squared number density. Different slopes instead are determined by the fact that leptonic channels ($\mu^+\mu^-$, $\tau^+\tau^-$) provide harder spectra for e^+/e^- than quarks and bosons, which have a similar trend. This makes the bounds of leptonic

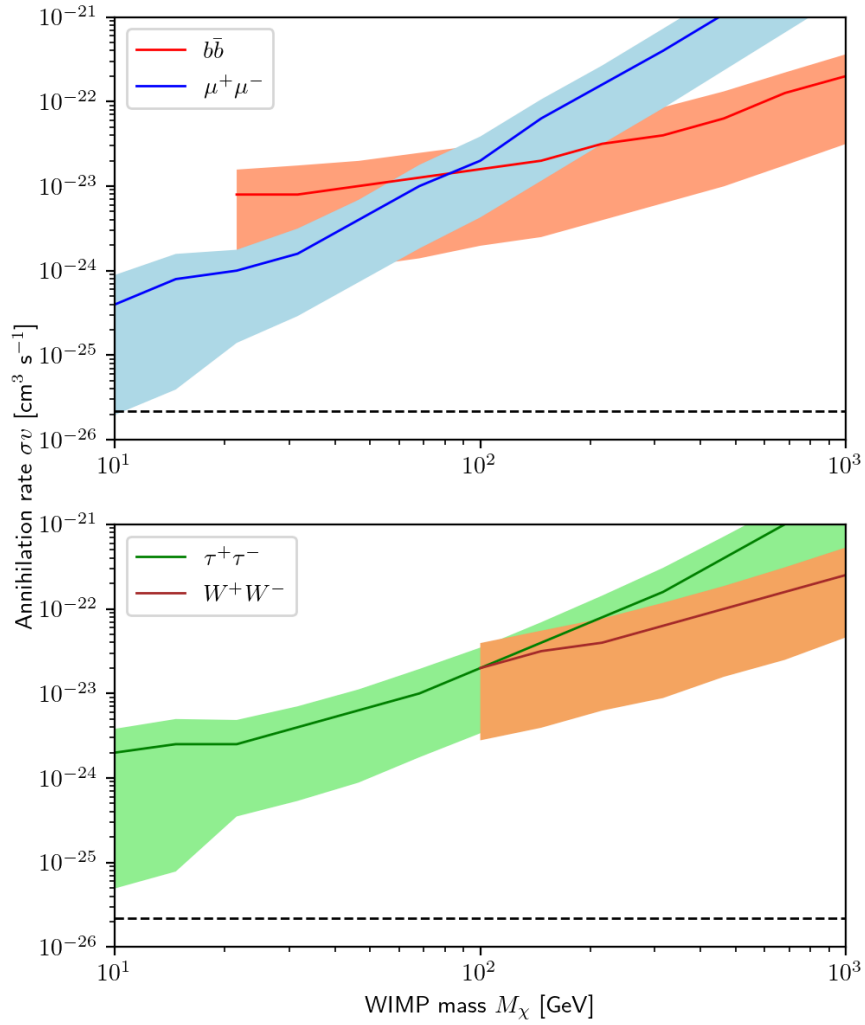


Figure 4.1 Best-fit cross-sections as function of WIMP mass (lines) and relative bounds within 2σ for the Stokes I map. Top panel: results for $b\bar{b}$ and $\mu^+\mu^-$ annihilation channels. Bottom panel: results for $\tau^+\tau^-$ and W^+W^- . The “thermal” cross section is plotted with a dashed black line.

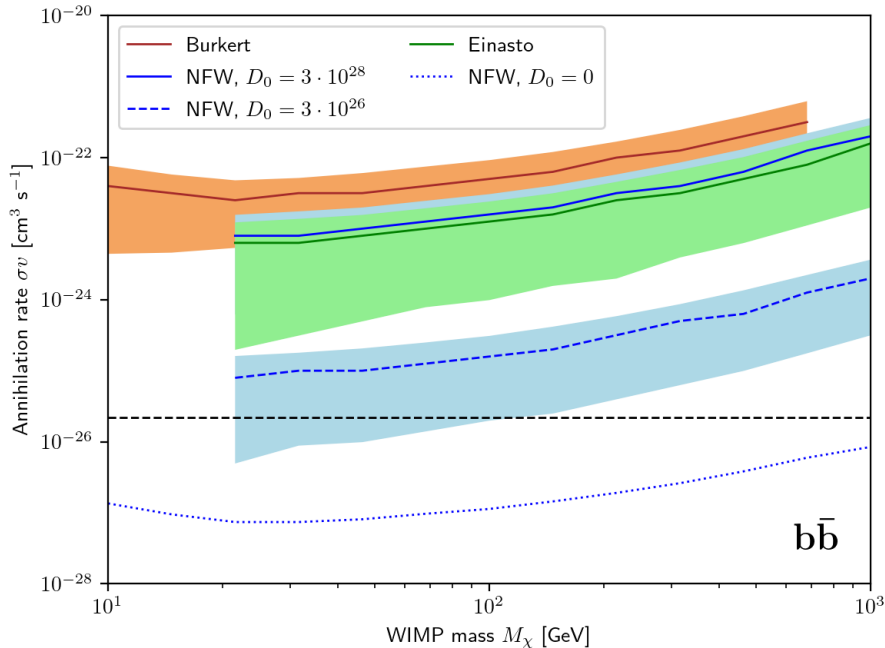


Figure 4.2 Best fit lines and relative 95% C.L. contours derived from the Stokes I map for annihilation into quarks, shown for three DM profiles: Burkert (green), Einasto (blue) and NFW (red, same as top panel of Figure 4.1, $b\bar{b}$ channel). For the NFW profile, we also show the case of the lower limit of the diffusion coefficient (dashed) and the loss-at-injection scenario for which the null hypothesis is preferred, thus we only plot the upper 95% C.L. (dotted, only upper bounds).

channels to be more stringent at low masses and less stringent above 100 GeV, than those of quarks and bosons.

We studied the impact that different DM profiles and diffusion scenarios have on the particle constraints. For the former, we used the Burkert (Eq. (1.82)), which has a shallow central profile, and the cuspy Einasto (Eq. (1.81)) profile, more similar to the NFW one. The relative parameters (scale radius and halo normalization) are summarized in Table 4.1, together with those of the NFW profile.

Profile	Type	r_0 [kpc]	ρ_0 [$10^8 M_\odot \text{ kpc}^{-3}$]
NFW	Cuspy	0.35	2.3
Burkert	Cored	0.13	13.7
Einasto	Cuspy	0.44	0.36

Table 4.1 DM profiles and relative type (cuspy or core), scale radius r_0 and density normalization ρ_0 . For the Einasto profile, the slope parameter is the canonical $\alpha = 0.17$ (see Eq. (1.81)).

We also considered two different diffusion coefficients, a lower limit for the diffusion coefficient ($10^{26} \text{ cm}^2 \text{ s}^{-1}$), obtained by imposing a diffusion time shorter than the age of the Universe (see Eq. (2.13)) and an extreme, loss-at-injection scenario, i.e. $D_0 = 0$. Results are shown in Figure 4.2, where we compare bounds for the $b\bar{b}$ annihilation channel only. We assumed this channel simply because it has the shallowest trend, thus the plot requires a narrowest range of cross sections - but the behaviour is similar to other annihilation channels. Considering the three cases of Table 4.1, the NFW profile allow higher cross sections as best fit values compared to the Burkert and Einasto ones. This is expected as a cuspy profile boost the theoretical signal at small radii. In fact, for a fixed luminosity, a peaked flux density profile

is easier to detect than a broad, low surface brightness signal. This allows to place lower best fit values on the annihilation cross section.

The same applies for different diffusion coefficients: a lower value of D_0 generates a more spatially concentrated emission, especially for a cuspy profile like NFW. The loss-at-injection scenario ($D_0 = 0$) takes it to the extreme, such that there is no detection but we could only place upper limits. In order to compute the latter, we allowed the code to explore cross sections down to $10^{-28} \text{ cm}^3 \text{ s}^{-1}$.

4.3.2 Results from the Stokes V map

We ran the likelihood analysis on the Stokes V images not to place significant constraints on the DM particle - as DM-induced synchrotron emission is expected not to be circularly polarized - but to use the Stokes V map as our best noise estimate and, therefore, to assess the most optimistic constraints that can be placed by our observations.

We found no preference for the annihilation signal in the Stokes V map and upper 95% C.L. are shown in Figure 4.3 for the benchmark model described in § 4.1. Bounds for the $b\bar{b}$

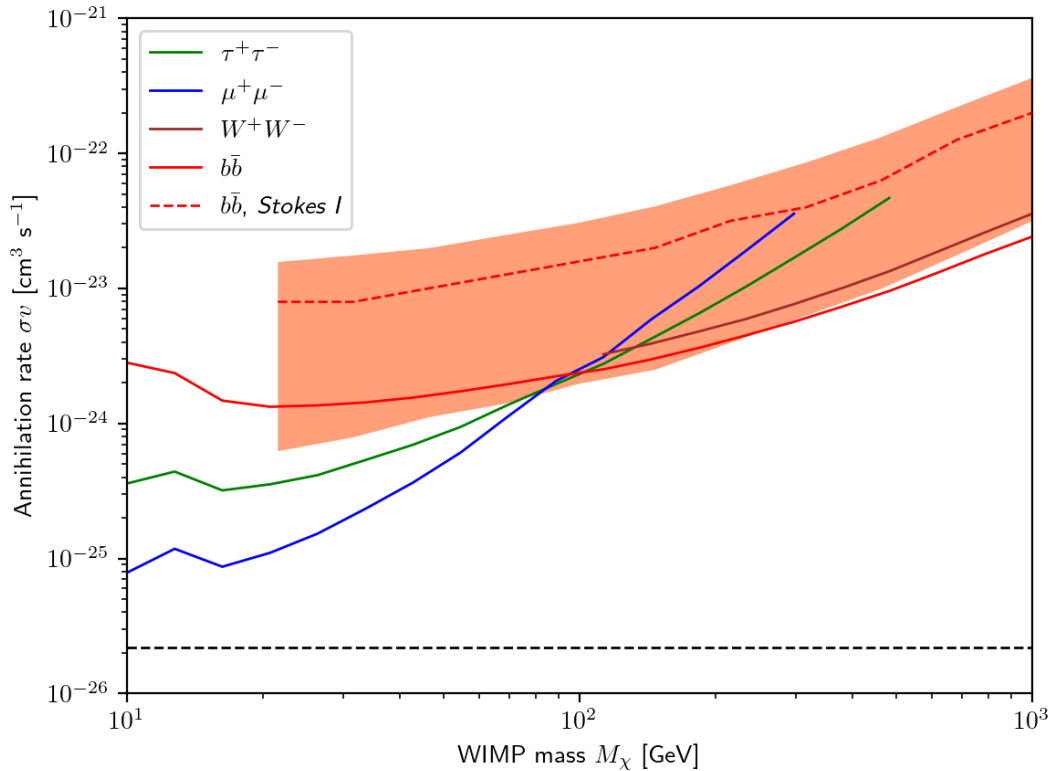


Figure 4.3 Upper 95% C.L. from the analysis on Stokes V map for annihilation into $b\bar{b}$ (red), $\tau^+\tau^-$ (green), $\mu^+\mu^-$ (blue) and W^+W^- (brown). Best fit (dashed red) and 2σ limits from Figure 4.1 are showed for the $b\bar{b}$ channel only, as a comparison.

channel from the Stokes I map detection are also included for a comparison. Upper limits from the analysis of the Stokes V map are almost an order to magnitude fainter than the best fit line from the Stokes I map for the same annihilation channel. Moreover, upper limits from leptonic channels reach the $\sigma v \sim 10^{-25} \text{ cm}^3 \text{ s}^{-1}$ for $M_\chi < 20 \text{ GeV}$, which is less than one order of magnitude above the thermal level.

Note also that for these masses the trend (cross section increase with mass) is inverted. This can be explained considering that, at those masses, the induced e^+/e^- distribution might

peak at energies below the corresponding synchrotron power peak (Regis et al., 2014).

4.4 Comparison with previous works

We place our results in the context of the most recent literature constraints (Regis et al., 2021). Figure 2.7 shows bounds for benchmark models of relative papers, for the $b\bar{b}$ annihilation channel. Upper limits are obtained from different types of observations. Kar et al. (2019), Regis et al. (2014) and Basu et al. (2021) combine observations on several dSphs, whereas Vollmann et al. (2020) and Regis et al., 2017 obtain limits from deep observations on single targets. The best upper limits are obtained by observations of the LMC (Regis et al., 2021) that has one of the highest \mathcal{J} -factors (after the GC) and larger magnetic fields ($4.3 \mu\text{G}$) compared to dSphs. These constraints are even better than those obtained from high energy observations (Ackermann et al., 2015),

Our best fit values obtained from the Stokes I map cannot be compared with other upper limits, but are reported here anyway for the sake of completeness. In case that the calibration and source subtraction can be improved and the noise level of the Stokes I map can be lowered to the level of the Stokes V map, our observations would lead to upper limits that are still approximately three orders of magnitude higher than the best ones (Regis et al., 2021) for sub-TeV particles. However, considering the pilot nature of our observations (only ~ 4 hours long), our results are encouraging in the view of longer integrations on Draco.

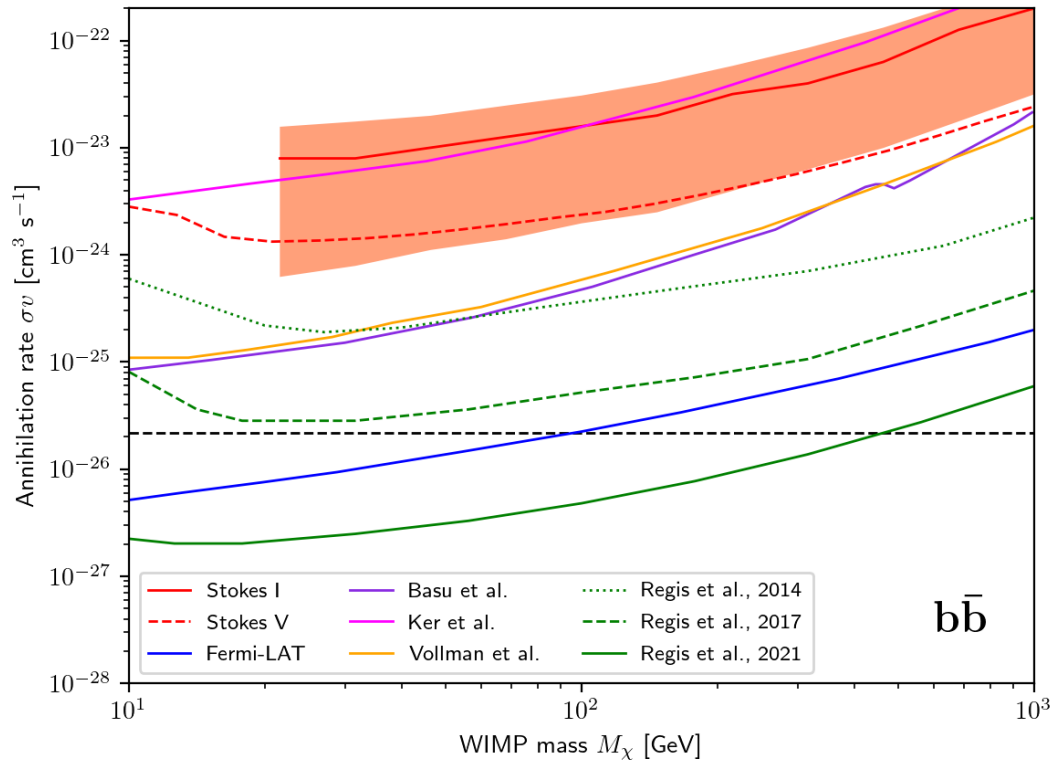


Figure 4.4 State of the art upper limits on DM particle. Our best fit derived from the Stokes I map and upper limit derived from the Stokes V analysis are included too. We plotted the least stringent upper limits among the one derived by Regis et al. (2021).

Chapter 5

Conclusions

DM is a fundamental component of the Universe and a solid pillar of the Standard Cosmological Model. Its intrinsic nature, however, is still largely unknown and various approaches are used to investigate its properties. WIMP is a class of theoretical particles, a candidate to be the constituent of DM. Theoretical models predict that WIMPs are able to annihilate/decay into Standard Model particles and that electrons/positrons pairs are among the main secondary products of these interactions. Relativistic electrons so obtained are expected to produce a diffused, observable synchrotron emission if a magnetic field is present. The detection of this emission would be an evidence of the particle nature of DM and would allow to determine the properties of WIMPs. The non detection is still useful, as it leads to put constraints on the annihilation cross section of the WIMP as a function of its mass.

In this thesis we have presented a search for this signal in the Draco dSph, that is one of the most DM-dominated objects known. We analyzed 4 h of observations from the GMRT, taken with a large bandwidth (200 MHz) around the central frequency 650 MHz, using the full array configuration of the telescope in order to maximize the sensitivity. We discarded a large fraction (65%) of data during the calibration and self-calibration process, including all the data from 8 antennas out of 30. We produced an high resolution map with beam size of $4.60''$ with a rms noise of $36 \mu\text{Jy beam}^{-1}$, whose model has been used to perform the subtraction of compact sources in the visibility plane. After the subtraction, we used baselines with lengths below 3 km to produce low resolution maps with a beam size of $20.5''$. The resulting flux density map (Stokes I map) has a rms noise of $230 \mu\text{Jy beam}^{-1}$ while the Stokes V map, which brings the best sensitivity achievable for our observations, reaches a value of $50 \mu\text{Jy beam}^{-1}$. We modelled the theoretical emission of Draco in order to statistically compare expected and measured flux density maps. We assumed a NFW profile for the DM distribution, a standard diffusion for relativistic electrons and a $1 \mu\text{G}$, exponentially decreasing magnetic field.

The comparison has been implemented through a maximum likelihood technique, which led to a marginal evidence ($\sigma \simeq 2$ in the best case) of the diffused emission. This low significant detection is likely due to residuals of a discrete source that has not been fully subtracted. Assuming this is an actual DM signal, we still presented best fit values for the cross section for a range of particle masses (10 GeV - 1 TeV) and for different annihilation channels ($b\bar{b}$, $\tau^+\tau^-$, $\mu^+\mu^-$ and W^+W^-). At 100 GeV, where cross sections are similar for every annihilation channel, we obtain a value of $\sim 10^{-23} \text{ cm}^3 \text{ s}^{-1}$, almost three orders of magnitude above the “thermal” cross section. The cross section increases with mass but with different slopes for different annihilation channels, due to different spectra for the electronic populations injected. Exploring different choices for DM profile and the diffusion mechanism, we understood how the values obtained are really sensible to changes in the model assumptions. Thus, a better characterization of the magnetic field, the diffusion and the DM profile of dSphs seems necessary in order to achieve less model-dependent bounds. Even though the comparison with state of the art upper limits place our results four orders of magnitude above the best one from radio

observations, we can still be optimistic on future observations of Draco: running the analysis on the Stokes V map, we obtain upper limits on the cross section, estimating the best bounds we could obtain from our observations. Roughly an order of magnitude improvement can be achieved for every annihilation channel and, for the $\mu^+\mu^-$ channel, a cross section just four times above the “thermal” value would be obtained at the 10 GeV scale. A longer exposure on Draco, together with improved calibration and source subtraction, would bring substantially lower bounds.

Bibliography

- Abdallah, H. et al. (Sept. 2016). “Search for Dark Matter Annihilations towards the Inner Galactic Halo from 10 Years of Observations with H.E.S.S.” In: *Physical Review Letters* 117.11. ISSN: 1079-7114. DOI: [10.1103/physrevlett.117.111301](https://doi.org/10.1103/physrevlett.117.111301). URL: <http://dx.doi.org/10.1103/PhysRevLett.117.111301>.
- Abeyssekara, A.U. et al. (Feb. 2018). “A search for dark matter in the Galactic halo with HAWC”. In: *Journal of Cosmology and Astroparticle Physics* 2018.02, pp. 049–049. ISSN: 1475-7516. DOI: [10.1088/1475-7516/2018/02/049](https://doi.org/10.1088/1475-7516/2018/02/049). URL: <http://dx.doi.org/10.1088/1475-7516/2018/02/049>.
- Abramowski, A. et al. (Dec. 2014). “Search for dark matter annihilation signatures in H.E.S.S. observations of dwarf spheroidal galaxies”. In: *Phys. Rev. D* 90 (11), p. 112012. DOI: [10.1103/PhysRevD.90.112012](https://doi.org/10.1103/PhysRevD.90.112012). URL: <https://link.aps.org/doi/10.1103/PhysRevD.90.112012>.
- Acciari, V. A. et al. (Aug. 2010). “VERITAS SEARCH FOR VHE GAMMA-RAY EMISSION FROM DWARF SPHEROIDAL GALAXIES”. In: *The Astrophysical Journal* 720.2, pp. 1174–1180. ISSN: 1538-4357. DOI: [10.1088/0004-637x/720/2/1174](https://doi.org/10.1088/0004-637x/720/2/1174). URL: <http://dx.doi.org/10.1088/0004-637x/720/2/1174>.
- Ackermann, M. et al. (Nov. 2015). “Searching for Dark Matter Annihilation from Milky Way Dwarf Spheroidal Galaxies with Six Years of Fermi Large Area Telescope Data”. In: *Physical Review Letters* 115.23. ISSN: 1079-7114. DOI: [10.1103/physrevlett.115.231301](https://doi.org/10.1103/physrevlett.115.231301). URL: <http://dx.doi.org/10.1103/PhysRevLett.115.231301>.
- Ackermann, M. et al. (May 2017). “The Fermi Galactic Center GeV Excess and Implications for Dark Matter”. In: *The Astrophysical Journal* 840.1, p. 43. ISSN: 1538-4357. DOI: [10.3847/1538-4357/aa6cab](https://doi.org/10.3847/1538-4357/aa6cab). URL: <http://dx.doi.org/10.3847/1538-4357/aa6cab>.
- Aghanim, N. et al. (Sept. 2020). “Planck 2018 results”. In: *A&A* 641, A6. ISSN: 1432-0746. DOI: [10.1051/0004-6361/201833910](https://doi.org/10.1051/0004-6361/201833910). URL: <http://dx.doi.org/10.1051/0004-6361/201833910>.
- Albareti, Franco D. et al. (Oct. 2015). “Constraint on the time variation of the fine-structure constant with the SDSS-III/BOSS DR12 quasar sample”. In: *MNRAS* 452.4, pp. 4153–4168. DOI: [10.1093/mnras/stv1406](https://doi.org/10.1093/mnras/stv1406). arXiv: [1501.00560](https://arxiv.org/abs/1501.00560) [astro-ph.CO].
- Albert, A. et al. (Feb. 2018). “Dark Matter Limits from Dwarf Spheroidal Galaxies with the HAWC Gamma-Ray Observatory”. In: *The Astrophysical Journal* 853.2, p. 154. DOI: [10.3847/1538-4357/aaa6d8](https://doi.org/10.3847/1538-4357/aaa6d8). URL: <https://doi.org/10.3847/1538-4357/aaa6d8>.
- Aleksić, J et al. (June 2011). “Searches for dark matter annihilation signatures in the Segue 1 satellite galaxy with the MAGIC-I telescope”. In: *Journal of Cosmology and Astroparticle Physics* 2011.06, pp. 035–035. ISSN: 1475-7516. DOI: [10.1088/1475-7516/2011/06/035](https://doi.org/10.1088/1475-7516/2011/06/035). URL: <http://dx.doi.org/10.1088/1475-7516/2011/06/035>.
- Aparicio, Antonio, Ricardo Carrera, and David Martínez-Delgado (Nov. 2001). “The Star Formation History and Morphological Evolution of the Draco Dwarf Spheroidal Galaxy”. In: *AJ* 122.5, pp. 2524–2537. DOI: [10.1086/323535](https://doi.org/10.1086/323535). arXiv: [astro-ph/0108159](https://arxiv.org/abs/astro-ph/0108159) [astro-ph].
- Basu, Arghyadeep et al. (Jan. 2021). “Stringent constraint on the radio signal from dark matter annihilation in dwarf spheroidal galaxies using the TGSS”. In: *Monthly Notices of the Royal*

- Astronomical Society* 502.2, pp. 1605–1611. ISSN: 1365-2966. DOI: [10.1093/mnras/stab120](https://doi.org/10.1093/mnras/stab120). URL: <http://dx.doi.org/10.1093/mnras/stab120>.
- Beck, G. and S. Colafrancesco (May 2016). “A Multi-frequency analysis of dark matter annihilation interpretations of recent anti-particle and γ -ray excesses in cosmic structures”. In: *Journal of Cosmology and Astroparticle Physics* 2016.05, pp. 013–013. ISSN: 1475-7516. DOI: [10.1088/1475-7516/2016/05/013](https://doi.org/10.1088/1475-7516/2016/05/013). URL: <http://dx.doi.org/10.1088/1475-7516/2016/05/013>.
- Beck, Geoff (2020). *Radio-Frequency Searches for Dark Matter in Dwarf Galaxies*. arXiv: [2007.01689](https://arxiv.org/abs/2007.01689) [astro-ph.HE].
- Bergström, Lars, Piero Ullio, and James H. Buckley (Aug. 1998). “Observability of γ rays from dark matter neutralino annihilations in the Milky Way halo”. In: *Astroparticle Physics* 9.2, pp. 137–162. ISSN: 0927-6505. DOI: [10.1016/S0927-6505\(98\)00015-2](https://doi.org/10.1016/S0927-6505(98)00015-2). URL: [http://dx.doi.org/10.1016/S0927-6505\(98\)00015-2](http://dx.doi.org/10.1016/S0927-6505(98)00015-2).
- Bertone, Gianfranco and Dan Hooper (Oct. 2018). “History of dark matter”. In: *Reviews of Modern Physics* 90.4. ISSN: 1539-0756. DOI: [10.1103/revmodphys.90.045002](https://doi.org/10.1103/revmodphys.90.045002). URL: <http://dx.doi.org/10.1103/RevModPhys.90.045002>.
- Bertone, Gianfranco, Günter Sigl, and Joseph Silk (Nov. 2002). “Annihilation radiation from a dark matter spike at the Galactic Centre”. In: *Monthly Notices of the Royal Astronomical Society* 337.1, pp. 98–102. ISSN: 1365-2966. DOI: [10.1046/j.1365-8711.2002.05892.x](https://doi.org/10.1046/j.1365-8711.2002.05892.x). URL: <http://dx.doi.org/10.1046/j.1365-8711.2002.05892.x>.
- Bonnivard, V. et al. (Aug. 2015). “Dark matter annihilation and decay in dwarf spheroidal galaxies: the classical and ultrafaint dSphs”. In: *Monthly Notices of the Royal Astronomical Society* 453.1, pp. 849–867. ISSN: 0035-8711. DOI: [10.1093/mnras/stv1601](https://doi.org/10.1093/mnras/stv1601). eprint: <https://academic.oup.com/mnras/article-pdf/453/1/849/13769186/stv1601.pdf>. URL: <https://doi.org/10.1093/mnras/stv1601>.
- Borriello, E., A. Cuoco, and G. Miele (Jan. 2009). “Radio constraints on dark matter annihilation in the galactic halo and its substructures”. In: *Physical Review D* 79.2. ISSN: 1550-2368. DOI: [10.1103/physrevd.79.023518](https://doi.org/10.1103/physrevd.79.023518). URL: <http://dx.doi.org/10.1103/PhysRevD.79.023518>.
- Briggs, Daniel S., Frederic R. Schwab, and Richard A. Sramek (Jan. 1999). “Imaging”. In: *Synthesis Imaging in Radio Astronomy II*. Ed. by G. B. Taylor, C. L. Carilli, and R. A. Perley. Vol. 180. Astronomical Society of the Pacific Conference Series, p. 127.
- Bringmann, Torsten et al. (July 2018). “DarkSUSY 6: an advanced tool to compute dark matter properties numerically”. In: *Journal of Cosmology and Astroparticle Physics* 2018.07, pp. 033–033. ISSN: 1475-7516. DOI: [10.1088/1475-7516/2018/07/033](https://doi.org/10.1088/1475-7516/2018/07/033). URL: <http://dx.doi.org/10.1088/1475-7516/2018/07/033>.
- Bullock, J. S. et al. (Mar. 2001). “Profiles of dark haloes: evolution, scatter and environment”. In: *Monthly Notices of the Royal Astronomical Society* 321.3, pp. 559–575. ISSN: 1365-2966. DOI: [10.1046/j.1365-8711.2001.04068.x](https://doi.org/10.1046/j.1365-8711.2001.04068.x). URL: <http://dx.doi.org/10.1046/j.1365-8711.2001.04068.x>.
- Burkert, A. (July 1995). “The Structure of Dark Matter Halos in Dwarf Galaxies”. In: *The Astrophysical Journal* 447.1. ISSN: 0004-637X. DOI: [10.1086/309560](https://doi.org/10.1086/309560). URL: <http://dx.doi.org/10.1086/309560>.
- Calura, F., G. A. Lanfranchi, and F. Matteucci (Mar. 2008). “The evolution of the photometric properties of Local Group dwarf spheroidal galaxies”. In: *A&A* 484.1, pp. 107–118. ISSN: 1432-0746. DOI: [10.1051/0004-6361:20078465](https://doi.org/10.1051/0004-6361:20078465). URL: <http://dx.doi.org/10.1051/0004-6361:20078465>.
- Carretti, Ettore et al. (Jan. 2013). “Giant magnetized outflows from the centre of the Milky Way”. In: *Nature* 493.7430, pp. 66–69. ISSN: 1476-4687. DOI: [10.1038/nature11734](https://doi.org/10.1038/nature11734). URL: <http://dx.doi.org/10.1038/nature11734>.

- Cembranos, J. A. R. et al. (Apr. 2011). “Photon spectra from WIMP annihilation”. In: *Phys. Rev. D* 83.8, 083507, p. 083507. DOI: [10.1103/PhysRevD.83.083507](https://doi.org/10.1103/PhysRevD.83.083507). arXiv: [1009.4936 \[hep-ph\]](https://arxiv.org/abs/1009.4936).
- Cesarsky, C. J. (Jan. 1980). “Cosmic-ray confinement in the galaxy”. In: *ARA&A* 18, pp. 289–319. DOI: [10.1146/annurev.aa.18.090180.001445](https://doi.org/10.1146/annurev.aa.18.090180.001445).
- Chang, Laura J and Lina Necib (Aug. 2021). “Dark matter density profiles in dwarf galaxies: linking Jeans modelling systematics and observation”. In: *Monthly Notices of the Royal Astronomical Society* 507.4, pp. 4715–4733. ISSN: 1365-2966. DOI: [10.1093/mnras/stab2440](https://doi.org/10.1093/mnras/stab2440). URL: <http://dx.doi.org/10.1093/mnras/stab2440>.
- Chiappo, A et al. (July 2019). “Dwarf spheroidal J-factor likelihoods for generalized NFW profiles”. In: *Monthly Notices of the Royal Astronomical Society* 488.2, pp. 2616–2628. ISSN: 1365-2966. DOI: [10.1093/mnras/stz1871](https://doi.org/10.1093/mnras/stz1871). URL: <http://dx.doi.org/10.1093/mnras/stz1871>.
- Chyży, K. T. et al. (Apr. 2011). “Magnetic fields in Local Group dwarf irregulars”. In: *A&A* 529, A94. ISSN: 1432-0746. DOI: [10.1051/0004-6361/201015393](https://doi.org/10.1051/0004-6361/201015393). URL: <http://dx.doi.org/10.1051/0004-6361/201015393>.
- Clark, B. G. (Sept. 1980). “An efficient implementation of the algorithm ‘CLEAN’”. In: *A&A* 89.3, p. 377.
- Colafrancesco, S., S. Profumo, and P. Ullio (July 2006). “Multi-frequency analysis of neutralino dark matter annihilations in the Coma cluster”. In: *A&A* 455.1, pp. 21–43. ISSN: 1432-0746. DOI: [10.1051/0004-6361:20053887](https://doi.org/10.1051/0004-6361:20053887). URL: <http://dx.doi.org/10.1051/0004-6361:20053887>.
- Colafrancesco, Sergio, Stefano Profumo, and Piero Ullio (Jan. 2007). “Detecting dark matter WIMPs in the Draco dwarf: A multiwavelength perspective”. In: *Physical Review D* 75.2. ISSN: 1550-2368. DOI: [10.1103/physrevd.75.023513](https://doi.org/10.1103/physrevd.75.023513). URL: <http://dx.doi.org/10.1103/PhysRevD.75.023513>.
- Coles, Peter and Bernard Jones (Jan. 1991). “A lognormal model for the cosmological mass distribution.” In: *MNRAS* 248, pp. 1–13. DOI: [10.1093/mnras/248.1.1](https://doi.org/10.1093/mnras/248.1.1).
- Coles, Peter and Francesco Lucchin (Jan. 1995). “Cosmology, The Origin and Evolution of Cosmic Structure”. In: *Chichester: Wiley, |c1995 -1*.
- Condon, J. J. (Mar. 1974). “Confusion and Flux-Density Error Distributions”. In: *ApJ* 188, pp. 279–286. DOI: [10.1086/152714](https://doi.org/10.1086/152714).
- Condon, James J. and Scott M. Ransom (2016). *Essential Radio Astronomy*.
- Cook, R H W et al. (Mar. 2020). “Searching for dark matter signals from local dwarf spheroidal galaxies at low radio frequencies in the GLEAM survey”. In: *Monthly Notices of the Royal Astronomical Society* 494.1, pp. 135–145. ISSN: 1365-2966. DOI: [10.1093/mnras/staa726](https://doi.org/10.1093/mnras/staa726). URL: <http://dx.doi.org/10.1093/mnras/staa726>.
- Diemand, Jürg and Michael Kuhlen (May 2008). “Infall Caustics in Dark Matter Halos?” In: *The Astrophysical Journal* 680.1, pp. L25–L28. ISSN: 1538-4357. DOI: [10.1086/589688](https://doi.org/10.1086/589688). URL: <http://dx.doi.org/10.1086/589688>.
- Dolphin, Andrew E. et al. (2005). *Star Formation Histories of Local Group Dwarf Galaxies*. arXiv: [astro-ph/0506430 \[astro-ph\]](https://arxiv.org/abs/astro-ph/0506430).
- Douglas, James N. et al. (May 1996). “The Texas Survey of Radio Sources Covering -35.5 degrees < declination < 71.5 degrees at 365 MHz”. In: *AJ* 111, p. 1945. DOI: [10.1086/117932](https://doi.org/10.1086/117932).
- Drlica-Wagner, A. et al. (Aug. 2015). “SEARCH FOR GAMMA-RAY EMISSION FROM DES DWARF SPHEROIDAL GALAXY CANDIDATES WITH FERMI -LAT DATA”. In: *The Astrophysical Journal* 809.1, p. L4. ISSN: 2041-8213. DOI: [10.1088/2041-8205/809/1/L4](https://doi.org/10.1088/2041-8205/809/1/L4). URL: <http://dx.doi.org/10.1088/2041-8205/809/1/L4>.
- Drlica-Wagner, A. et al. (Apr. 2020). “Milky Way Satellite Census. I. The Observational Selection Function for Milky Way Satellites in DES Y3 and Pan-STARRS DR1”. In:

- 893.1, p. 47. DOI: [10.3847/1538-4357/ab7eb9](https://doi.org/10.3847/1538-4357/ab7eb9). URL: <https://doi.org/10.3847/1538-4357/ab7eb9>.
- Drukier, Andrzej K., Katherine Freese, and David N. Spergel (June 1986). “Detecting cold dark-matter candidates”. In: *Phys. Rev. D* 33 (12), pp. 3495–3508. DOI: [10.1103/PhysRevD.33.3495](https://link.aps.org/doi/10.1103/PhysRevD.33.3495). URL: <https://link.aps.org/doi/10.1103/PhysRevD.33.3495>.
- Einasto, J. (Jan. 1968). “On constructing models of stellar systems. V. The binomial model.” In: *Publications of the Tartu Astrofizica Observatory* 36, pp. 414–441.
- Evans, N. W., J. L. Sanders, and Alex Geringer-Sameth (May 2016). “Simple J-factors and D-factors for indirect dark matter detection”. In: *Physical Review D* 93.10. ISSN: 2470-0029. DOI: [10.1103/physrevd.93.103512](https://doi.org/10.1103/physrevd.93.103512). URL: <http://dx.doi.org/10.1103/PhysRevD.93.103512>.
- Faria, D. et al. (Oct. 2006). “The usage of Strömgren photometry in studies of local group dwarf spheroidal galaxies”. In: *A&A* 465.2, pp. 357–373. ISSN: 1432-0746. DOI: [10.1051/0004-6361:20065244](https://doi.org/10.1051/0004-6361:20065244). URL: <http://dx.doi.org/10.1051/0004-6361:20065244>.
- Geringer-Sameth, Alex, Savvas M. Koushiappas, and Matthew G. Walker (Apr. 2015a). “Comprehensive search for dark matter annihilation in dwarf galaxies”. In: *Phys. Rev. D* 91.8, 083535, p. 083535. DOI: [10.1103/PhysRevD.91.083535](https://doi.org/10.1103/PhysRevD.91.083535). arXiv: [1410.2242 \[astro-ph.CO\]](https://arxiv.org/abs/1410.2242).
- Geringer-Sameth, Alex et al. (Aug. 2015b). “Indication of Gamma-Ray Emission from the Newly Discovered Dwarf Galaxy Reticulum II”. In: *Physical Review Letters* 115.8. ISSN: 1079-7114. DOI: [10.1103/physrevlett.115.081101](https://doi.org/10.1103/PhysRevLett.115.081101). URL: <http://dx.doi.org/10.1103/PhysRevLett.115.081101>.
- (Aug. 2015c). “Indication of Gamma-Ray Emission from the Newly Discovered Dwarf Galaxy Reticulum II”. In: *Physical Review Letters* 115.8. ISSN: 1079-7114. DOI: [10.1103/physrevlett.115.081101](https://doi.org/10.1103/physrevlett.115.081101). URL: <http://dx.doi.org/10.1103/PhysRevLett.115.081101>.
- Goodman, Mark W. and Edward Witten (June 1985). “Detectability of certain dark-matter candidates”. In: *Phys. Rev. D* 31 (12), pp. 3059–3063. DOI: [10.1103/PhysRevD.31.3059](https://doi.org/10.1103/PhysRevD.31.3059). URL: <https://link.aps.org/doi/10.1103/PhysRevD.31.3059>.
- Gunn, J. E. et al. (Aug. 1978). “Some astrophysical consequences of the existence of a heavy stable neutral lepton.” In: *ApJ* 223, pp. 1015–1031. DOI: [10.1086/156335](https://doi.org/10.1086/156335).
- Gupta, Y. et al. (Aug. 2017). “The upgraded GMRT: opening new windows on the radio Universe”. In: *Current Science* 113.4, pp. 707–714. DOI: [10.18520/cs/v113/i04/707-714](https://doi.org/10.18520/cs/v113/i04/707-714).
- Högbom, J. A. (June 1974). “Aperture Synthesis with a Non-Regular Distribution of Interferometer Baselines”. In: *A&AS* 15, p. 417.
- Hooper, Dan and Tim Linden (Sept. 2015). “On The gamma-ray emission from Reticulum II and other dwarf galaxies”. In: *Journal of Cosmology and Astroparticle Physics* 2015.09, pp. 016–016. ISSN: 1475-7516. DOI: [10.1088/1475-7516/2015/09/016](https://doi.org/10.1088/1475-7516/2015/09/016). URL: <http://dx.doi.org/10.1088/1475-7516/2015/09/016>.
- Horigome, Shun-ichi et al. (Sept. 2020). “J-factor estimation of Draco, Sculptor, and Ursa Minor dwarf spheroidal galaxies with the member/foreground mixture model”. In: *Monthly Notices of the Royal Astronomical Society* 499.3, pp. 3320–3337. ISSN: 1365-2966. DOI: [10.1093/mnras/staa2909](https://doi.org/10.1093/mnras/staa2909). URL: <http://dx.doi.org/10.1093/mnras/staa2909>.
- Hurley-Walker, N. et al. (Sept. 2016). “GaLactic and Extragalactic All-sky Murchison Widefield Array (GLEAM) survey – I. A low-frequency extragalactic catalogue”. In: *Monthly Notices of the Royal Astronomical Society* 464.1, pp. 1146–1167. ISSN: 1365-2966. DOI: [10.1093/mnras/stw2337](https://doi.org/10.1093/mnras/stw2337). URL: <http://dx.doi.org/10.1093/mnras/stw2337>.
- Intema, H. T. et al. (Feb. 2017). “The GMRT 150 MHz all-sky radio survey”. In: *A&A* 598, A78. ISSN: 1432-0746. DOI: [10.1051/0004-6361/201628536](https://doi.org/10.1051/0004-6361/201628536). URL: <http://dx.doi.org/10.1051/0004-6361/201628536>.
- Kapteyn, J. C. (May 1922). “First Attempt at a Theory of the Arrangement and Motion of the Sidereal System”. In: *ApJ* 55, p. 302. DOI: [10.1086/142670](https://doi.org/10.1086/142670).

- Kar, Arpan et al. (Aug. 2019). “Constraints on dark matter annihilation in dwarf spheroidal galaxies from low frequency radio observations”. In: *Physical Review D* 100.4. ISSN: 2470-0029. DOI: [10.1103/physrevd.100.043002](https://doi.org/10.1103/PhysRevD.100.043002). URL: <http://dx.doi.org/10.1103/PhysRevD.100.043002>.
- Klop, Niki et al. (June 2017). “Impact of axisymmetric mass models for dwarf spheroidal galaxies on indirect dark matter searches”. In: *Physical Review D* 95.12. ISSN: 2470-0029. DOI: [10.1103/physrevd.95.123012](https://doi.org/10.1103/PhysRevD.95.123012). URL: <http://dx.doi.org/10.1103/PhysRevD.95.123012>.
- Lake, George (July 1990). “Detectability of γ -rays from clumps of dark matter”. In: *Nature* 346.6279, pp. 39–40. ISSN: 1476-4687. DOI: [10.1038/346039a0](https://doi.org/10.1038/346039a0). URL: <https://doi.org/10.1038/346039a0>.
- Leane, Rebecca K. et al. (July 2018). “GeV-scale thermal WIMPs: Not even slightly ruled out”. In: *Phys. Rev. D* 98 (2), p. 023016. DOI: [10.1103/PhysRevD.98.023016](https://link.aps.org/doi/10.1103/PhysRevD.98.023016). URL: <https://link.aps.org/doi/10.1103/PhysRevD.98.023016>.
- Lee, Benjamin W. and Steven Weinberg (1977). “Cosmological lower bound on heavy-neutrino masses”. In: *Physical Review Letters* 39, pp. 165–168.
- Martinez, G. D. (June 2015). “A robust determination of Milky Way satellite properties using hierarchical mass modelling”. In: *Monthly Notices of the Royal Astronomical Society* 451.3, pp. 2524–2535. ISSN: 1365-2966. DOI: [10.1093/mnras/stv942](http://dx.doi.org/10.1093/mnras/stv942). URL: <http://dx.doi.org/10.1093/mnras/stv942>.
- Mashchenko, Sergey, Alison Sills, and H. M. Couchman (Mar. 2006). “Constraining Global Properties of the Draco Dwarf Spheroidal Galaxy”. In: *The Astrophysical Journal* 640.1, pp. 252–269. ISSN: 1538-4357. DOI: [10.1086/499940](http://dx.doi.org/10.1086/499940). URL: <http://dx.doi.org/10.1086/499940>.
- Masiero, A., S. Profumo, and P. Ullio (Apr. 2005). “Neutralino dark matter detection in split supersymmetry scenarios”. In: *Nuclear Physics B* 712.1-2, pp. 86–114. ISSN: 0550-3213. DOI: [10.1016/j.nuclphysb.2005.01.028](http://dx.doi.org/10.1016/j.nuclphysb.2005.01.028). URL: <http://dx.doi.org/10.1016/j.nuclphysb.2005.01.028>.
- Mayer, Lucio et al. (Oct. 2001). “The Metamorphosis of Tidally Stirred Dwarf Galaxies”. In: *The Astrophysical Journal* 559.2, pp. 754–784. ISSN: 1538-4357. DOI: [10.1086/322356](http://dx.doi.org/10.1086/322356). URL: <http://dx.doi.org/10.1086/322356>.
- McConnachie, Alan W. (June 2012). “THE OBSERVED PROPERTIES OF DWARF GALAXIES IN AND AROUND THE LOCAL GROUP”. In: *The Astronomical Journal* 144.1, p. 4. ISSN: 1538-3881. DOI: [10.1088/0004-6256/144/1/4](http://dx.doi.org/10.1088/0004-6256/144/1/4). URL: <http://dx.doi.org/10.1088/0004-6256/144/1/4>.
- McGaugh, Stacy S. and W. J. G. de Blok (May 1998). “Testing the Dark Matter Hypothesis with Low Surface Brightness Galaxies and Other Evidence”. In: *ApJ* 499.1, pp. 41–65. DOI: [10.1086/305612](https://arxiv.org/abs/astro-ph/9801123). arXiv: [astro-ph/9801123](https://arxiv.org/abs/astro-ph/9801123) [astro-ph].
- Montanari, A., E. Moulin, and D. Malyshev (2021). *Search for dark matter annihilation signals from the Galactic Center with the H.E.S.S. Inner Galaxy Survey*. arXiv: [2108.10302](https://arxiv.org/abs/2108.10302) [astro-ph.HE].
- Moore, B. et al. (May 1998). “Resolving the Structure of Cold Dark Matter Halos”. In: *ApJ* 499.1, pp. L5–L8. DOI: [10.1086/311333](https://arxiv.org/abs/astro-ph/9709051). arXiv: [astro-ph/9709051](https://arxiv.org/abs/astro-ph/9709051) [astro-ph].
- Moore, Ben (Aug. 1994). “Evidence against dissipation-less dark matter from observations of galaxy haloes”. In: *Nature* 370.6491, pp. 629–631. DOI: [10.1038/370629a0](https://doi.org/10.1038/370629a0).
- Natarajan, Aravind et al. (Oct. 2013). “Bounds on dark matter properties from radio observations of Ursa Major II using the Green Bank Telescope”. In: *Physical Review D* 88.8. ISSN: 1550-2368. DOI: [10.1103/physrevd.88.083535](http://dx.doi.org/10.1103/PhysRevD.88.083535). URL: <http://dx.doi.org/10.1103/PhysRevD.88.083535>.
- Natarajan, Aravind et al. (2015). *Green Bank Telescope Constraints on Dark Matter Annihilation in Segue I*. arXiv: [1507.03589](https://arxiv.org/abs/1507.03589) [astro-ph.CO].

- Navarro, Julio F., Carlos S. Frenk, and Simon D. M. White (May 1996). “The Structure of Cold Dark Matter Halos”. In: *The Astrophysical Journal* 462, p. 563. ISSN: 1538-4357. DOI: [10.1086/177173](https://doi.org/10.1086/177173). URL: <http://dx.doi.org/10.1086/177173>.
- Norris, Ray P. et al. (2011). “EMU: Evolutionary Map of the Universe”. In: *Publications of the Astronomical Society of Australia* 28.3, pp. 215–248. ISSN: 1448-6083. DOI: [10.1071/as11021](https://doi.org/10.1071/as11021). URL: <http://dx.doi.org/10.1071/AS11021>.
- Perley, R. A. and B. J. Butler (May 2017). “An Accurate Flux Density Scale from 50 MHz to 50 GHz”. In: *ApJS* 230.1, 7, p. 7. DOI: [10.3847/1538-4365/aa6df9](https://doi.org/10.3847/1538-4365/aa6df9). arXiv: [1609.05940](https://arxiv.org/abs/1609.05940) [astro-ph.IM].
- Petač, Mihael, Piero Ullio, and Mauro Valli (Dec. 2018). “On velocity-dependent dark matter annihilations in dwarf satellites”. In: *Journal of Cosmology and Astroparticle Physics* 2018.12, pp. 039–039. ISSN: 1475-7516. DOI: [10.1088/1475-7516/2018/12/039](https://doi.org/10.1088/1475-7516/2018/12/039). URL: <http://dx.doi.org/10.1088/1475-7516/2018/12/039>.
- Poincarè, H. (Oct. 1906). “The Milky Way and the Theory of Gases”. In: *Popular Astronomy* 14, pp. 475–488.
- Pontzen, Andrew and Fabio Governato (Apr. 2012). “How supernova feedback turns dark matter cusps into cores”. In: *MNRAS* 421.4, pp. 3464–3471. DOI: [10.1111/j.1365-2966.2012.20571.x](https://doi.org/10.1111/j.1365-2966.2012.20571.x). arXiv: [1106.0499](https://arxiv.org/abs/1106.0499) [astro-ph.CO].
- Pospelov, Maxim, Adam Ritz, and Mikhail Voloshin (Apr. 2008). “Secluded WIMP dark matter”. In: *Physics Letters B* 662.1, pp. 53–61. DOI: [10.1016/j.physletb.2008.02.052](https://doi.org/10.1016/j.physletb.2008.02.052). arXiv: [0711.4866](https://arxiv.org/abs/0711.4866) [hep-ph].
- Press, William H. and Paul Schechter (Feb. 1974). “Formation of Galaxies and Clusters of Galaxies by Self-Similar Gravitational Condensation”. In: *ApJ* 187, pp. 425–438. DOI: [10.1086/152650](https://doi.org/10.1086/152650).
- Profumo, Stefano (Nov. 2005). “TeV γ -rays and the largest masses and annihilation cross sections of neutralino dark matter”. In: *Phys. Rev. D* 72 (10), p. 103521. DOI: [10.1103/PhysRevD.72.103521](https://doi.org/10.1103/PhysRevD.72.103521). URL: <https://link.aps.org/doi/10.1103/PhysRevD.72.103521>.
- Putman, Mary E. et al. (May 2021). “The Gas Content and Stripping of Local Group Dwarf Galaxies”. In: *The Astrophysical Journal* 913.1, p. 53. ISSN: 1538-4357. DOI: [10.3847/1538-4357/abe391](https://doi.org/10.3847/1538-4357/abe391). URL: <http://dx.doi.org/10.3847/1538-4357/abe391>.
- Read, J I (May 2014). “The local dark matter density”. In: *Journal of Physics G: Nuclear and Particle Physics* 41.6, p. 063101. ISSN: 1361-6471. DOI: [10.1088/0954-3899/41/6/063101](https://doi.org/10.1088/0954-3899/41/6/063101). URL: <http://dx.doi.org/10.1088/0954-3899/41/6/063101>.
- Regis, Marco, Laura Richter, and Sergio Colafrancesco (July 2017). “Dark matter in the Reticulum II dSph: a radio search”. In: *Journal of Cosmology and Astroparticle Physics* 2017.07, pp. 025–025. ISSN: 1475-7516. DOI: [10.1088/1475-7516/2017/07/025](https://doi.org/10.1088/1475-7516/2017/07/025). URL: <http://dx.doi.org/10.1088/1475-7516/2017/07/025>.
- Regis, Marco and Piero Ullio (Aug. 2008). “Multiwavelength signals of dark matter annihilations at the Galactic center”. In: *Physical Review D* 78.4. ISSN: 1550-2368. DOI: [10.1103/physrevd.78.043505](https://doi.org/10.1103/physrevd.78.043505). URL: <http://dx.doi.org/10.1103/PhysRevD.78.043505>.
- Regis, Marco et al. (Oct. 2014). “Local Group dSph radio survey with ATCA (III): constraints on particle dark matter”. In: *Journal of Cosmology and Astroparticle Physics* 2014.10, pp. 016–016. ISSN: 1475-7516. DOI: [10.1088/1475-7516/2014/10/016](https://doi.org/10.1088/1475-7516/2014/10/016). URL: <http://dx.doi.org/10.1088/1475-7516/2014/10/016>.
- Regis, Marco et al. (Mar. 2015a). “Local Group dSph radio survey with ATCA – I: observations and background sources”. In: *Monthly Notices of the Royal Astronomical Society* 448.4, pp. 3731–3746. ISSN: 0035-8711. DOI: [10.1093/mnras/stu2747](https://doi.org/10.1093/mnras/stu2747). URL: <http://dx.doi.org/10.1093/mnras/stu2747>.
- Regis, Marco et al. (Mar. 2015b). “Local Group dSph radio survey with ATCA – II. Non-thermal diffuse emission”. In: *Monthly Notices of the Royal Astronomical Society* 448.4,

- pp. 3747–3765. ISSN: 0035-8711. DOI: [10.1093/mnras/stv127](https://doi.org/10.1093/mnras/stv127). URL: <http://dx.doi.org/10.1093/mnras/stv127>.
- Regis, Marco et al. (Nov. 2021). “The EMU view of the Large Magellanic Cloud: troubles for sub-TeV WIMPs”. In: *Journal of Cosmology and Astroparticle Physics* 2021.11, p. 046. ISSN: 1475-7516. DOI: [10.1088/1475-7516/2021/11/046](https://doi.org/10.1088/1475-7516/2021/11/046). URL: <http://dx.doi.org/10.1088/1475-7516/2021/11/046>.
- Roberts, M. S. and R. N. Whitehurst (Oct. 1975). “The rotation curve and geometry of M31 at large galactocentric distances.” In: *ApJ* 201, pp. 327–346. DOI: [10.1086/153889](https://doi.org/10.1086/153889).
- Rubin, Vera C. and Jr. Ford W. Kent (Feb. 1970). “Rotation of the Andromeda Nebula from a Spectroscopic Survey of Emission Regions”. In: *ApJ* 159, p. 379. DOI: [10.1086/150317](https://doi.org/10.1086/150317).
- Ruchayskiy, Oleg et al. (May 2016). “Searching for decaying dark matter in deep XMM–Newton observation of the Draco dwarf spheroidal”. In: *Monthly Notices of the Royal Astronomical Society* 460.2, pp. 1390–1398. ISSN: 0035-8711. DOI: [10.1093/mnras/stw1026](https://doi.org/10.1093/mnras/stw1026). eprint: <https://academic.oup.com/mnras/article-pdf/460/2/1390/8115197/stw1026.pdf>. URL: <https://doi.org/10.1093/mnras/stw1026>.
- Rybicki, George B. and Alan P. Lightman (1986). *Radiative Processes in Astrophysics*.
- Schechter, P. (Jan. 1976). “An analytic expression for the luminosity function for galaxies.” In: *ApJ* 203, pp. 297–306. DOI: [10.1086/154079](https://doi.org/10.1086/154079).
- Schramm, David N. and Michael S. Turner (May 1996). “Deuteronomy and numbers”. In: *Nature* 381.6579, pp. 193–194. ISSN: 1476-4687. DOI: [10.1038/381193a0](https://doi.org/10.1038/381193a0). URL: <https://doi.org/10.1038/381193a0>.
- Shapley, Harlow (Mar. 1938). “A Stellar System of a New Type”. In: *Harvard College Observatory Bulletin* 908, pp. 1–11.
- Sheth, Ravi K. and Giuseppe Tormen (Jan. 2002). “An excursion set model of hierarchical clustering: ellipsoidal collapse and the moving barrier”. In: *Monthly Notices of the Royal Astronomical Society* 329.1, pp. 61–75. ISSN: 1365-2966. DOI: [10.1046/j.1365-8711.2002.04950.x](https://doi.org/10.1046/j.1365-8711.2002.04950.x). URL: <http://dx.doi.org/10.1046/j.1365-8711.2002.04950.x>.
- Siffert, Beatriz B. et al. (Oct. 2010). “Radio emission from dark matter annihilation in the Large Magellanic Cloud”. In: *Monthly Notices of the Royal Astronomical Society* 410.4, pp. 2463–2471. ISSN: 0035-8711. DOI: [10.1111/j.1365-2966.2010.17613.x](https://doi.org/10.1111/j.1365-2966.2010.17613.x). URL: <http://dx.doi.org/10.1111/j.1365-2966.2010.17613.x>.
- Simon, Joshua D. (Aug. 2019). “The Faintest Dwarf Galaxies”. In: *Annual Review of Astronomy and Astrophysics* 57.1, pp. 375–415. ISSN: 1545-4282. DOI: [10.1146/annurev-astro-091918-104453](https://doi.org/10.1146/annurev-astro-091918-104453). URL: <http://dx.doi.org/10.1146/annurev-astro-091918-104453>.
- Spekkens, Kristine et al. (July 2013). “A DEEP SEARCH FOR EXTENDED RADIO CONTINUUM EMISSION FROM DWARF SPHEROIDAL GALAXIES: IMPLICATIONS FOR PARTICLE DARK MATTER”. In: *The Astrophysical Journal* 773.1, p. 61. ISSN: 1538-4357. DOI: [10.1088/0004-637x/773/1/61](https://doi.org/10.1088/0004-637x/773/1/61). URL: <http://dx.doi.org/10.1088/0004-637x/773/1/61>.
- Stasyszyn, F. et al. (Sept. 2010). “Measuring cosmic magnetic fields by rotation measure–galaxy cross-correlations in cosmological simulations”. In: *Monthly Notices of the Royal Astronomical Society* 408.2, pp. 684–694. ISSN: 0035-8711. DOI: [10.1111/j.1365-2966.2010.17166.x](https://doi.org/10.1111/j.1365-2966.2010.17166.x). URL: <http://dx.doi.org/10.1111/j.1365-2966.2010.17166.x>.
- Steigman, Gary, Basudeb Dasgupta, and John F. Beacom (July 2012). “Precise relic WIMP abundance and its impact on searches for dark matter annihilation”. In: *Physical Review D* 86.2. ISSN: 1550-2368. DOI: [10.1103/physrevd.86.023506](https://doi.org/10.1103/physrevd.86.023506). URL: <http://dx.doi.org/10.1103/PhysRevD.86.023506>.
- Strigari, Louis E (Mar. 2018). “Dark matter in dwarf spheroidal galaxies and indirect detection: a review”. In: *Reports on Progress in Physics* 81.5, p. 056901. ISSN: 1361-6633. DOI: [10.1088/1361-6633/aaae16](https://doi.org/10.1088/1361-6633/aaae16). URL: <http://dx.doi.org/10.1088/1361-6633/aaae16>.

- Tasitsiomi, Argyro, Jennifer Gaskins, and Angela V. Olinto (Sept. 2004). “Gamma-ray and synchrotron emission from neutralino annihilation in the Large Magellanic Cloud”. In: *Astroparticle Physics* 21.6, pp. 637–650. ISSN: 0927-6505. DOI: [10.1016/j.astropartphys.2004.04.004](https://doi.org/10.1016/j.astropartphys.2004.04.004). URL: <http://dx.doi.org/10.1016/j.astropartphys.2004.04.004>.
- Thompson, Anthony, James Moran, and George Swenson Jr (Jan. 1991). *Interferometry and Synthesis in Radio Astronomy*. Vol. -1. ISBN: 978-3-319-44429-1. DOI: [10.1007/978-3-319-44431-4](https://doi.org/10.1007/978-3-319-44431-4).
- Véron-Cetty, M. -P. and P. Véron (Aug. 2006). “A catalogue of quasars and active nuclei: 12th edition”. In: *A&A* 455.2, pp. 773–777. DOI: [10.1051/0004-6361:20065177](https://doi.org/10.1051/0004-6361:20065177).
- Vollmann, Martin et al. (June 2020). “Radio constraints on dark matter annihilation in Canes Venatici I with LOFAR†”. In: *Monthly Notices of the Royal Astronomical Society* 496.3, pp. 2663–2672. ISSN: 1365-2966. DOI: [10.1093/mnras/staa1657](https://doi.org/10.1093/mnras/staa1657). URL: <http://dx.doi.org/10.1093/mnras/staa1657>.
- Widrow, Lawrence M., Brent Pym, and John Dubinski (June 2008). “Dynamical Blueprints for Galaxies”. In: *The Astrophysical Journal* 679.2, pp. 1239–1259. ISSN: 1538-4357. DOI: [10.1086/587636](https://doi.org/10.1086/587636). URL: <http://dx.doi.org/10.1086/587636>.
- Wilson, A. G. (Feb. 1955). “Sculptor-Type Systems in the Local Group of Galaxies”. In: *PASP* 67.394, pp. 27–29. DOI: [10.1086/126754](https://doi.org/10.1086/126754).
- Zang, Z. and E. J. A. Meurs (July 2001). “The Cores of Local Group Galaxies at X-Rays”. In: *The Astrophysical Journal* 556.1, pp. 24–34. DOI: [10.1086/321582](https://doi.org/10.1086/321582). URL: <https://doi.org/10.1086/321582>.
- Zwicky, F. (Jan. 1933). “Die Rotverschiebung von extragalaktischen Nebeln”. In: *Helvetica Physica Acta* 6, pp. 110–127.